Laser Manipulation of Indium Atoms

Dissertation
zur Erlangung des Doktorgrades (Dr. rer. nat.)
der Mathematisch-Naturwissenschaftlichen Fakultät
der Rheinischen Friedrich-Wilhelms-Universität Bonn

vorgelegt von
Ruby dela Torre
aus
Philippines

Bonn 2005

Angefertigt mit Genehmigung
der Mathematisch-Naturwissenschaftlichen Fakultät
der Rheinischen Friedrich-Wilhelms-Universität Bonn

1. Gutachter: Prof. Dr. Dieter Meschede
2. Gutachter: Prof. Dr. Karsten Buse

Tag der Promotion: 12.Juli.2005

Contents

Introduction

"There is nothing that I can see in the physical laws that says the computer elements can not be made enormously smaller than they are now", predicted Richard Feynman on the evolution of microprocessor devices in 1959 [1]. At around the same time, Intel co-founder Gordon Moore forecasted the rapid pace of technological innovation with his popular prediction known as "Moore's Law", which states that the transistor density on integrated circuits doubles about every two years. As an example, at year 2000, Intel's Pentium 4 processor had 42,000,000 transistors and at year 2003, Intel's Itanium 2 processor had 410,000,000 transistors [2]. To scale down microprocessor chips, several lithography processes are being explored to achieve feature sizes between hundreds to tens of nanometers.

Conventional optical lithography can create feature sizes of 200 nm, but this feature size is diffraction-limited. One way of raising the bar in this field is by using extreme ultra-violet (EUV) light sources, with wavelengths of 13 nm. The feature size that was achieved so far is around 80 nm. With EUV lithography, a new set of optical coatings in this regime has to be custom-built and surface roughness becomes critical. Another lithography method which can produce even smaller structures, at tens of nanometer range, is electron beam or ion beam lithography. One drawback for this type of lithography is that it is a serial writing process and is, therefore, slow. Another disadvantage is that it can be destructive to the masks and the substrates due to the high-energy of the electron or ion beam. Scanning probe patterning can make structures of single atom dimension, but the process is extremely slow as the atoms have to be deposited one at a time. Another lithography process which is our interest in this research endeavor is atom lithography. In atom lithography, an atomic beam is manipulated to create the desired structure as it interacts with the substrate. Contrary to optical lithography, atom lithography is not diffraction-limited. Thus, smaller structures can be produced because the de-Broglie wavelength is in the nanometer range and below. Unlike e-beam or ion beam lithography, there is no restriction due to Coulomb repulsion because neutral atoms are used, and the low energy of an atomic beam does not damage the substrate. Light masks can be used to create atomic patterns onto a substrate, which allows parallel writing to be achieved. In atom lithography, a laser standing wave focuses the atoms in its nodes during deposition onto a substrate [3]. If only a single standing wave is used as a light mask, the smallest structure that can be attained is half the wavelength of the standing wave, which is on the order of hundred nanometers, but a combination of standing wave light masks can be used to create smaller and more complex structures [4]. Atom lithography has been demonstrated in sodium [5], cesium [6], chromium [7, 8], aluminum [9], and recently, ytterbium [10].

There are two stages in atom lithography. The first stage is the atomic beam collimation in order to have a significant level of atomic flux for deposition. The second stage is the deposition, wherein the atomic beam interacts with a standing wave light mask to create the desired pattern onto the substrate. In this thesis, we are concerned only with the first stage, that is, atomic beam collimation via laser cooling. Laser cooling of an atomic beam allows one to control the atomic velocity distribution using lasers, whose frequencies are nearly in resonance with the atomic transitions. By controlling the atomic velocity, the overall flux of atoms at the deposition region can be increased. One-dimensional transverse laser cooling of an indium atomic beam has been experimentally realized in this work. Indium is a technologically significant element as it is used in electronic and opto-electronic devices, when combined with other elements, for instance, Phosphorus to form InP, or combined with Gallium and Arsenic to form InGaAs. Thus, the ability to manipulate indium with optical fields and, eventually, deposit it on a substrate with minimum feature size has great engineering implications.

One challenge in laser cooling of indium is that there is no closed atomic transition with a reasonably populated initial state. Thus, a five-frequency Lambda-scheme was employed to achieve transverse laser cooling of an atomic beam. In the first chapter of this thesis, the indium atom with its multilevel atomic structure is discussed and its interaction with the light field is treated in a semiclassical approach. The light sources used in the laser cooling experiment will be presented in chapter 2. The method of frequency stabilization of the light sources and atomic spectroscopy of indium will be discussed in chapter 3. The laser cooling schemes and experimental results will be discussed in the last chapter. The cooling effect for different detuning, intensity and polarization of the light fields at the cooling region will be presented.

Chapter 1

Theory

1.1 Light field Interaction with an Indium Atom

In this chapter, the interaction between an indium atom and the optical fields used in laser cooling is elaborated. The motion of an atom traversing a light field can be described mathematically by defining the Hamiltonian of the system and the atomic wavefunction. At this point, we limit our discussion to an atom, with no collisions to other atoms and its internal and external states are influenced by one or more monochromatic light fields. The total Hamiltonian can be written as:

$$\hat{H} = \hat{H}_A - \hat{\mathbf{d}} \cdot \vec{\mathbf{E}} \tag{1.1}$$

where the first term, $\hat{H}_A$, is the Hamiltonian operator describing the complex internal atomic structure in terms of the energy levels and the relaxation rates and the second term describes the interaction of the atom with the light field. The dipole moment operator of an atom is denoted by $\hat{\mathbf{d}}$ and the electric field by $\vec{\mathbf{E}}$. The field $\vec{\mathbf{E}}$ can be written as

$$\vec{\mathbf{E}}(\vec{r}, t) = \frac{1}{2} \sum_{\lambda} \hat{\varepsilon} E_{\lambda}(\vec{r}, t) \mathrm{e}^{-i\omega_{\lambda} t - i\phi_{\lambda}} + \hat{\varepsilon} E^{*}_{\lambda}(\vec{r}, t) \mathrm{e}^{i\omega_{\lambda} t + i\phi_{\lambda}} \tag{1.2}$$

where the summation is taken over the different radiation modes of a laser, labelled by λ to specify the wavelength and $\hat{\varepsilon}$ is the unit polarization vector. The electric field is a time-dependent vector field in the semiclassical approach, while in the full quantum-mechanical approach, the electric field is treated as an operator. The interaction of the atom with the light field is incorporated in the $\hat{\mathbf{d}} \cdot \vec{\mathbf{E}}$ term, which is related to a ubiquitous quantity in atomic physics, the Rabi frequency Ω. The relation between the dipole matrix element of the atomic transition and the Rabi frequency is given by:

$$\hbar\Omega_{nm} = -\vec{\mathbf{d}}_{nm} \cdot \vec{\mathbf{E}} = -\frac{1}{2}\langle\psi_n|\vec{\mathbf{d}} \cdot \hat{\varepsilon}|\psi_m\rangle \sum_{\lambda}(E_{\lambda}^{*}e^{i\omega t+i\phi} + E_{\lambda}e^{-i\omega t-i\phi}) \tag{1.3}$$

The wavefunction of the atom can be constructed as a superposition of the available atomic states,

$$\Psi(x,t) = \sum_{n} C_n(t)\psi_n(x)e^{-i\zeta_n} \tag{1.4}$$

where ψ_n is an eigenstate of the free atom Hamiltonian, C_n is the probability amplitude, and ζ_n is the phase, which is a function of time, t, and this will be determined when the rotating wave approximation is used.

If relaxation mechanisms are considered, it is more appropriate to employ a density-matrix approach, with its evolution being governed by the Liouville equation. The density-matrix approach is related to the wavefunction description. The probability amplitude $C_i(t)$ is related to the density matrix elements $\rho_{mn}^{(i)}(t)$ by the following equation:

$$\rho_{mn}^{(i)}(t) = C_m^{(i)}(t)C_n^{(i)}(t)^{*} \tag{1.5}$$

The population is represented by $\rho_{mm}(t)$ and the degree of coherence by $\rho_{mn}(t)$. Instead of the Schrödinger equation describing the evolution of the wavefunction, the evolution of the atomic density matrix $\rho(t)$ is governed by the Liouville equation, given by

$$\frac{d\rho(t)}{dt} = \frac{1}{i\hbar}[\hat{H}, \rho(t)] + \hat{L}_{loss}\rho \tag{1.6}$$

where $\hat{L}_{loss}$ is the relaxation operator. If the only relaxation mechanism is spontaneous emission, $\hat{L}_{loss}$ can be written in Lindblad form as [14]:

$$\hat{L}_{loss}\rho = \sum_{ij}\Gamma_{ij}(S_{ij}\ \rho\ S_{ij}^{\dagger}) - \frac{1}{2}\ \Gamma_{ij}(S_{ij}^{\dagger}S_{ij}\ \rho + \rho\ S_{ij}^{\dagger}S_{ij}) \tag{1.7}$$

where Γ_{ij} is the rate of spontaneous emission from level $|j\rangle$ to $|i\rangle$ and $S_{ij} = |i\rangle\langle j|$.

1.1.1 Indium as a Three-Level Lambda System

The indium atomic structure (figure 1.1) can be considered as a three-level Lambda-structure (figure 1.2), if the hyperfine sublevels are neglected. The

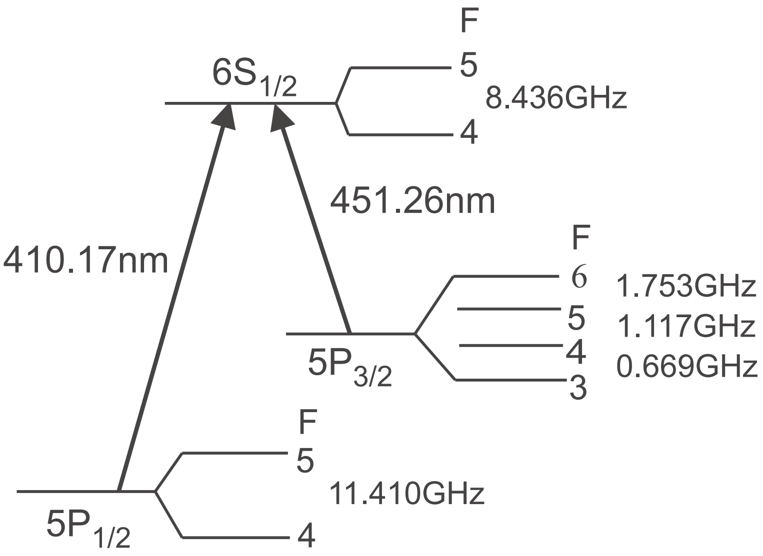

Figure 1.1: *The Indium Level Scheme. The wavelengths indicated are wavelengths in vacuum.*

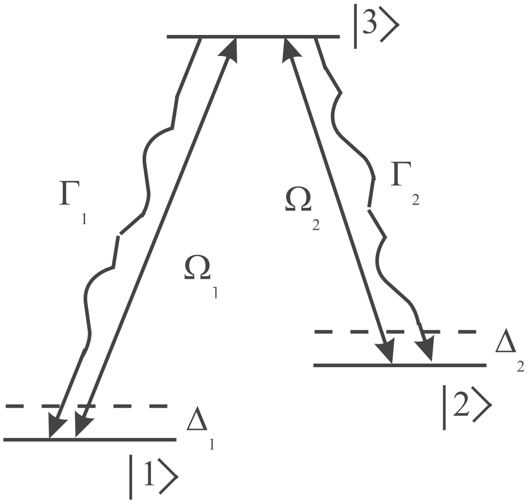

Figure 1.2: *A three-level Lambda system*

evolution of the probability amplitudes, C_i, is as follows [11]:

$$\frac{d}{dt}C(t) = -i\mathbf{H}C(t) \tag{1.8}$$

where

$$\mathbf{H} = \frac{1}{2}\begin{pmatrix} 2\Delta_1 & 0 & \Omega_1 \\ 0 & 2\Delta_2 & \Omega_2 \\ \Omega_1 & \Omega_2 & 0 \end{pmatrix} \tag{1.9}$$

The diagonal elements of **H** are related to the detunings Δ_i and the off-diagonal elements are related to the Rabi frequencies Ω_i. The Rabi frequencies of indium for the relevant J→ J′ transitions and F→ F′ transitions are tabulated in appendix A.

For a 3-level Lambda system, the relaxation matrix can be written as:

$$\hat{L}_{loss}\rho = \frac{1}{2}\begin{pmatrix} 2\Gamma_1\rho_{33} & 0 & -\Gamma\rho_{13} \\ 0 & 2\Gamma_2\rho_{33} & -\Gamma\rho_{23} \\ -\Gamma\rho_{31} & -\Gamma\rho_{32} & -2\Gamma\rho_{33} \end{pmatrix} \tag{1.10}$$

where the relaxation rate Γ is the sum of the two transitions, $\Gamma = \Gamma_1 + \Gamma_2$. The relaxation rate of the $6S_{1/2}$ state of indium is $\Gamma = 2\pi \cdot 25.1\,\mathrm{MHz}$. The lifetime of this state is 6.89 ns. On the other hand, the relaxation rate of the two J→ J′ transitions are as follows [12]:

$6\mathrm{S}_{1/2} \rightarrow 5\mathrm{P}_{1/2}: \quad \Gamma_1 = \Gamma_{410} = 0.56 \cdot 10^8\,\mathrm{s}^{-1} = 2\pi \cdot 8.9\,\mathrm{MHz}$
$6\mathrm{S}_{1/2} \rightarrow 5\mathrm{P}_{3/2}: \quad \Gamma_2 = \Gamma_{451} = 1.02 \cdot 10^8\,\mathrm{s}^{-1} = 2\pi \cdot 16.2\,\mathrm{MHz}$

The relaxation rate Γ_i is a spectroscopic quantity, that can be experimentally determined. This is directly related to the dipole matrix elements through the following equation [11, 13]:

$$[\langle J\|d\|J'\rangle]^2 = \frac{3\mathrm{e}^2\Gamma_i\lambda^3}{32\pi^3 c\alpha}(2J'+1) \tag{1.11}$$

where e is the electron charge, α is the fine structure constant, J' and J are the angular momenta of the upper and lower states, respectively.

Since the interaction Hamiltonian (eqn 1.6) and the relaxation matrix (eqn 1.8) are known, the Liouvillian equation for a 3-level Lambda system can be constructed as follows:

$$\begin{aligned}
\frac{\mathrm{d}}{\mathrm{dt}}\rho_{11} &= \frac{1}{i\hbar}[\frac{1}{2}\Omega_1(\rho_{31}-\rho_{13})] + \Gamma_1\rho_{33} && (1.12)\\
\frac{\mathrm{d}}{\mathrm{dt}}\rho_{22} &= \frac{1}{i\hbar}[\frac{1}{2}\Omega_2(\rho_{32}-\rho_{23})] + \Gamma_2\rho_{33} && (1.13)\\
\frac{\mathrm{d}}{\mathrm{dt}}\rho_{33} &= \frac{1}{i\hbar}[-\frac{1}{2}\Omega_1(\rho_{31}-\rho_{13}) - \frac{1}{2}\Omega_2(\rho_{32}-\rho_{23})] - \Gamma\rho_{33} && (1.14)\\
\frac{\mathrm{d}}{\mathrm{dt}}\rho_{13} &= \frac{1}{i\hbar}[\Delta_1\rho_{13} + \frac{1}{2}\Omega_1(\rho_{33}-\rho_{11}) + \frac{1}{2}\Omega_2\rho_{12}] - \frac{1}{2}\Gamma\rho_{13} && (1.15)\\
\frac{\mathrm{d}}{\mathrm{dt}}\rho_{12} &= \frac{1}{i\hbar}[(\Delta_1-\Delta_2)\rho_{12} + \frac{1}{2}\Omega_1\rho_{32} + \frac{1}{2}\Omega_2\rho_{13}] && (1.16)\\
\frac{\mathrm{d}}{\mathrm{dt}}\rho_{23} &= \frac{1}{i\hbar}[2\Delta_2\rho_{23} + \frac{1}{2}\Omega_2(\rho_{33}-\rho_{22}) + \frac{1}{2}\Omega_1\rho_{21}] - \frac{1}{2}\Gamma\rho_{23} && (1.17)
\end{aligned}$$

If a standing wave is used to drive the atomic transition, the Rabi frequency term has a factor of $\cos(k_i z)$ while for a traveling wave, there is a factor of $e^{ik_i z}$.

1.1.2 Indium as a Six-Level System

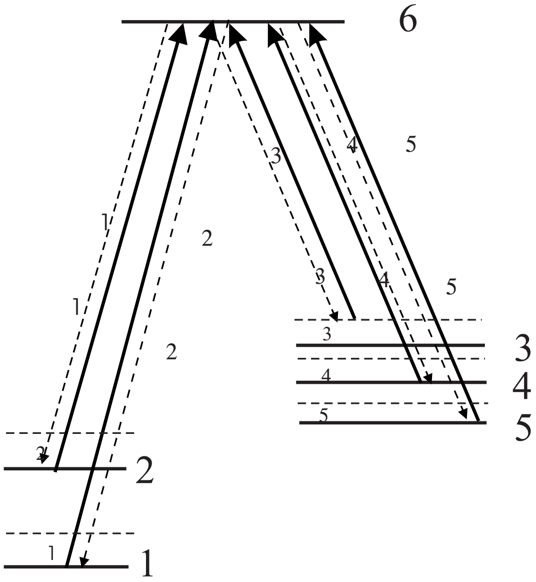

Figure 1.3: *The coupled hyperfine levels for the Indium laser cooling scheme.*

Despite the simplicity of the three-level system, the coupled indium transitions in this experiment are more complicated. The atom and light field are coupled by hyperfine dipole transitions from the five lower states $|5P_{1/2}, F = 4,5\rangle$ and $|5P_{3/2}, F = 4,5,6\rangle$ to the upper $|6S_{1/2}, F = 5\rangle$ state, as shown in figure 1.3. The interaction Hamiltonian for such atomic level transitions is given by:

$$H = \frac{1}{2}\begin{pmatrix} 2\Delta_1 & 0 & 0 & 0 & 0 & \Omega_1 \\ 0 & 2\Delta_2 & 0 & 0 & 0 & \Omega_2 \\ 0 & 0 & 2\Delta_3 & 0 & 0 & \Omega_3 \\ 0 & 0 & 0 & 2\Delta_4 & 0 & \Omega_4 \\ 0 & 0 & 0 & 0 & 2\Delta_5 & \Omega_5 \\ \Omega_1 & \Omega_2 & \Omega_3 & \Omega_4 & \Omega_5 & 0 \end{pmatrix} \tag{1.18}$$

and the relaxation operator $\hat{L}_{loss}$ acting on the density matrix ρ can be constructed from equation 1.9 and can be written as follows:

$$\hat{L}_{loss}\rho = \frac{1}{2}\begin{pmatrix} 2\Gamma_1\rho_{66} & 0 & 0 & 0 & 0 & -\Gamma\rho_{16} \\ 0 & 2\Gamma_2\rho_{66} & 0 & 0 & 0 & -\Gamma\rho_{26} \\ 0 & 0 & 2\Gamma_3\rho_{66} & 0 & 0 & -\Gamma\rho_{36} \\ 0 & 0 & 0 & 2\Gamma_4\rho_{66} & 0 & -\Gamma\rho_{46} \\ 0 & 0 & 0 & 0 & 2\Gamma_5\rho_{66} & -\Gamma\rho_{56} \\ -\Gamma\rho_{61} & -\Gamma\rho_{62} & -\Gamma\rho_{63} & -\Gamma\rho_{64} & -\Gamma\rho_{65} & -2\Gamma\rho_{66} \end{pmatrix} \tag{1.19}$$

The Liouvillian equation in this case gives rise to 36 differential equations, given in appendix B. In our case, we solved this set of equations by numerical integration. The well-known method of continued fractions is not applicable in this case because of the relatively large wavelength difference associated with the two ground states, that is, $\Delta\lambda/\lambda = 0.10$.

1.1.3 Force on a Moving Atom

The force experienced by the atom due the presence of a light field is related to the ground-state population and coherences, which is obtained by solving the Liouvillian equation. The semiclassical force is given by:

$$F(\vec{r},t) = -\langle \nabla H(\vec{r},t)\rangle \tag{1.20}$$

where $\langle\ \rangle$ denotes the expectation value of the force. The interaction Hamiltonian H is given in equation(1.3). The spatial average of the force can be written as:

$$F(\vec{r},t) = -\int_\lambda Tr(\rho\nabla H)dz \tag{1.21}$$

$$F(\vec{r},t) = Tr\,(\sum_n \rho_{0n}\exp(in\omega t)\;\vec{\mathbf{d}}\cdot\hat{\varepsilon}\,\nabla[E_\lambda(\vec{r})e^{-i\omega t-i\phi(\vec{r})} + E^*_\lambda(\vec{r})e^{i\omega t+i\phi(\vec{r})}]) \tag{1.22}$$

The integration over z can be replaced by an integration over time by using $z = \mathrm{v}t$, for moving atoms. The imaginary part of the force is the radiation pressure force, which is due to the gradient of the phase of the electric field $\nabla\,\phi(\vec{r})$. This force is responsible for a type of cooling mechanism known as Doppler cooling, which will be explained in the next section. The real part of the force is the dipole force, which is due to the gradient of the intensity of the electric field $\nabla\,I(\vec{r})$. This force can cause stimulated emission in the high-intensity regime, which leads to a sub-Doppler cooling mechanism [15]. The semi-classical picture of a force on a moving atom is justified when the atomic velocity is much larger than the recoil velocity $v_{rec} = \hbar\mathrm{k}/\mathrm{m}$, where k is the wavenumber of the light wave and m is the atomic mass. This holds

for the case of our indium atomic beam configuration, wherein the transverse velocity is 73 cm/s and the recoil velocity is 8 mm/s.
Using the 6-level atomic structure, the density matrix for each hyperfine level is solved by numerically integrating the Liouvillian equation over the interaction time between the light field and the atom. The initial population is determined by the thermal distribution of the atomic beam. The force can, then, be calculated using equation(1.21). A numerical simulation of the force as a function of velocity will be presented in the last chapter of this thesis, wherein the laser cooling experimental results will be compared with the theoretical simulation.

1.2 Doppler cooling

The simplest mechanism for laser cooling of free atoms uses the Doppler effect. This was proposed by Hänsch and Schawlow [16] in 1975. Three-dimensional laser cooling using radiation pressure was later experimentally demonstrated by S. Chu [17] in 1985.
An atom moving opposite to the propagation direction of a red-detuned laser beam will experience a force due to radiation pressure. In the atom's rest frame, the red-detuned beam appears Doppler-shifted towards higher frequency and is therefore close to resonance. Thus, it will absorb the photon and will undergo subsequent spontaneous emission. However, the net momentum transfer due to spontaneous emission is zero because it occurs in random directions. Only the momentum change due to absorption determines the direction of the radiation force. The atom will then be decelerated in the direction of the laser beam. The spontaneous emission rate limits the maximum deceleration of the atom because it determines the efficiency of the photon absorption process.

When a laser beam interacts with a moving atom, the photon momentum is transferred to the atom. When a red-detuned laser beam propagates in the same direction as the atomic motion, the laser frequency is shifted away from resonance in the reference frame of a moving atom. On the other hand, for a laser beam propagating opposite the direction of atomic motion, the laser frequency is shifted close to resonance. Thus, the atom will absorb more photons from the counter-propagating beam. The counter-propagating laser beam gives more momentum kick to the atom than the beam propagating in the same direction as the atom. This leads to a damping of the atomic velocity. The net force on the atom is given by[19]:

$$\mathrm{F} = \hbar k \gamma_r \tag{1.23}$$

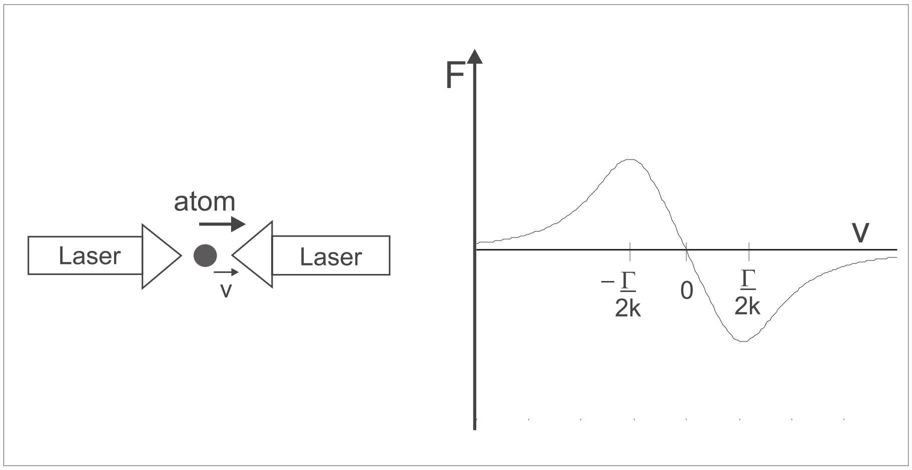

Figure 1.4: *Doppler Cooling. Within the range* $-\Gamma/(2k) \leq v \leq \Gamma/(2k)$*, the Doppler force has opposite sign to the velocity, implying that it is a damping force.*

where γ_r is the scattering rate of the incident photons. In a two-level atom excited by a low intensity light field I, such that the saturation parameter in resonance, $\mathrm{S}_0 = I/I_0$, is less than 1, the scattering rate is given by:

$$\gamma_r = \frac{S_0\Gamma/2}{1 + S_0 + 4((\Delta + \omega_D)/\Gamma)^2} \tag{1.24}$$

where $\omega_D = -\vec{k}\cdot\vec{v}$ is the Doppler shift and I_0 is the saturation intensity for a particular atomic transition. In the presence of two counter-propagating red-detuned laser beams, the average force an atom experiences is given by [20]:

$$\vec{F}_{OM} = -\underbrace{\frac{8\hbar k^2 S_0(|\Delta|/\Gamma)}{(1 + S_0 + (2\Delta/\Gamma)^2)^2}}_{\beta}\,\vec{v} = -\beta\vec{v} \tag{1.25}$$

This is the sum of the force due to each laser beam with all higher orders of $(kv/\Gamma)^4$ are neglected. Note that the damping force in equation (1.25) is valid only for $S_0 \ll 1$.

There must be sufficient scattering events for the atoms to experience a reasonable radiation pressure force. Thus, the atoms must interact with the light field for a long period of time. For moving atoms, the interaction time is related to the interaction length. If we consider Indium as a two-level atom, we can calculate the interaction length which is sufficient to realize Doppler cooling from the saturation parameter S_0, the decay rate Γ, and the number of pumping cycles N_{pump}. If N_{pump} is estimated to be 1000, and S_0

= 1, then the required interaction length, l, is 6 mm for laser cooling with the $5P_{3/2} \rightarrow 6S_{1/2}$ transition.

The atoms can not reach zero temperature ($v = 0$) by Doppler cooling because of the random nature of the momentum 'kicks' the atom experiences. These recoil events cause heating which can be described as a diffusion process, or a random walk around $\langle \mathrm{p} \rangle = 0$ in momentum space. There are two competing processes, cooling due to the scattering and heating due to recoil. Eventually, these two processes will reach a steady-state condition [19]:

$$F_{OM} \cdot v = 4\hbar\omega_r\gamma_r \tag{1.26}$$

where ω_r is the recoil frequency and γ_r is the scattering rate. At steady-state, the kinetic energy is found to have a minimum at $|\Delta| = \Gamma/2$, which leads to an equilibrium temperature known as the Doppler temperature or Doppler limit, T_D. The Doppler temperature and recoil temperature for indium is tabulated in Appendix C.

There are other cooling mechanisms which lead to temperatures two orders of magnitude lower than the Doppler limit. These mechanisms are based on optical transitions in multilevel atoms, which gives rise to multiple interaction strengths (Rabi frequencies), depending on the atomic dipole orientation relative to the light polarization. In this thesis, two of these sub-Doppler cooling mechanisms will be discussed in the succeeding sections, one is dipole force cooling by stimulated emission and the other is polarization-gradient cooling.

1.3 Stimulated Emission Cooling from the Dipole Force

The dipole force arises from the interaction of a spatially-varying electric field of a laser beam and the induced dipole moment of the atom. The electric field shifts the energy level of the atom in proportion to the field intensity. This is known as the AC Stark effect. In the low intensity regime, $\Omega \ll |\Delta|$, and for a red-detuned laser beam, the light shift creates a potential well for the ground state. The atoms are attracted to the node of the potential well or the region with relatively high intensity as shown in figure 1.5. This attractive force, however, is conservative and it does not cool the atoms.

In the high-intensity regime ($\mathrm{S} \gg 1$) and for a blue-detuned laser beam, the dipole force can lead to a phenomenon called stimulated emission cooling. Stimulated emission leads to the coherent redistribution of photons between the two counterpropagating waves [21]. Atomic momentum is transferred

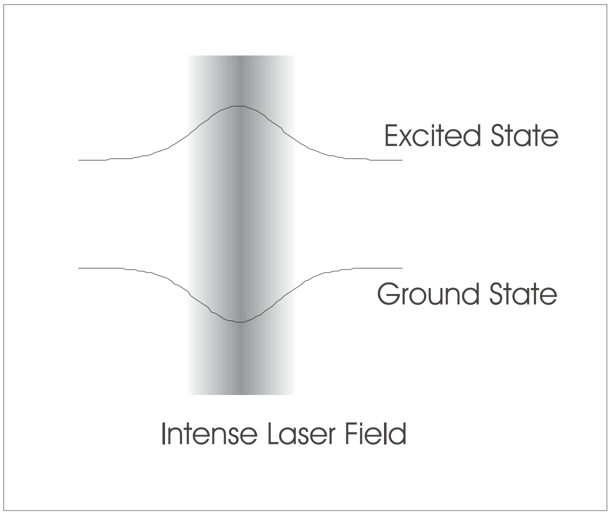

Figure 1.5: *AC Stark shift*

to laser photons by stimulated emission processes. This phenomenon can be best described in the dressed-atom picture. The eigenstates of the atom plus laser periodically oscillate in space, as shown in figure 1.6. The dressed-states coincide with the unperturbed states only at the nodes of the standing wave. At any point in the standing wave, not at the node, the dressed states are linear combinations of the unperturbed excited state $|e,n\rangle$, and the ground state with a higher energy due to photon absorption $|g,n+1\rangle$. The energy splitting between the dressed-states is maximum at the antinodes of the standing wave.

It is important to note that the spontaneous emission rates vary in space. The atoms has a preferred position in the standing wave where it undergoes spontaneous emission. Consider the dressed-states as shown in figure 1.6, an atom at energy level $|2,n\rangle$, with its position at the node of the standing wave, where $|2,n\rangle = |e,n\rangle$, it has maximum probability to decay. If the atom is at the antinode, where $|2,n\rangle$ is mixed with $|g,n+1\rangle$, it has a minimum probability to decay. The atom starting at a node of the standing wave at $|1, n+1\rangle$, will climb the potential hill, and then undergo spontaneous emission to $|2,n\rangle$, from where it will again undergo another cycle of climbing a potential hill or it will decay to $|1,n\rangle$, where it will experience a slight velocity change due to recoil, but it will not have, on average, a kinetic energy change. For an atom which decays to $|2,n\rangle$, its kinetic energy is transformed into potential energy as it climbs a potential hill, and successive cycles of stimulated emission will cause a decrease in its kinetic energy. This is a Sisyphus-type cooling mechanism, in which the atomic velocity is decreased due to stimulated emission cycles.

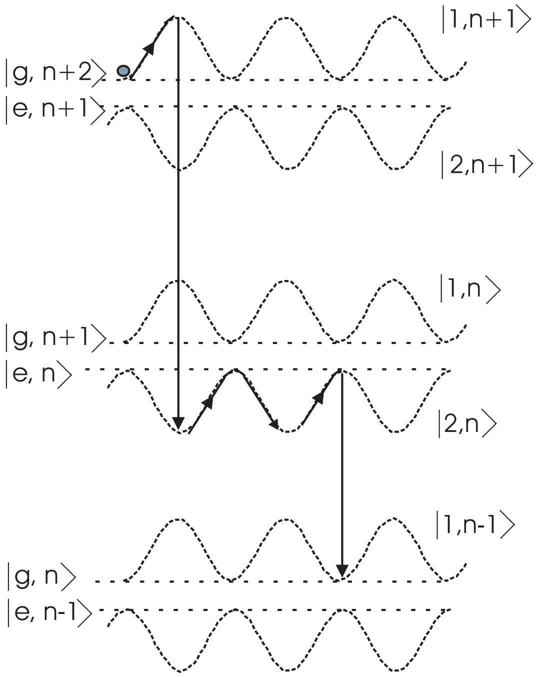

Figure 1.6: *Laser cooling by stimulated emission, adapted from reference [21]. The dressed-states energy levels are shown. The atomic trajectory is illustrated by the solid line. As the atom undergoes a series of spontaneous emission at a preferred position in the standing wave, its kinetic energy decreases.*

1.4 Polarization-gradient Cooling

When the electric field polarization varies spatially along the trajectory of the atom, this leads to a different type of cooling mechanism, which is known as polarization-gradient cooling. A spatially-varying polarization along the direction of motion of the atom leads to a change in its steady-state population due to optical pumping. This gives rise to an anisotropy in the ground state Zeeman sublevels. The change in population takes a finite time, which is the optical pumping time, to occur. This is a non-adiabatic effect, which leads to a momentum change in the atomic motion. The laser field not only produces optical pumping, but it also induces a light shift, which is different for each Zeeman sublevel. This light-shifted energy is also spatially-varying and this leads to a gradient of the interaction potential, or a force that slows down a moving atom.

Lin ⊥ Lin Configuration

In a lin ⊥ lin configuration, the polarization directions of two counter-propagating linearly-polarized light fields are orthogonal to each other and the polarization varies along the propagation direction z, depending on its wavelength λ. The polarization varies in space as shown in figure 1.7. At z=$\lambda/8$, the polarization is σ- and at z= $\lambda/4$, the polarization is linear. Due to this polarization gradient, there is a cooling force which slows down the atom. This can be intuitively explained as a Sisyphus effect, as shown in figure 1.7.

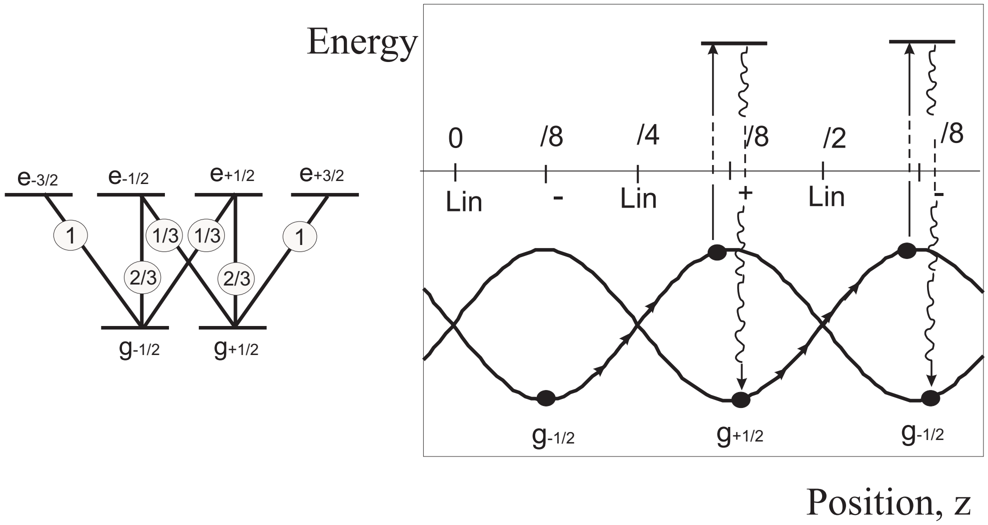

Figure 1.7: *Light-shifted energies for the J=1/2 ground state in a lin ⊥ lin configuration and for red-detuned light field. The polarization as a function of position in a lin ⊥ lin configuration is as well indicated.*

If the light field is red-detuned, the light-shifted energy of the Zeeman ground state sublevels is lower than the unperturbed energy, as shown in figure 1.7. The light-shifted energy is spatially-varying due to the polarization-gradient. An atom, initially at a position z=$\lambda/8$, will climb the potential hill until it is optically pumped to the next Zeeman sublevel, which in this case, the $g_{+1/2}$ sublevel. The time it takes for the atom to move through this distance is given by the optical pumping time, τ_p. When the atom is at the $g_{+1/2}$ sublevel, it will again climb another potential hill. Thus, the atom loses kinetic energy most of the time.

For the indium cooling scheme, there are 60 Zeeman sublevels for all allowed hyperfine transitions of $5P_{1/2} \rightarrow 6S_{1/2}$ and $5P_{3/2} \rightarrow 6S_{1/2}$. If all these $F \rightarrow F'$ transitions are excited by counter-propagating light fields with polarization-gradient, then the populations and coherences for all 60 Zeeman sublevels, should be solved in order to estimate the damping force.

Chapter 2

Experimental Set-up

Several optical-frequency sources are necessary to manipulate the indium atomic beam using a Lambda-cooling scheme. Five hyperfine transitions should be driven by five optical frequencies, in order to avoid optical pumping in a non-coupled state. These frequencies are provided by two GaN diode lasers and a frequency-doubled Ti:Sapphire laser which serves as a carrier beam, modulated by an electro-optic modulator (EOM) and an acousto-optic modulator (AOM) to excite the different hyperfine transitions, as shown in figure 2.1.

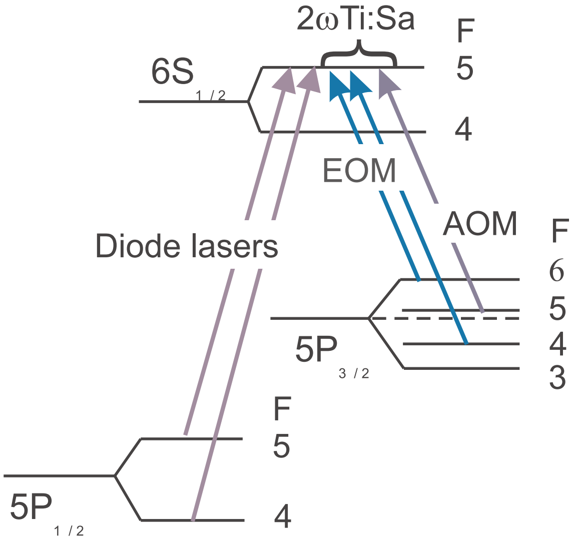

Figure 2.1: *The indium level scheme and the corresponding laser sources for exciting the transitions of interest.*

To achieve one-dimensional transverse laser cooling, the atomic beam is always perpendicular to the laser beams at the cooling region. The atomic beam has a full divergence of 2.7 mrad. Different light-field configurations and different combinations of light sources were employed to understand which driven atomic transition contributes to the cooling effect. One of the laser cooling configurations is shown in figure 2.2, wherein the 410 nm and 451 nm light sources are overlapped using a dichroic mirror. Details of the light sources used in our experiment and the atomic beam source will be discussed in this chapter.

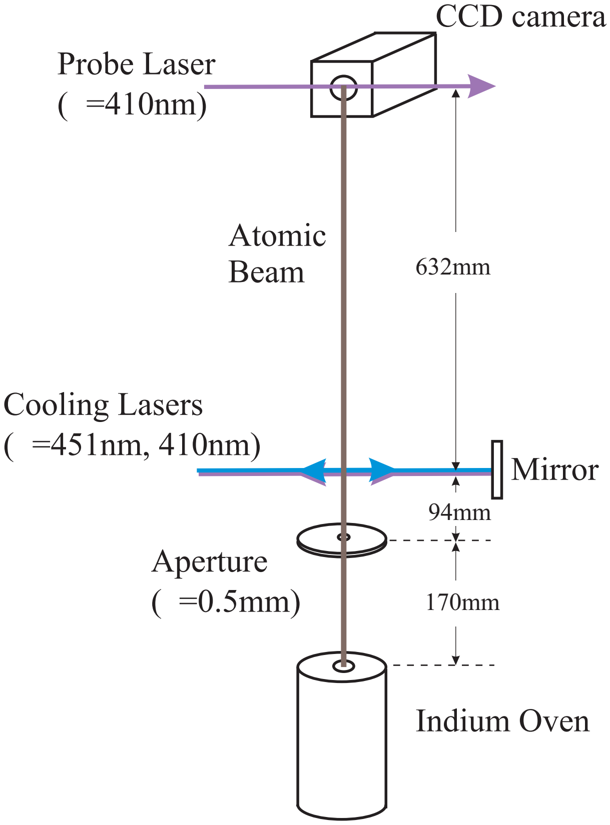

Figure 2.2: *One configuration we investigated in order to observe laser cooling of an indium atomic beam.*

2.1 Lasers

2.1.1 GaN diode laser

The 410 nm transition of the Indium atomic level is excited by a single-frequency GaN diode laser [22], with an external grating in a Littrow configuration. For our applications, we need both a narrow linewidth, on the order of 10MHz, and a large mode-hop free tuning range of 20 GHz. This can be realized by placing the diode laser in an extended cavity (Extended Cavity Diode Laser, ECDL). In this configuration, a diffraction grating is placed after the out-coupling facet of the diode laser. The first-order beam is reflected by the grating into the diode laser, while the zeroth order is used for the experiment. To tune the ECDL over different output wavelengths, one should change either the current, or the temperature of the diode laser or both, or tilt the diffraction grating. To scan the ECDL over a large wavelength range, one needs to move the piezo, which is attached to the grating, over a certain distance. This can be done by scanning the voltage applied to the piezo. A mode-hop free large tuning range of 12GHz can be realized by applying an additional feed-forward current proportional to the scanning voltage. The linewidth of the diode laser in our experiment is 10 MHz. In our experiment, we use a DL100 system, supplied by Toptica. The laser has an output power of 12mW after the grating and an elliptical cross-sectional area of $1.5 \times 3\,\mathrm{mm}^2$.

2.1.2 The Ti:Sapphire laser

In this experiment, we use a frequency-doubled Ti:Sapphire laser to generate the 451nm light. The Ti:Sapphire laser is an MBR-110 model, produced by Microlase Optical Systems. It is a bow-tie ring laser, embedded in a monolithic aluminum block, which makes the whole system mechanically stable. One remarkable feature of this laser is its relatively large tuning range while operating in single frequency. A tuning range of 3 GHz, covering the three hyperfine indium transitions at $5P_{3/2} \rightarrow 6S_{1/2}$, can be achieved. To have single-direction operation, the Ti:Sapphire laser employs an optical diode while running in a ring configuration to eliminate any spatial-hole-burning effects in the gain medium.

To set the laser at the right wavelength (902 nm), a birefringent filter inside the Ti:Sapphire laser is used to coarsely control the wavelength. For single-mode operation, a thin etalon inside the laser cavity is used to select the laser-mode. The etalon angular position is locked to the laser frequency using a locking scheme, employing phase-sensitive detection and a lock-in amplifier, included in the Microlase electronic circuitry. This locking scheme ensures a modehop-free operation while the laser wavelength is being scanned. Long-term laser stability is obtained by using an external Fabry-Perot reference cavity, with a side-fringe locking scheme. The external reference cavity actively controls the laser cavity length by controlling the piezo attached to one of the laser mirrors and the galvo-plates inside the laser cavity. A laser linewidth of 100 kHz is the best attainable linewidth for this model. During our experiment, an external voltage ramp is used to scan the reference cavity of the Ti:Sapphire in order to fine-tune its output frequency. However, we do not actively stabilize the laser to an atomic transition as we could not find a suitable transition line in a spectroscopic cell at the 451 nm wavelength.

The typical operating power of the Ti:Sapphire laser at 902 nm wavelength is 800 mW for a pump power of 10 W. The pump laser of the Ti:Sapphire is a Millenia X, frequency-doubled Nd:YAG diode-pumped laser. The output beam of the Ti:Sapphire laser has a Gaussian profile.

2.1.3 Frequency-doubling cavity

In this section, we explain the principle behind second harmonic generation and apply this concept to frequency-doubling in a LiB_3O_5 (LBO) crystal and in a periodically-poled $KTiOPO_4$ (ppKTP) crystal. During the first phase of this experiment, a second-harmonic generation cavity with an LBO crystal is used, and in the second phase, a ppKTP crystal is used. The reason for changing the crystal is that the LBO conversion efficiency degrades over time, which is due to the strong tendency of LBO to absorb water. This water absorption changes its crystal structure and thus, is detrimental to its performance.

Second harmonic generation can be achieved when an intense laser beam is incident into an anisotropic, birefringent crystal. The nonlinear response of the crystal can cause its polarization to develop new frequency components of the electromagnetic field. Theoretical analysis of second-order nonlinear effects has been discussed by Armstrong et al. [23] in 1962. The nonlinear polarization in the presence of an intense electromagnetic field is given by:

$$P_i(\omega_3) = \varepsilon_0 \sum_{j,k} \chi^{(2)}_{i,j,k}(\omega_3, \omega_1, \omega_1) E_j(\omega_1) E^*_k(\omega_1) \tag{2.1}$$

where the i,j,k refer to the cartesian components of the field. Now, if we define the electric field of the laser beam and the nonlinear polarization to be:

$$\begin{aligned} \tilde{E}_j(z,t) &= \sum_n E_j(z,\omega_n) e^{-iw_n t} + c.c. & (2.2) \\ &= E_j(z,\omega_1)^{-i\omega_1 t} + E^*_j(z,\omega_1) e^{i\omega_1 t} \qquad \text{for n=1} & (2.3) \\ \tilde{P}_i(z,t) &= \sum_n P_i(z,\omega_n) e^{-i\omega_n t} + c.c. & (2.4) \end{aligned}$$

Expanding the summation in equation 2.1, one of the terms yields the second-order polarization, which can be written as

$$\tilde{P}^{(2)}(t) = \varepsilon_0 \chi^{(2)} [\underbrace{E^2 e^{-2i\omega t} + (E^*)^2 e^{2i\omega t}}_{2\omega - term} + \underbrace{2EE^*}_{DC - term}] \tag{2.5}$$

where ε_0 is the dielectric constant in vacuum and $\chi^{(2)}$ is the second-order nonlinear susceptibility. The 2ω-terms show that there is an electromagnetic field created, with a frequency twice that of the incident radiation field, which is known as the second harmonic beam. On the other hand, the DC-term is known as optical rectification.

Phase Matching

Inside the nonlinear crystal, the fundamental wave and the second-harmonic wave propagate with different phase velocities due to dispersion. Phase matching occurs when the fundamental wave and the second harmonic wave oscillate in phase with each other. The intensity of the second-harmonic beam depends on how well the phase matching condition is fulfilled. The phase mismatch parameter, Δk, is given by:

$$\Delta k = k_{2\omega} - 2k_{\omega} = \frac{2\omega}{c}(n_{2\omega} - n_{\omega}) \tag{2.6}$$

where $k_{2\omega}$, k_{ω} are the wavenumbers of the second harmonic beam and fundamental beam, respectively, $n_{2\omega}$, n_{ω} are the refractive indices of the second harmonic and fundamental beams, respectively. The intensity of the second-harmonic beam $I_{2\omega}$ is related to the phase mismatch by the equation [24]:

$$I_{2\omega} = \kappa^2 l^2 I_{\omega}^2 \frac{sin^2(\Delta kl/2)}{(\Delta kl/2)^2} \tag{2.7}$$

where κ^2 is a constant related to the effective dielectric constant of the crystal and the indices of refraction for both fundamental and second-harmonic beams, l is the crystal length, and I_{ω} is the intensity of the fundamental beam. The conversion coefficient κ^2 is related to the nonlinear coupling coefficient, d_{eff}, by:

$$\kappa^2 = \frac{4d_{eff}^2\omega^2}{c^3\epsilon_0 n_{\omega}^2 n_{2\omega}}. \tag{2.8}$$

When there is a phase difference between two second-harmonic beams generated at different planes, say plane z_1 and plane z_2, the two beams interfere. The separation between two adjacent peaks of this spatial interference pattern is known as the coherence length, l_c [25]. The coherence length is a function of the refractive indices of the fundamental beam and the second-harmonic beam, n^{ω} and $n^{2\omega}$, respectively.

There are two methods to achieve phase-matching, one is by angle-tuning and another by temperature-tuning. Phase-matching using angle-tuning can be achieved by aligning the angle between the fundamental beam and the optical axis of the crystal such that the power of the second harmonic beam is maximized. When one uses only angle-tuning for phase matching, there is a walk-off due to the different group velocities of the fundamental and second-harmonic beams, which leads to a decrease in the conversion efficiency. The propagation vectors of the ordinary and extra-ordinary rays diverge from each other while propagating inside the crystal. Thus, one can fix the angle between the propagation vector and the optical axis of the crystal at 90° and vary the crystal temperature until phase-matching is achieved. This is known as temperature-tuning. Temperature-tuning is used to obtain phase matching for crystals whose degree of birefringence is strongly dependent on temperature [27]. Phase matching in the LBO crystal used in our experiment is achieved by angle-tuning.

Quasi-Phase Matching (QPM)

Another way to realize phase matching without using angle-tuning is by periodically varying the nonlinear susceptibility of the crystal. For some materials, the birefringence is not sufficient to compensate for dispersion, which causes a large phase mismatch. To solve this issue, quasi-phase matching was introduced, wherein the sign of the nonlinear coupling coefficient, d_{eff}, of the material is changed periodically along the crystal length.

When there is a phase mismatch between the fundamental and the second-harmonic beams, the power is coupled alternately from one beam to the other, as shown in curve C of figure 2.3. In order for the second-harmonic power to grow monotonically, the phase must be changed back to its original value periodically to satisfy proper phase-matching. As the second-harmonic power decreases due to phase mismatch, the sign of d_{eff} is inverted. The relative phase is, thereby, inverted and the power flow is reversed, leading to a monotonic increase of the second-harmonic power, as shown in curve B of figure 2.3. The geometrical period length of d_{eff} in the crystal, denoted by Λ, is related to the quasi-phase matching condition, $\Delta k = 2\pi m/\Lambda$. For the ppKTP crystal we have in our experiment, the grating period is $5.15\mu m$, corresponding to our pump beam wavelength of 902nm, and this can be calculated using the Sellmeier equation [31]. Creation of a grating structure in ppKTP can be realized by applying electric field pulses through periodic electrodes on the crystal surface [32].

The second harmonic power can be increased by focusing a Gaussian fundamental beam into the crystal, with the right beam waist at the center of the crystal such that no large divergence occurs. The Boyd-Kleinmann reduction factor describes the decrease in second harmonic output power caused by walk-off due to focusing. From Boyd-Kleinman reduction factor,

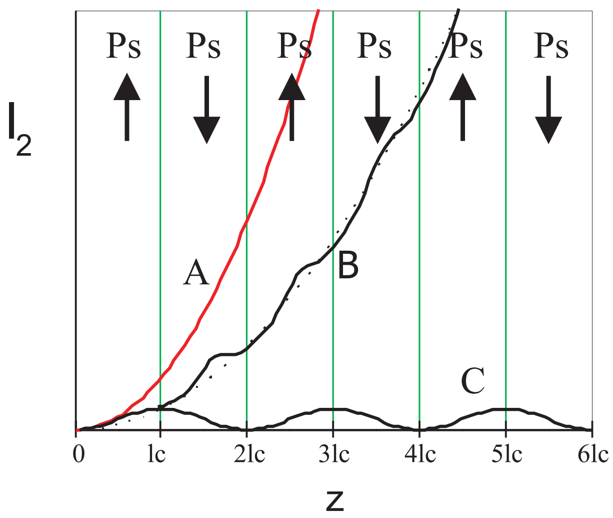

Figure 2.3: *Comparison of the spatial dependence of the intensity of the second-harmonic beam for the different phase matching conditions. The label P_S denotes spontaneous polarization of the crystal. (A)Phase matching is perfectly satisfied. (B)Quasi-phase matching is achieved with the c-axis of the crystal modulated with a period equal to twice the coherence buildup length, lc.(C) Non-phase matched interaction.*

one generally obtains the optimum value of the Rayleigh length, z_R, of the fundamental beam relative to the crystal length, l, and this is found to be $l = 3z_R$.

Second Harmonic Cavity for Power Enhancement

Another way to achieve power enhancement of the second harmonic beam is by 'recycling' the light through the crystal and this can be realized by placing the crystal in a resonator. The maximum second harmonic power that can obtained in a cavity is given by the implicit equation[29]:

$$P_{2\omega} = \frac{16T^2\eta_{sp}P_\omega}{(2-\sqrt{1-T}(2-A-\sqrt{\eta_{sp}P_{2\omega}}))^4}, \tag{2.9}$$

where $\eta_{sp} = P_{2\omega}/P_\omega^2$ is the single-pass conversion efficiency, T is the transmission of the in-coupling mirror, and A is the absorption of the resonator. In our experiment, two different resonators are built for each crystal, as shown in figure 2.4. For the LBO crystal, the cavity was designed by J. Wang [26]. It has a finesse of 136. Its typical second-harmonic power is 60 mW at 451 nm for a pump power of 1W and the maximum power is 100 mW. For the ppKTP

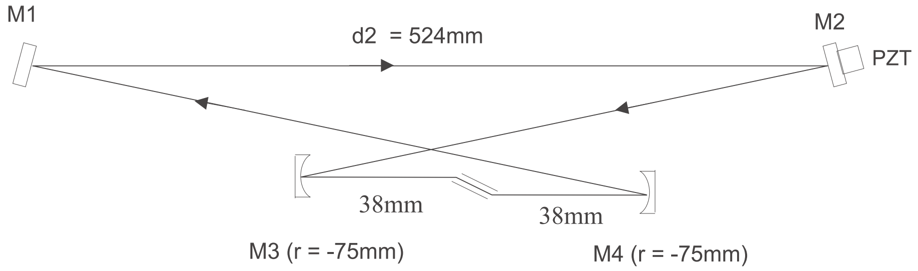
Frequency-doubling cavity (LBO)

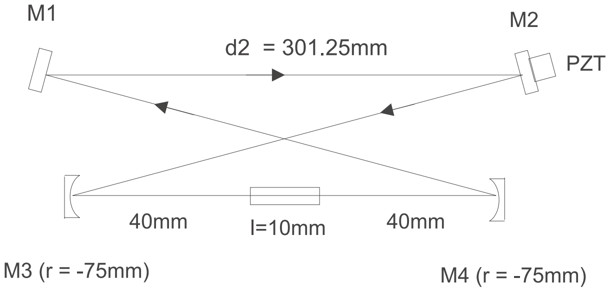
Frequency-doubling cavity (ppKTP)

Figure 2.4: *Diagram of the bow-tie ring resonator for the LBO crystal and for the ppKTP crystal. M1 and M2 are plane mirrors, whereas, M3 and M4 are curved mirrors, with a radius of curvature, r. The parameter d2 indicated in the figure is the total distance of the circulating beam from M4 to M1 to M2 and, lastly, to M3.*

crystal, the parameters of the cavity were calculated by S. Metz [30]. The finesse of this cavity is 89 (refer to figure 2.5). Due to quasi-phase matching, the ppKTP crystal has a higher conversion efficiency. In a ring-cavity, it has maximum transmission of 81.4% and it delivers a maximum power of 160 mW at 451 nm for a pump power of 700 mW. The relevant parameters of the crystals and the frequency-doubling cavities are tabulated in table 2.1.

Hänsch-Couillaud Stabilization

In order to obtain the maximum power of the cavity, it has to be stabilized

Points of Comparison	LBO crystal	ppKTP crystal
Crystal Dimensions	$3 \times 3 \times 10mm^3$	$6 \times 1 \times 10mm^3$
Type of Phase Matching	Angle-tuning	QPM, Temperature Tuning
Nonlinear Coupling Coefficient, d_{eff}	-0.905pm/V	10pm/V
Single-Pass Conversion Efficiency	$2.5 \times 10^{-5}W^{-1}$	$3W^{-1}$
Maximum Conversion Efficiency in a Ring Configuration, $\eta = P_{2\omega}/P_\omega$	10%	23%
Advantage	Less sensitive to temperature	Higher conversion efficiency, Less sensitive to moisture

Table 2.1: *Comparison between the LBO crystal and the ppKTP crystal.*

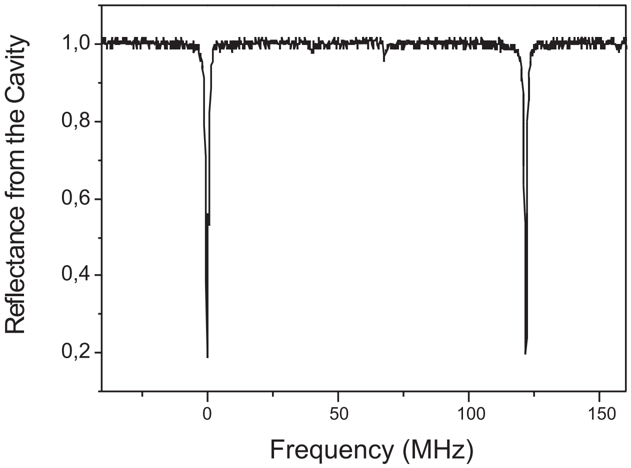

Figure 2.5: *Reflectance fringes from the ppKTP frequency-doubling cavity.*

such that the cavity is in resonance with the fundamental wavelength. We use the Hänsch-Couillaud scheme [28] for stabilizing the cavity, as shown in figure 2.6. The linear polarization of the reflected beam from the cavity becomes elliptically polarized when the cavity is not in resonance with the fundamental beam. A linearly-polarized fundamental beam, incident to a birefringent crystal at some angle θ, can be decomposed into two components, one field parallel and another perpendicular to the resonator plane, as follows:

$$\begin{aligned} E_{\parallel,in} &= E_{in} cos\theta && (2.10) \\ E_{\perp,in} &= E_{in} sin\theta. && (2.11) \end{aligned}$$

The parallel component experiences low loss and has a phase shift when it is reflected from the cavity. The perpendicular component serves as a reference. The complex amplitude of the parallel component of the reflected beam is [28]:

$$E_{\parallel,r} = E_{\parallel,in}[\sqrt{R_1} - \frac{T_1 R}{\sqrt{R_1}} \frac{\cos\vartheta - R + i\sin\vartheta}{(1-R)^2 + 4Rsin^2(\vartheta/2)}] \tag{2.12}$$

where R_1 and T_1 are the reflectivity and the transmission of the in-coupling mirror M_1, ϑ is the phase shift between the parallel and perpendicular components, and R accounts for all cavity losses, such as reflection from the crystal facets and the input and output coupling mirrors. The perpendicular component of the reflected beam is given by:

$$E_{\perp,r} = E_{\perp,in}\sqrt{R_1}. \tag{2.13}$$

When the cavity is not in resonance, the parallel component has a phase shift relative to the perpendicular component, due to the presence of an imaginary part of $E_{\parallel,r}$ as seen from eqn. (2.10). The reflected beam has an elliptical polarization, which is decomposed into two orthogonal linearly-polarized beams by the $\lambda/4$ plate and the polarizing beamsplitter. These two linearly-polarized beams are detected by the photodiodes. The signals from the photodiodes are, then, subtracted using a differential amplifier circuit to obtain a dispersive-shaped signal. The difference signal depends on the magnitude and handedness of the ellipticity. The slope of the dispersive signal with a zero-crossing is used as an error signal for locking the cavity. The error signal for the ppKTP cavity is shown in figure 2.7. This is obtained while scanning the piezo connected to one of the cavity mirrors and the difference signal between the two polarization components is monitored.

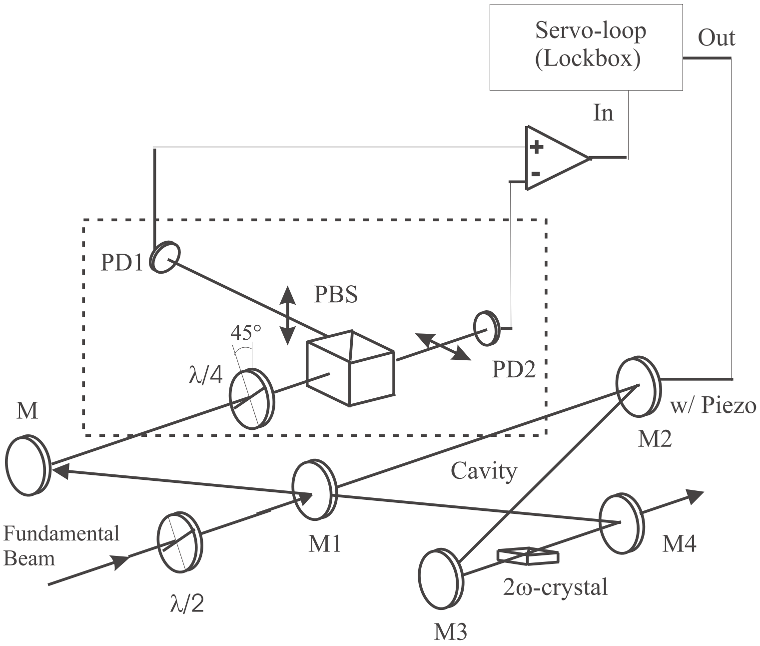

Figure 2.6: *Hänsch-Couillaud stabilization scheme and a sketch of the frequency-doubling cavity. The polarization of the two components of the reflected beam are indicated in the figure. The intensities of the two orthogonal components of the reflected beam are subtracted using a differential amplifier. The difference signal is used as an input to a servo-loop circuit, which is used for locking the cavity.*

Temperature Stability of the ppKTP cavity

One technical challenge we have encountered is the temperature stability of our ppKTP cavity. Since the birefringence of the crystal depends on the temperature, any temperature drift changes the optical output of the crystal. The crystal is placed inside an oven with peltier element to actively control the temperature by a feedback circuit. Furthermore, a water-cooling slab is placed above the crystal oven to fully-dissipate the heat.

2.2 Optical multi-frequency sources

The frequency-doubled Ti:Sapphire laser beam is incident to an electro-optic modulator (EOM) and an acousto-optic modulator (AOM) in order to optically-excite the three hyperfine transitions, $|5P_{3/2}, F = 6, 5, 4\rangle \rightarrow |6S_{1/2}, F = 5\rangle$. The two sidebands of the EOM are tuned to the $F =$

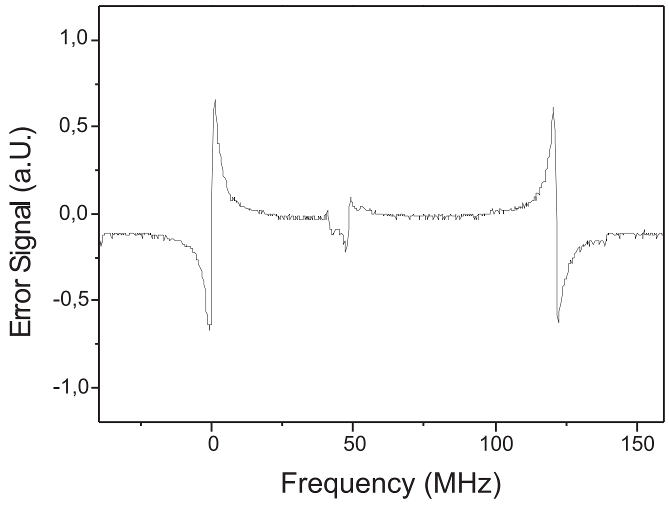

Figure 2.7: *Error signal for locking the ppKTP cavity. This is the output signal of the differential amplifier circuit when the inputs are the two polarization components of the reflected beam from the cavity.*

$6 \rightarrow F' = 5$ and $F = 4 \rightarrow F' = 5$ hyperfine transitions. The AOM shifts the carrier frequency higher, so that the first-order beam is tuned to the $F = 5 \rightarrow F' = 5$ hyperfine transition, as shown in figure 2.8. The experimental setup is shown in figure 2.9. The carrier beam is split into two, using a polarizing beamsplitter, and their relative intensities are adjusted using a $\lambda/2$ plate. The output beams from the EOM and AOM are combined using a polarizing beamsplitter. The combined beam has two different polarizations. The polarization of the EOM output beam is orthogonal to that of the AOM. For polarization-gradient cooling with all hyperfine transitions, this factor should be considered.

The EOM (New Focus model 4421) produces two sidebands with a frequency of 1435 MHz away from the incident carrier frequency. The RF source is supplied by Marconi Instruments model-2032 signal generator. The RF power is set at 33.5 dBm after the amplifier, and directly supplied to the EOM. To determine the appropriate RF power, the output beam from the EOM is incident into a Fabry-Perot cavity with a free-spectral range of 1.5 GHz. The carrier beam, the first and second-order sidebands are resolved by the Fabry-Perot cavity. The relative amplitudes of the carrier and sidebands are monitored while changing the RF power. The RF power is set such that the power of each first-order sideband is 33% of the incident optical power.

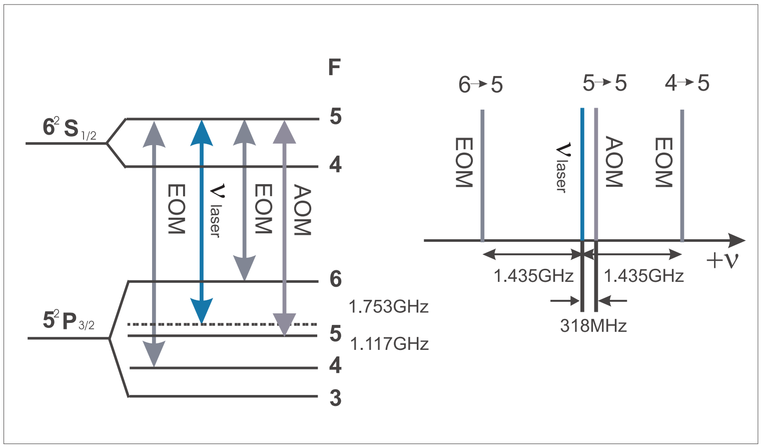

Figure 2.8: *The different hyperfine transitions are excited using an EOM and an AOM. The EOM sidebands are tuned to the 6⟶5 and 4⟶5 transitions, while the AOM first-order beam is tuned to the 5⟶5 transition.*

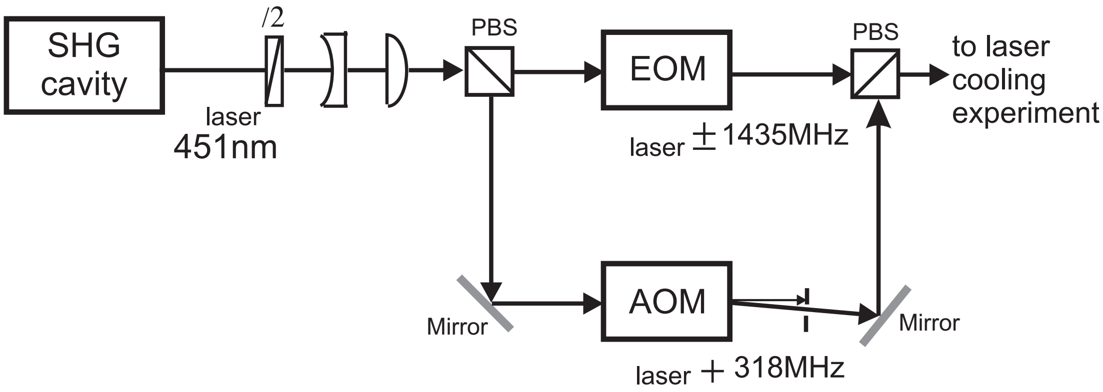

Figure 2.9: *Experimental set-up of the 451nm light source, from the second-harmonic generation (SHG) cavity, to the EOM and AOM modulators, which are used to generate the three frequency components. A polarizing beamsplitter (PBS) is used to separate and to recombine the beams of the EOM and the AOM. The lenses are used to change the beam size so that the beam passes through both apertures of the EOM and the AOM without any clipping.*

The AOM (AA Optoelectronics, model AA.ST.318) frequency is set at 318 MHz. To set the AOM frequency, the input voltage of the AOM driver is adjusted while monitoring the frequency of the RF signal to the AOM with a spectrum analyzer. The first-order beam from the AOM, which shifts the carrier beam higher in frequency is spatially-selected using an aperture. The AOM output beam has a maximum transmission of 87%.

To check if the EOM and AOM frequencies are on resonance with the three hyperfine transitions, the combined output beam from the EOM and AOM is incident perpendicular to the atomic beam. The fluorescence signal is detected using a photomultiplier, using fluorescence spectroscopy which will be described in chapter 3. The carrier beam (451 nm light source) is scanned over a minimum range of 3 GHz. With both EOM and AOM turned-off, a fluorescence signal is detected as shown in figure 2.10. When the EOM and AOM are turned-on, additional fluorescence peaks are seen, as shown in figure 2.11, because there are more optical frequencies in resonance with the atomic hyperfine transitions. The large fluorescence peak in figure 2.11 corresponds to the event when the EOM and AOM outputs simultaneously excite the three hyperfine transitions. As one changes the EOM or AOM frequency, this fluorescence peak changes in amplitude and linewidth. When its amplitude is maximum and its linewidth is minimum, the EOM and AOM frequencies are properly set. This corresponds to a condition when the combined output beam from the EOM and AOM excites the $|F = 6, 5, 4\rangle \rightarrow |F' = 5\rangle$ transitions simultaneously.

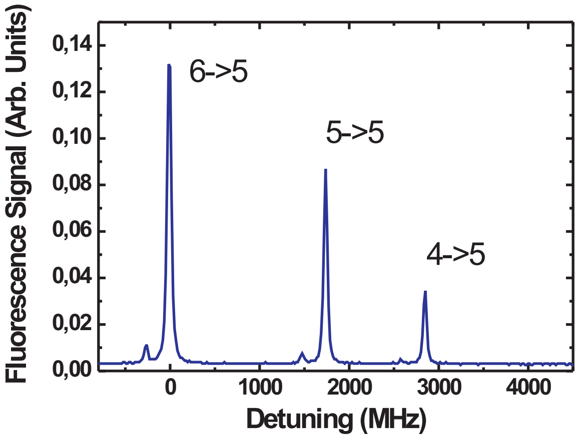

Figure 2.10: *Fluorescence signal of the atomic beam when it interacts with the 451nm laser. Only the carrier beam is scanned across all three hyperfine transitions.*

2.3 Vacuum system and the atomic beam

The atomic beam is produced by an effusive oven with an aperture of 1mm in diameter. The operating temperature of the oven is 1200°C, provided by

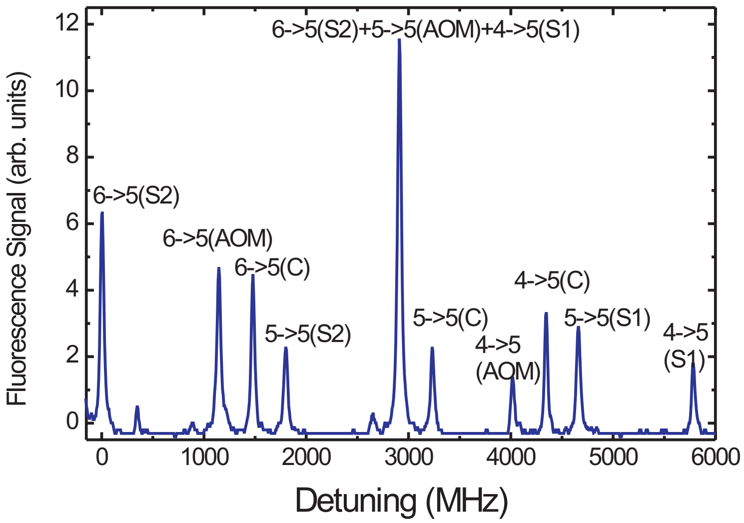

Figure 2.11: *Fluorescence signal of the atomic beam when it interacts with the 451nm laser, carrier plus EOM sidebands and first-order AOM output beam. The carrier beam (C) is scanned across all three hyperfine transitions. The two sidebands (S1 and S2) from the EOM and the frequency-shifted beam from the AOM produces additional fluorescence peaks.*

tungsten heating wires, with a current of 8 A, and controlled by an automated temperature controller. The oven is placed in a cylindrical shielding with water-cooling to dissipate the heat. To prevent indium from condensing at its rim, when the temperature is being lowered, there is an additional heating wire at the rim, called the hotlip, with a current of 2.5 A. The vacuum chamber for housing the atomic beam is pumped by a turbo-molecular pump (Turbo-V 250, Varian), to give a pressure of 10^{-8} Torr, which is sufficient for laser cooling experiments.

Molten indium easily adheres to the steel surface of the vacuum chamber and to the windows of the vacuum chamber. Thus, a water-cooled copper shield, with an opening of 5 mm, is placed above the oven to minimize the amount of indium deposited everywhere in the chamber, refer to Figure 2.12. A $1 \times 5\, mm^2$ slit is attached to the copper shield to partly define the atomic beam trajectory. Another aperture with a diameter of 0.5 mm is placed below the chamber for the laser cooling experiments. The oven aperture size and the 0.5 mm-aperture defines the atomic beam trajectory.

The collimation ratio, κ, due to the two apertures is 4.4 mrad and it can be obtained from the relation:

$$\kappa = \frac{\phi_1 + \phi_2}{2 \cdot d} \tag{2.14}$$

where ϕ_1 is the oven aperture size of 1 mm, ϕ_2 is the 0.5 mm aperture and d is the distance between the two apertures, which is 170 mm. We measured the atomic beam size at the laser cooling region and at the probe region using fluorescence techniques. From the fluorescence image, the FWHM of the atomic beam at the cooling region is 0.52 mm, and at the probe region, the FWHM is 2.2 mm. Taking into account that the distance between the cooling region and the probe region is 620 mm, the full divergence of the atomic beam is θ=2.7 mrad. The discrepancy between the calculated collimation ratio κ and the measured full divergence θ of the atomic beam could be due to the clogging of the apertures such that the effective aperture size is smaller.

The atomic beam has a Maxwell-Boltzmann velocity distribution given by [33]:

$$f(v_z) = \frac{v_z^3}{2\tilde{v}^4}\, exp\,[\frac{-v_z^2}{2\tilde{v}^2}] \tag{2.15}$$

where v_z is the longitudinal velocity of the atomic beam, and $\tilde{v} = \sqrt{\frac{k_B T}{M}}$. The calculated most probable velocity for a typical operating temperature of $1200°C$ is 565 m/s. The longitudinal velocity distribution was measured with a time-of-flight method. The measured value of the most probable velocity is 530m/s. The Doppler width, $\Delta\nu_D$, of the atomic beam at the probe region for the $5P_{1/2} \rightarrow 6S_{1/2}$ transition is $\pm 5.5\, MHz$, which is obtained using the relation:

$$\Delta\nu_D = \pm\frac{k v_t}{2\pi} = \frac{v_{z,mp}\kappa}{\lambda} \tag{2.16}$$

where v_t is the most probable transverse velocity at the probe region, $v_{z,mp}$ is the most probable longitudinal velocity, λ is the excitation wavelength for the $5P_{1/2} \rightarrow 6S_{1/2}$ transition.

The atomic beam is made accessible to the laser beams through 4 AR-coated(at 410 nm, 451 nm) vacuum windows, mounted in a six-way cross(CF63). All optical components are mounted on an optical breadboard, outside the vacuum chamber. The detection region is 620 mm away from the cooling region. The vacuum chamber for the detection region consists of a smaller six-way cross (CF35) with 4 AR-coated viewports for detecting the atomic fluorescence.

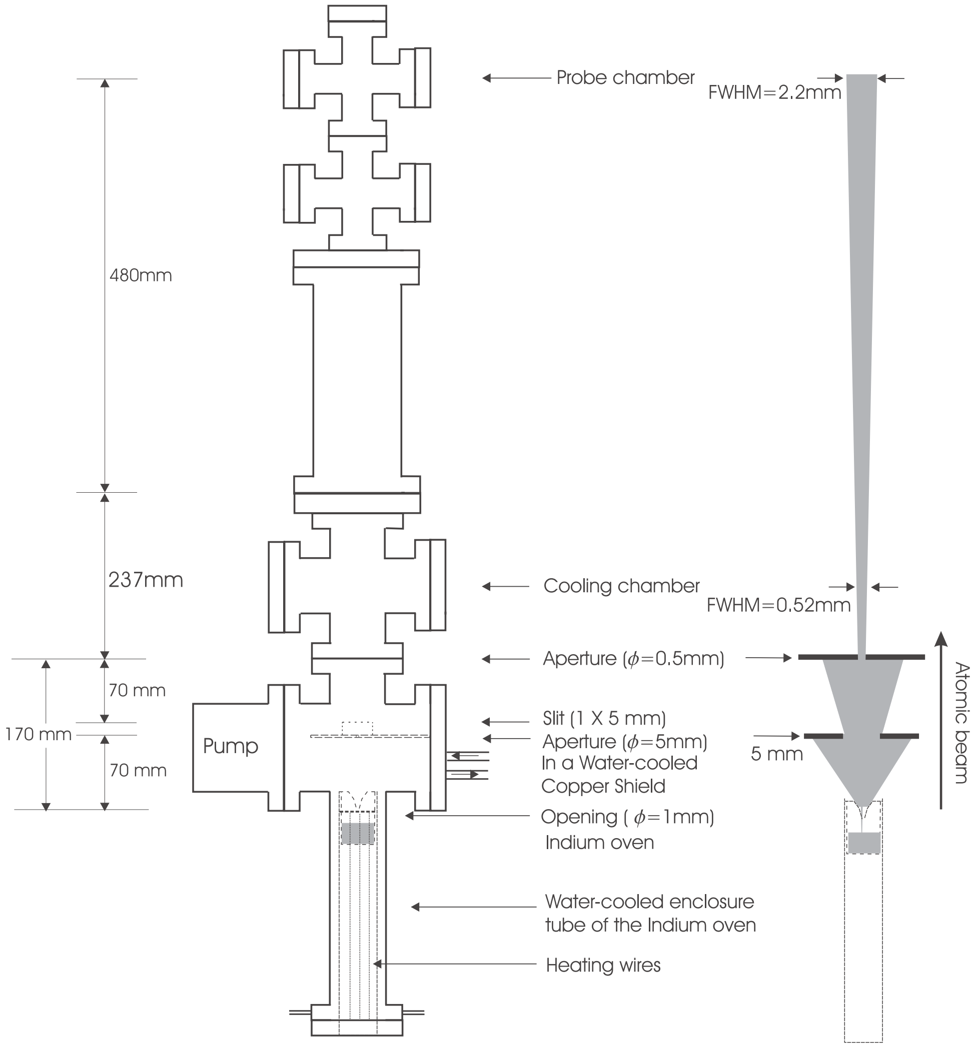

Figure 2.12: *The vacuum system with all dimensions specified.*

2.4 Detection system

The atomic beam profile at the probe region is obtained using fluorescence imaging. A CCD-camera is used to image the fluorescence emission of the atomic beam irradiated by either a 410 nm or a 451 nm light source at a resonant transition. The laser beam passes through a slit with a height of 1mm to remove the effect of optical pumping by the probe beam. The laser beam is locked to a resonant transition using current modulation and lock-in technique. Details of the locking scheme will be discussed in the next chapter on laser spectroscopy and stabilization. A typical fluorescence image of the 410 nm light source at the $F = 4 \rightarrow F' = 5$ resonant transition is shown in figure 2.13. From the geometry of the atomic beam, the transverse velocity v_t of the atoms at the probe region is deduced to be 73 cm/s. This is calculated from the atomic beam divergence θ and the longitudinal velocity v_{long} of the atoms:

$$v_t = v_{long} \cdot tan(\theta/2) \approx v_{long} \cdot \theta/2 = 73\, cm/s \tag{2.17}$$

where the atomic beam full divergence is $\theta = 2.7$ mrad.

The measured beam size is compared with a theoretical beam size using ballistic trajectory calculation, wherein the oven configuration and aperture geometry are used as input parameters. To obtain the theoretical plot, a simulation involving 40,000 atoms, in which the initial transverse velocity has a Gaussian distribution and the initial longitudinal velocity has a Maxwell-Boltzmann distribution with the most probable velocity v_{mp}= 530 m/s. In this simulation, the initial width of the transverse velocity distribution is $\Delta v_x = 0.5\, m/s$. The simulation result is shown in figure 2.14.

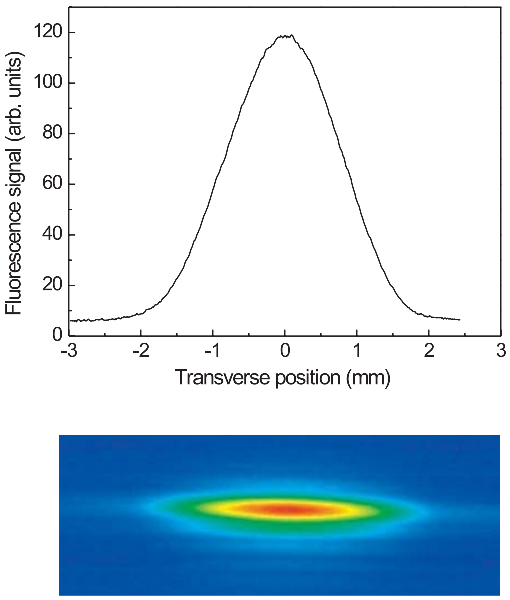

Figure 2.13: *Atomic beam integrated fluorescence profile.*

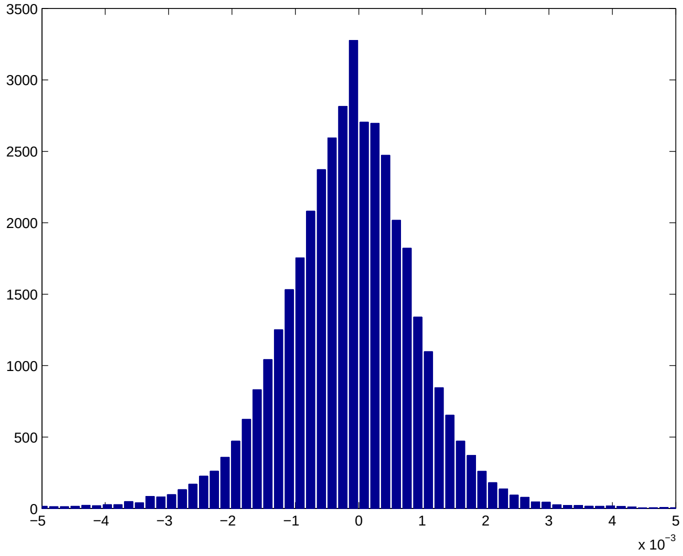

Figure 2.14: *Initial atomic distribution at the probe region. The y-axis corresponds to the number of atoms. The x-axis corresponds to the transverse position in units of meter.*

Chapter 3

Spectroscopy of Indium and Frequency-Stabilization

It is essential in laser cooling experiments that an atomic transition frequency is used as a reference for setting the laser frequency. Unlike alkali elements, such as cesium and rubidium, there is no vapor cell developed for indium. This is due to the fact that indium has a low vapor pressure at room temperature (P_v at $T = 27°C \approx 10^{-33}$ Torr). A commercial hollow cathode cell was first used for obtaining an absorption spectrum. In this hollow cathode cell, the absorption of the strongest 410 nm transition is only 20% and no sub-Doppler feature was observed. The Doppler width of indium vapor at a temperature of 630°C is 1.5 GHz. This linewidth is too broad to be used for laser stabilization, which requires us to have sub-Doppler features as frequency reference. A vapor cell, which can be heated up to temperatures on the order of 600-800°C, is therefore necessary for performing indium spectroscopy. An all-sapphire cell (ASC) was custom-built for our laboratory from the Armenian Academy of Science, as shown in figure 3.2. With an all-sapphire cell, the maximum absorption for the strongest transition of the 410nm line is 75%. With this cell, sub-Doppler features were observed with saturated absorption and polarization spectroscopy, which allows us to stabilize the laser frequency relative to the atomic transition. Results of our spectroscopy studies on an indium all-sapphire cell are elaborated in reference [37]. The spectroscopy schemes for frequency stabilization of the lasers in our cooling experiments are outlined in figure 3.1.

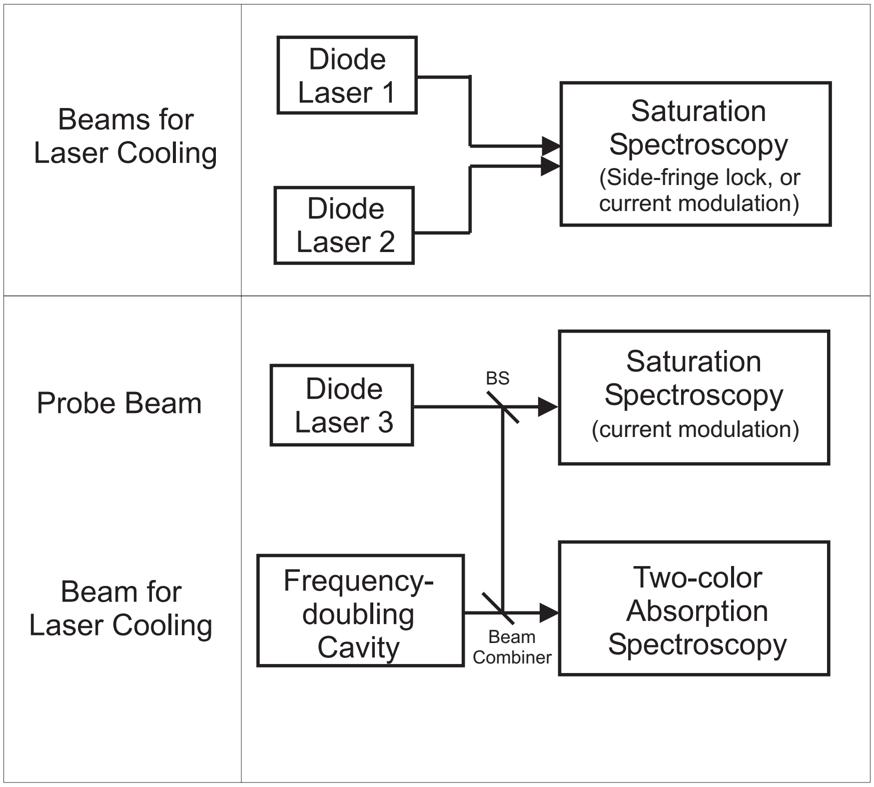

Figure 3.1: *Spectroscopy and frequency stabilization scheme for the light sources used in the laser cooling experiment.*

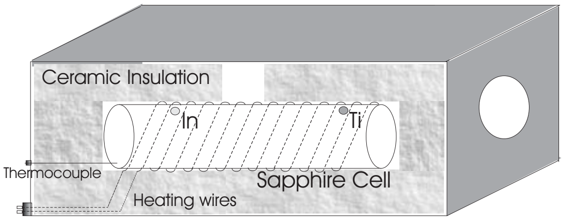

Figure 3.2: *Schematic view of the all-sapphire cell. A current of 5A passes through the NiCr heating wires to reach a temperature of 630° C. The temperature of the cell is monitored with a thermocouple during heating up and cooling down. When the sapphire cell is cooled down too fast, condensation of indium occurs at its end facets.*

3.1 Saturation Spectroscopy

Doppler-free saturation spectroscopy at the $5P_{1/2} \rightarrow 6S_{1/2}$ transition was performed using the experimental setup shown in figure 3.3. A strong pump beam is incident to the ASC and is propagating in opposite direction to a weak probe beam. The pump beam saturates the velocity group perpendicular to the pump beam. This saturation process is exhibited as a dip in the Doppler absorption profile, which is known as a Lamb-dip. In our experiment, the saturation parameter of the pump beam for the F=4→ F′=5 (410 nm line) is $0.5S_0$, while that for the probe beam is $0.2S_0$. The saturated absorption spectrum for the 410nm transition of indium when the laser is scanned across the four hyperfine transitions is shown in in figure 3.4. The Doppler profiles for the hyperfine transitions of the 410 nm line are well-resolved due to the large hyperfine splittings, on the order of 10 GHz. The large hyperfine splittings in this transition also leads to a single Lamb-dip for every Doppler-broadened absorption line, as can be seen in figure 3.4.

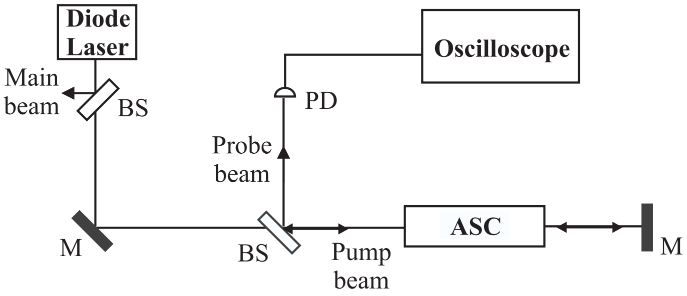

Figure 3.3: *Experimental set-up of saturated-absorption spectroscopy. A lock-in technique is employed to remove the Doppler-background from the spectrum. Only the Lamb-dip signal is used for laser stabilization.*

3.2 Laser Frequency Stabilization

Two locking schemes were employed for stabilizing the diode laser frequencies using the saturation spectroscopy signal.

3.2.1 Side-fringe locking

In the side-fringe locking scheme, the Doppler background is removed by amplitude modulation and lock-in technique. The pump beam is amplitude-modulated by a mechanical chopper at 1.8 kHz and the signal is used as

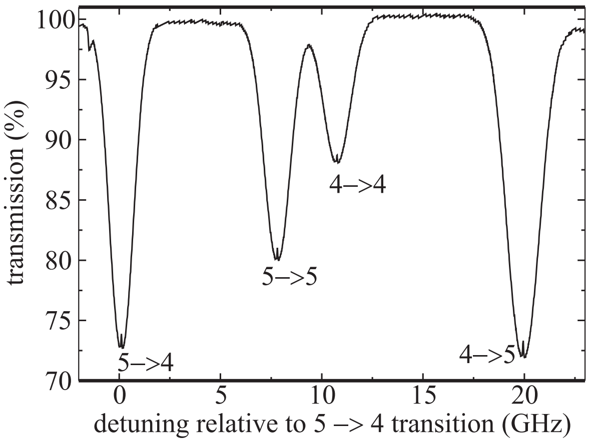

Figure 3.4: *Doppler profile and Lamb-dip feature of the 4 hyperfine transitions of the 410nm line.*

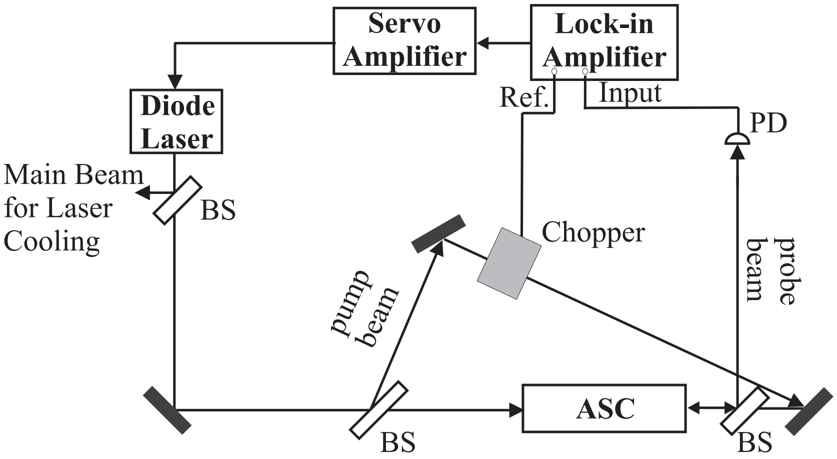

Figure 3.5: *Experimental set-up of saturated-absorption spectroscopy. A lock-in technique is employed to remove the Doppler-background from the spectrum. Only the Lamb-dip signal is used for laser stabilization.*

an input to a lock-in amplifier, as shown in figure 3.5. The demodulated signal is the pure Lamb-dip spectrum, which has a full-width half-maximum (FWHM) of 50 MHz, as shown in figure 3.6. The spectral resolution is narrow enough for frequency stabilization. The slope of the Lamb-dip fringe is used as an input to a servo-amplifier circuit. The servo-amplifier actively controls the input voltage of the piezo in the laser cavity, thus, controlling the laser frequency. The zero-level crossing along the slope of the Lamb-dip signal corresponds to the frequency on which the laser is stabilized. By changing the input offset of the servo-amplifier, the laser frequency can be swept across the frequency range of the Lamb-dip, which is 50 MHz in the case of indium. This method is applied to the cooling lasers, whose frequencies are detuned from resonance by several MHz. This method can not be employed for frequency-stabilization at the resonance frequency (Δ=0) because at resonance, there is no corresponding slope of the Lamb-dip signal. Thus, for applications which require stabilizing the laser onto resonance, the current modulation method is employed.

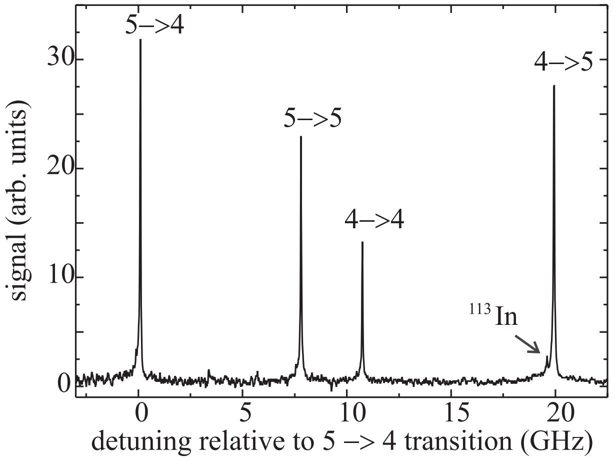

Figure 3.6: *Lamb-dip spectrum of the 4 hyperfine transitions of the 410nm line, after the Doppler background is removed by demodulating the photodiode signal with a lock-in amplifier.*

3.2.2 Current Modulation

Another stabilization scheme involves locking the laser frequency on the zero-crossing of a dispersive-shaped signal. The experimental scheme for this frequency stabilization method is shown in figure 3.7. The first-derivative of the saturated-absorption spectrum has a dispersive profile, as shown in figure 3.8. When the laser frequency is modulated, the demodulated spectroscopy signal from the lock-in amplifier is simply the first-derivative of the absorption spectrum. Modulation of the laser frequency can be achieved by modulating the input current to the laser. The typical current modulation frequency in our experiment is 14 kHz and the laser current source has a modulation amplitude of 2 mV. Since current modulation locking allows us to set the laser frequency to zero detuning, this technique is applied to diode lasers used as a probe beam and as 'repumpers' in our laser cooling experiment.

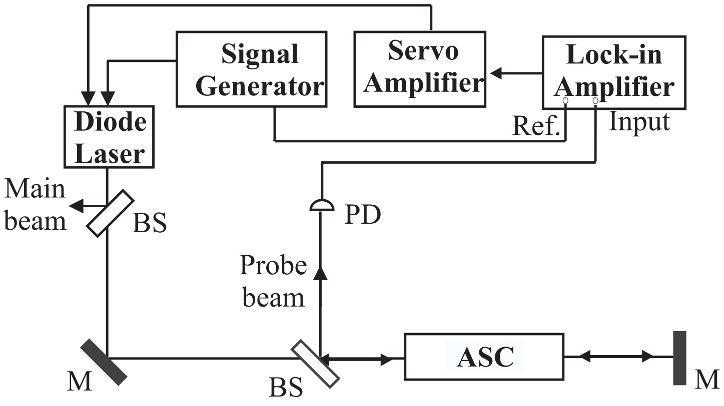

Figure 3.7: *Experimental set-up for frequency stabilization using current-modulation technique.*

During the laser cooling experiment, the detuning of the 410 nm cooling laser is determined from the beat frequency of the reference laser and the detuned, cooling laser. The reference laser is normally locked in resonance with the current modulation scheme. On the other hand, the detuned laser is locked with the side-fringe technique. The beat signal is obtained when the two lasers are overlapped and is incident to a fast photodiode, whose signal is monitored with a spectrum analyzer. From the frequency read-out of the spectrum analyzer, the amount of detuning is determined.

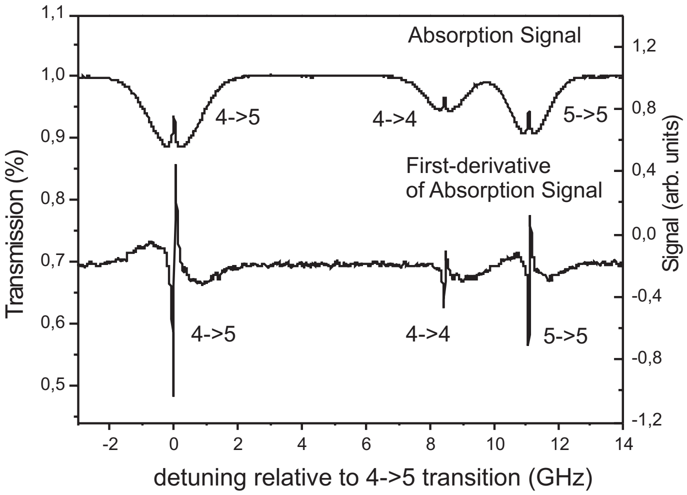

Figure 3.8: *First-derivative of the absorption signal of the 410 nm-indium transitions. The dispersive-shaped signal is used for frequency stabilization.*

3.2.3 Allan Variance

The frequency stability can be characterized in the time-domain by the IEEE standard method, known as the 'Allan variance'. The Allan variance can be obtained from the average value of the discrete frequency fluctuations $\bar{y}_i$ and is given by [34]:

$$\sigma_y^2(\tau) = \frac{1}{(N-1)} \sum_{i=1}^{N-1} \frac{(\bar{y}_{i+1}(t+\tau) - \bar{y}_i(t))^2}{2} \tag{3.1}$$

The Allan variance does not depend on the number of samples for obtaining the power law spectral density, in contrast to the classical variance. The type of noise can be characterized by a parameter α from the dependence of the Allan variance on the time interval τ, given by:

$$\sigma_y^2(\tau) \propto \tau^{-\alpha-1} \tag{3.2}$$

Noise type	α
White noise due to phase	2
Flicker noise due to phase	1
White noise due to frequency	0
Flicker due to frequency	-1
Random walk (frequency)	-2

The square-root of the Allan variances $\sigma_y(\tau)$ for the two locking techniques, side-fringe locking and current-modulation scheme, are plotted in figure 3.9. The frequency stability of the laser locked at the Lamb-dip fringe is 260 kHz for an integration time of 1 sec while that locked using current modulation technique is 340 kHz for the same integration time. For the laser locked to the Lamb-dip fringe, white noise due to frequency ($\sigma_y(\tau) \propto \tau^{-1/2}$) is a dominant noise type as seen in the slope of its Allan variance. On the other hand, for the laser locked to the dispersive-shaped signal with current modulation, flicker noise due to phase ($\sigma_y(\tau) \propto \tau^{-1}$) is a dominant noise type as can be inferred from the slope of its Allan variance.

3.3 Two-color Absorption Spectroscopy

Absorption spectroscopy was performed for indium at the 451 nm ($5P_{3/2} \rightarrow 6S_{1/2}$) transition. However, due to the low thermal population of the $5P_{3/2}$ ground state at 630°C, the absorption is relatively weak. The maximum absorption is only 6%. In our experiment, optical pumping from $5P_{1/2}$ to $5P_{3/2}$

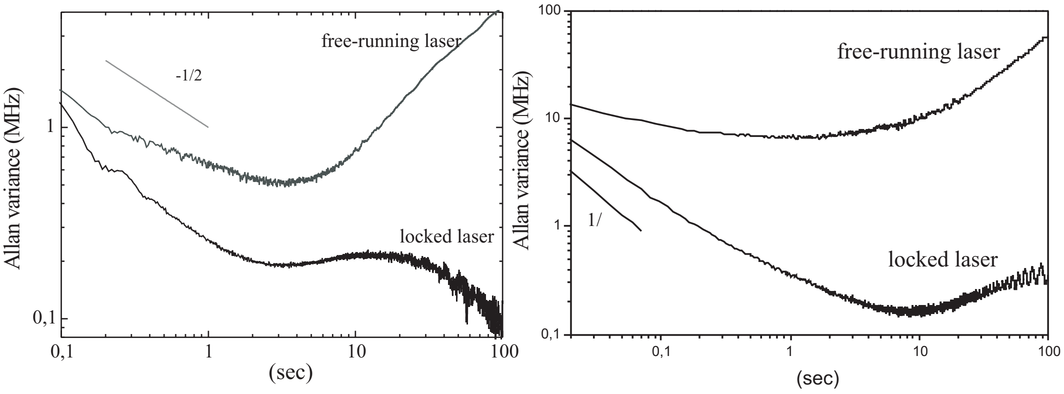

Figure 3.9: *The square-root of the Allan variance of the error signal of the free-running laser and for the same laser locked on resonance of the F=4 → F=5 transition using (left) Lamb-dip side-fringe locking and (right) using current modulation scheme.*

ground state using the 410 nm light source was done to obtain a larger absorption signal. The experimental setup is shown in figure 3.10. The 410 nm light source is locked in resonance at the $|\mathrm{F{=}4}\rangle \rightarrow |\mathrm{F{=}5}\rangle$ transition and amplitude-modulated to remove the Doppler background. The transmission signal of the 451 nm laser is detected with a photodiode and is demodulated with a lock-in amplifier. With this scheme, the absorption is increased to more than 10%. Since we are only interested in the absorption spectrum from the 451 nm light, an interference filter is placed before the photodiode to prevent the 410 nm light from being detected by the photodiode. The 451 nm laser scans across two sets of hyperfine transitions, (set 1) $|F = 4, 5, 6\rangle \rightarrow |F = 5\rangle$ and (set 2) $|F = 3, 4, 5\rangle \rightarrow |F = 4\rangle$. The background-free transmission signal is recorded in figures 3.11 for set 1 transitions and figure 3.12 for set 2.

The transmission signal for each transition is unexpectedly broad with a FWHM between 300-500 MHz. Power broadening for this case is negligible. We can phenomenologically approximate the observed profiles of the resonance lines of the $F'' = 4, 5 \rightarrow F = 4$ with a combination of Lorentzian and Gaussian profiles with a FWHM of 170 MHz and 600 MHz, respectively. Both linewidths are broad compared to the expected linewidth of 30-50 MHz for a small velocity class probed in linear absorption spectroscopy. This broad linewidth is due to velocity-changing collisions [35, 36]. A numerical simulation was carried out wherein an initial velocity group with v=0 is

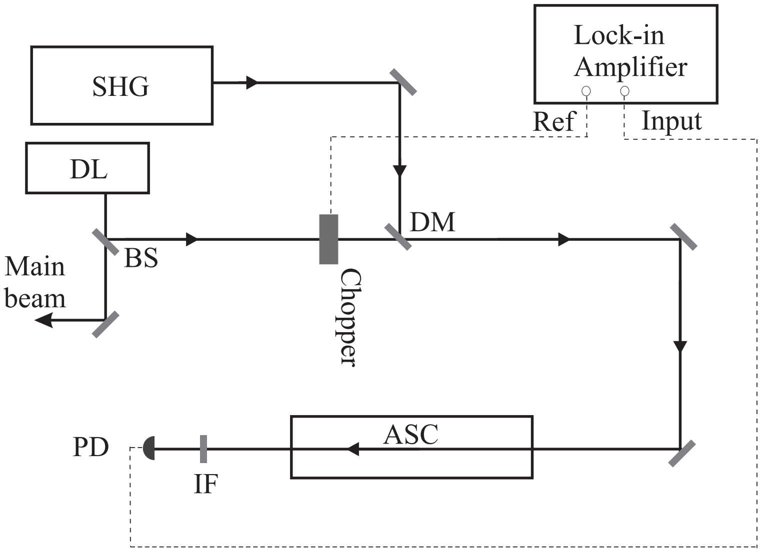

Figure 3.10: *Experimental set-up for two-color absorption spectroscopy in an all-sapphire cell. A dichroic mirror (DM) is used to combine the 451 nm light with the 410 nm laser beam. An interference filter (IF) blocks the 410 nm laser so it will not be detected by the photodiode.*

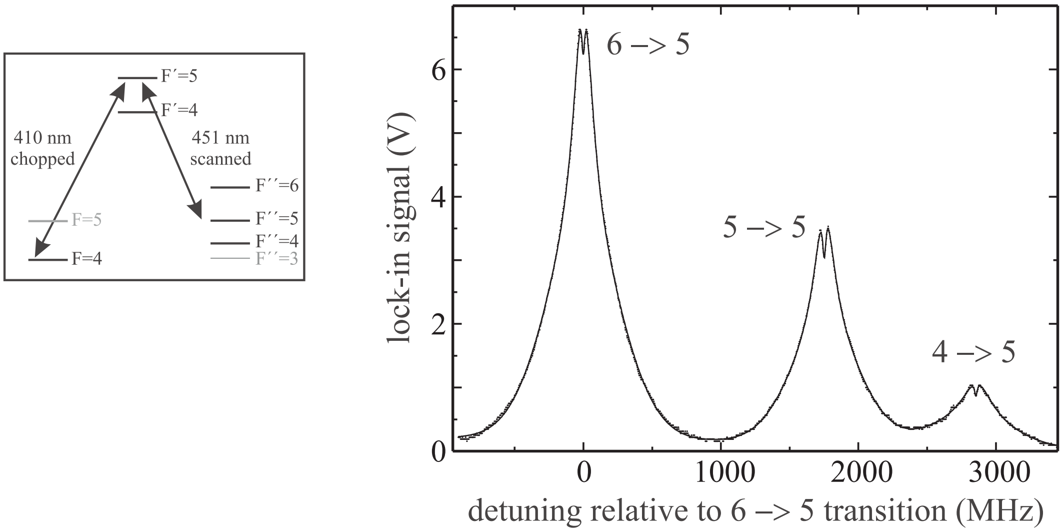

Figure 3.11: *Lock-in signal for the transmission of 451 nm light in an all-sapphire cell, scanned at F''=6,5,5→ F'=5. The amplitude-modulated 410 nm light is set in resonance at F=4→ F'=5 transition.*

redistributed by a single collision with thermal atoms with an rms velocity v_σ in a hard sphere model [37]. The result of this simulation is a velocity distribution with a narrow Lorentzian and a wider Gaussian profile with a FWHM which is 41% larger than the initial thermal distribution.

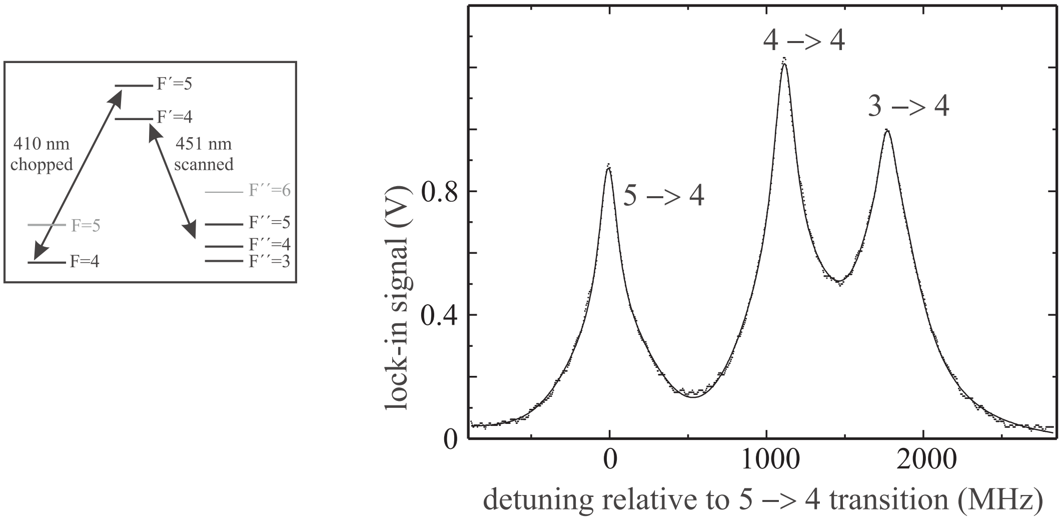

Figure 3.12: *Lock-in signal for the transmission of 451 nm light in an all-sapphire cell, scanned at* $F''=5,4,3\rightarrow F'=4$. *The amplitude-modulated 410 nm light is set in resonance at* $F=4\rightarrow F'=5$ *transition.*

There is a narrow dip at the center of each transition peak when the 410 nm and 451 nm lasers excite the same upper hyperfine level, as shown in figure 3.11. Increased transmission of the 451 nm laser is manifested as a dip in the absorption spectrum. This can be explained as a coherent two-photon process, as shown by its exclusive presence when the two lasers are coupled to the same upper level.

The presence of the $F = 3 \rightarrow F' = 4$ transition line, in figure 3.12, is unexpected since the F=3 state can not be populated by radiative decay from the $|6S_{1/2}, F = 5\rangle$ state. The F=3 state is populated by atom-atom collisions. The fit of the $F = 3 \rightarrow F' = 4$ gives a narrower Gaussian curve of 460 MHz compared to the $F = 4, 5 \rightarrow F' = 4$ transition and a Lorentzian of 95 MHz, which supports this argument.

3.4 Fluorescence Spectroscopy with an Atomic Beam

In fluorescence spectroscopy, the absorption of laser photons of an atomic sample is observed by monitoring the laser-induced fluorescence. When the

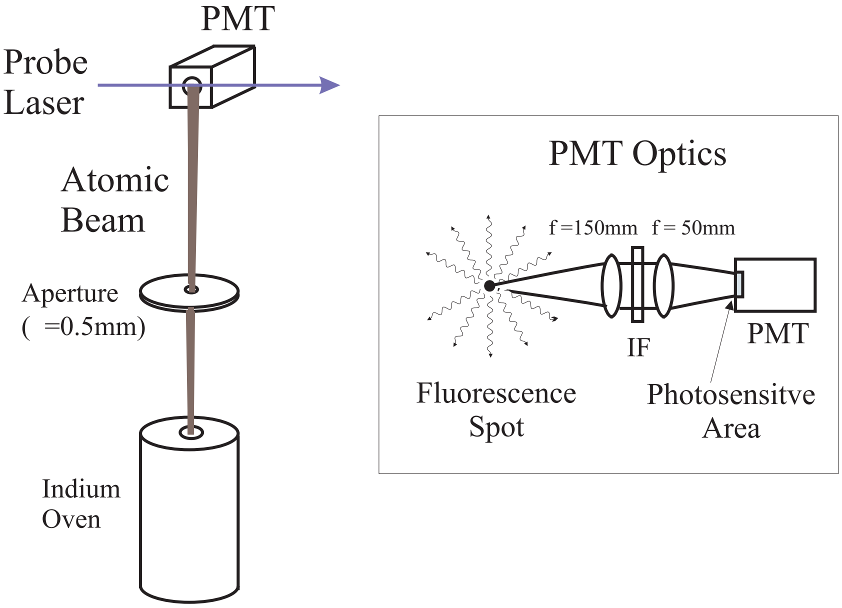

Figure 3.13: *(Left) Fluorescence spectroscopy set-up for indium. A photomultiplier tube (PMT) is used to detect the laser-induced fluorescence. (Right) A set of lenses is used to increase the fluorescence collection efficiency. The lens configuration is applicable to our particular atomic beam set-up. An interference filter IF is used to remove any fluorescence emission of another wavelength from being detected.*

laser wavelength is scanned across the atomic absorption lines, the fluorescence intensity as a function of laser wavelength is recorded, which is simply the excitation spectrum. The number of fluorescence photons being detected per second is given by [38]:

$$n_{fluo} = n_a \eta_k \eta_{ph} \varsigma \tag{3.3}$$

where n_a is the number of absorbed photons per second, η_k is the quantum efficiency of the excited state defined as the ratio of the spontaneous transition rate A_k to the total deactivation rate, $\eta_k = A_k/(A_k + R_k)$ where R_k is the rate of collision-induced transitions or other transitions not related to spontaneous emission, η_{ph} is the quantum efficiency of the detector, and ς is the fraction of fluorescence photons collected by the detection optics. The relative peak heights of the excitation spectrum reflect the relative decay probabilities of the atomic transitions, only if (1) the atoms radiate before they undergo collisions with other atoms or with the background gas, and

(2) the quantum efficiency of the detector is constant for all excited states, which is satisfied by existing photomultiplier tubes (PMT). Even if the above conditions are not fulfilled, fluorescence spectroscopy is still a good frequency marker.

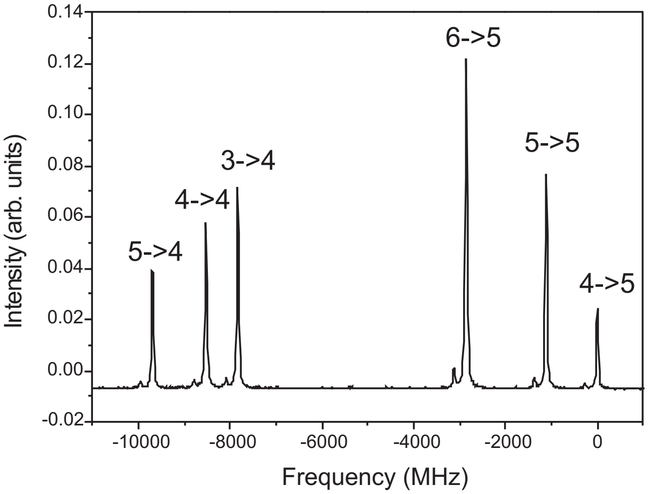

Figure 3.14: *Fluorescence spectrum of the indium atomic beam when the 451 nm laser frequency is scanned across the six hyperfine transitions.*

The fluorescence spectroscopy set-up with an indium atomic beam is shown in figure 3.13. The applications of fluorescence spectroscopy for indium laser cooling are as follows:

1. Frequency reference for 451 nm laser

On top of the two-color absorption spectroscopy, the fluorescence spectrum of the 451 nm laser is also used as a frequency marker. A typical fluorescence spectrum of the atomic beam excited by a 451 nm laser is shown in figure 3.14. The fluorescence signal provides a narrow linewidth of 60 MHz, when the laser beam is perfectly orthogonal to the atomic beam. Unlike the two-color spectroscopy for 451nm-indium transitions, the absorption line of the fluorescence spectrum is stable in frequency because it is independent of the overlap of the pump and probe beams (410 nm and 451 nm lasers) and any frequency instability of the 410 nm pump laser. Fluorescence spectroscopy can not be used, however, for in-situ frequency measurement because it uses the same atomic beam as that for laser cooling experiments. In practice, the frequency calibration with this scheme is done before and after a measurement interval during the laser cooling experiment.

2. Optimizing the frequency sources for the EOM and AOM

In chapter 2, it was discussed how the frequencies of the EOM microwave generator and the AOM RF source are set using the fluorescence signal of the atomic beam.

3. Alignment of the laser beams relative to the atomic beam

To ensure that the laser beams are orthogonal to the atomic beam, the fluorescence spectrum of the atomic beam is compared with the saturated-absorption spectrum in the All-Sapphire Cell (ASC). This can be applied for indium because the Lamb-dips are well-resolved. The Lamb-dip is a sufficient measure of laser-beam-to-atomic-beam orthogonality because it occurs only when the laser beam selects an atomic velocity group perpendicular to the propagation direction. Thus, when the absorption lines in the fluorescence spectrum is at the same frequency location as the Lamb-dip in the ASC, then the atomic beam is perpendicular to the laser beam.

Chapter 4

Laser Cooling of an Indium Atomic Beam

Laser cooling of indium can be caused by several mechanisms because of its rich multilevel structure. Thus, several experimental schemes were investigated. To determine the effect of the cooling lasers on the transverse velocity distribution of the atomic beam, the fluorescence signal at the probe region is imaged by a CCD camera. The width of the transverse velocity distribution can be calculated from the FWHM (full-width half-maximum) of the Gaussian fit of the fluorescence signal. The number of atoms in the state being probed is proportional to the area under the curve of the fluorescence signal.

4.1 Laser Cooling with 410 nm Lasers

4.1.1 Five-Frequency Laser Cooling

One-dimensional Doppler cooling is expected when the cooling lasers are red-detuned relative to the atomic resonance and when the interaction time t_{int} of the lasers with the atomic beam is greater than the damping time τ_{damp}. The damping time τ_{damp}, during which the atomic velocities are decreased to a minimum attainable velocity, is τ_{damp}= m/β = 15.4 μs, where m is the atomic mass. For Doppler cooling, the damping coefficient β is given by equation (1.25). It should be noted that this value of the damping time is based on a two-level atom. For a cooling mechanism which is based on a multi-level atom, in particular polarization-gradient cooling in a lin$\perp$lin configuration, the damping time is shorter due to optical pumping effects [39]. The interaction time in this five-frequency cooling experiment is $\sim 8\,\mu$s.

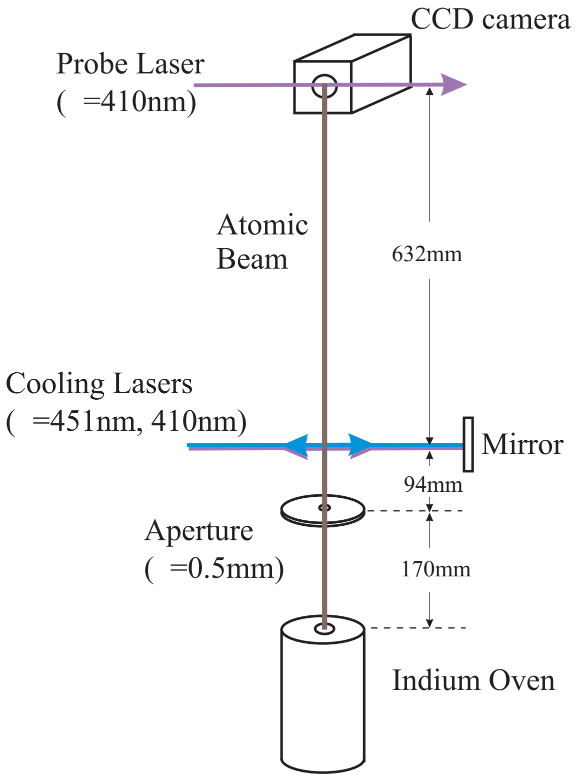

Figure 4.1: *Experimental scheme to achieve five-frequency transverse laser cooling of an indium atomic beam.*

The experimental configuration implemented to investigate laser cooling is shown in figure 4.1. The 410 nm and 451 nm lasers have the same propagation direction and are overlapped at the interaction region. A dichroic mirror is used to combine the 410 nm and 451 nm lasers. To ensure that the laser beams are well-overlapped at the cooling region, a CCD camera is used to detect the position of the fluorescence signal of the atomic beam with all laser frequencies tuned to the atomic resonance. The overlap of the laser beams at the dichroic mirror is adjusted until only one fluorescence spot due to all the lasers is detected. All lasers are linearly-polarized and in a standing-wave configuration. The polarizations of the two 410 nm lasers are oriented perpendicular to each other, and the polarizations of the 451 nm lasers from the EOM are oriented perpendicular to that from the AOM.

In the initial laser cooling experiment, the laser frequencies are set such that both 410nm lasers are red-detuned by $\Delta = -1.5\Gamma$ ($\Gamma = 2\pi{\cdot}25$MHz) and the 451nm laser is on resonance. The intensities of the 410nm lasers are I=310mW/cm^2 at the F=4 → F$'$=5 transition, I=280mW/cm^2 at the F=5 → F$'$=5 transition. For the 451nm laser, the intensity for each transition is I=50mW/cm^2. The probe laser frequency is resonant to the $F = 4 \rightarrow F' = 5$

(410nm) transition. Contrary to what is expected for Doppler cooling, a dip in the middle of the fluorescence signal is observed, as shown in figure 4.2. This suggests that the atoms are pushed away from the center of the atomic beam, and is referred to as a 'heating' signal. A narrowing of the transverse velocity distribution, or a 'cooling' signal, is what we intend to achieve. To observe a cooling signal, the detunings of the 410 nm lasers were changed from red to blue-detuning. When the 410 nm laser frequencies were blue-detuned by $\Delta = +2.5\Gamma$, and the 451 nm laser frequency was kept on resonance, a narrow peak at the center of the atomic beam fluorescence was observed, as shown in figure 4.3. With the cooling lasers, the width of the narrow fluorescence peak is 0.6 mm, 20% larger than the last defining aperture (ϕ=0.5 mm) of our atomic beam set-up, and 15% larger than the width of the atomic beam (0.52 mm) at the cooling region. This translates into a transverse velocity distribution with a FWHM of $v_T = 12$ cm/s for the cold atoms. The transverse velocity distribution of the uncooled atoms has a width of $v_T = 73$ cm/s. The broad background suggests that not all atomic velocity groups experience a damping force.
Furthermore, when the 451 nm laser is switched off, the cooling effect was still observed, as shown in figure 4.4. The 451nm laser in this configuration does not affect the transverse velocity distribution of the atoms, but it only optically-pumps the atoms from the $5P_{3/2}$ to the $5P_{1/2}$ state.

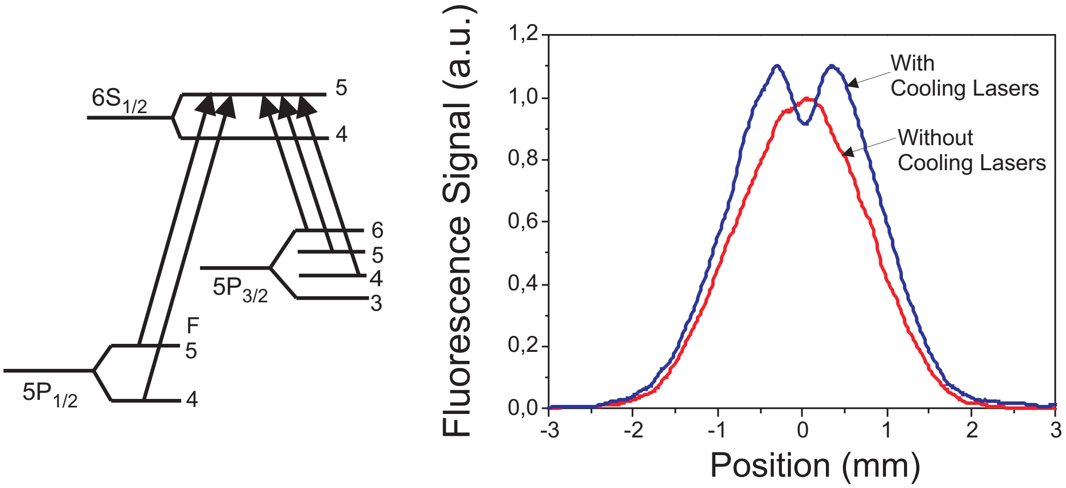

Figure 4.2: *Fluorescence signal of the atomic beam with red-detuned cooling lasers, for the experimental scheme in figure 4.1.*

Simulation

The damping force for a five-frequency optical excitation was calculated by

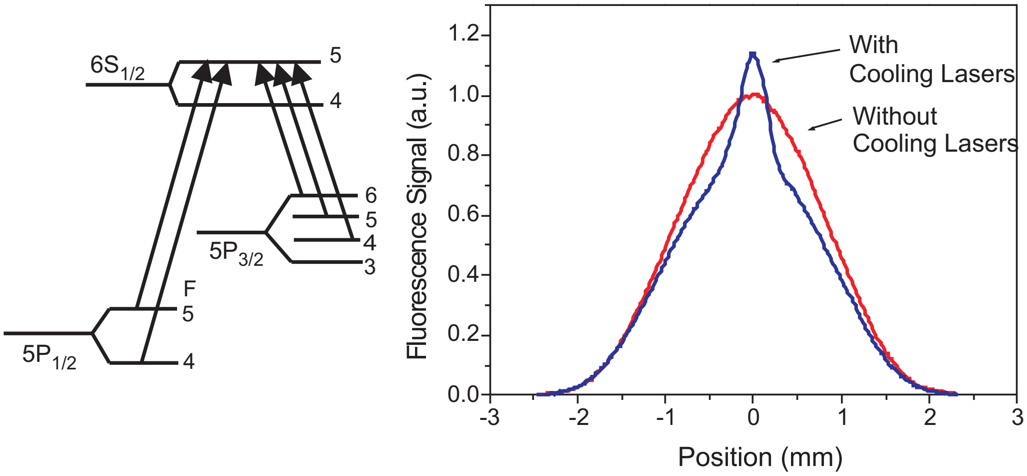

Figure 4.3: *Fluorescence signal of the atomic beam with blue-detuned cooling lasers, for the experimental scheme in figure 4.1.*

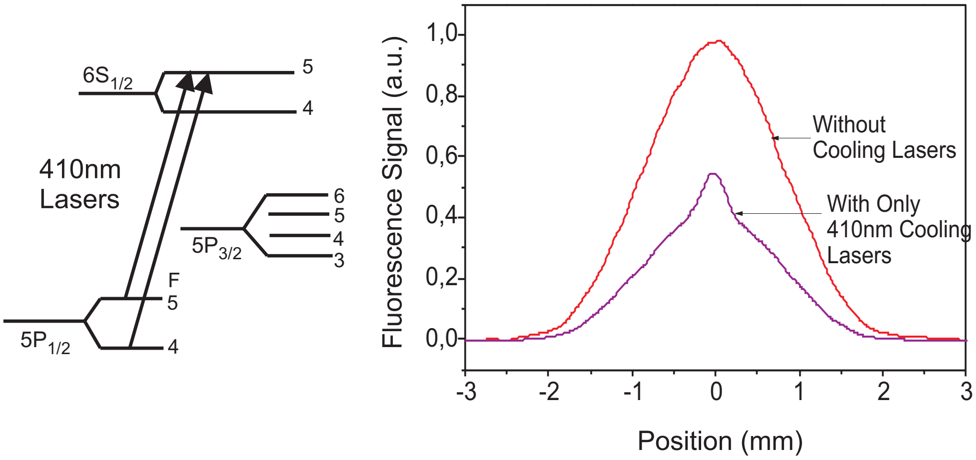

Figure 4.4: *Fluorescence signal of the atomic beam with blue-detuned cooling lasers with only 410 nm in the cooling region.*

using the semi-classical approach, in which the interaction Hamiltonian is given by:

$$H(x,t) = \hbar\Delta_i|g\rangle\langle g|e^{-i\omega t} + \frac{\hbar\Omega_i}{2}cos(k_i x)(|e\rangle\langle g| + |g\rangle\langle e|)e^{-i\omega t} + c.c. \qquad (4.1)$$

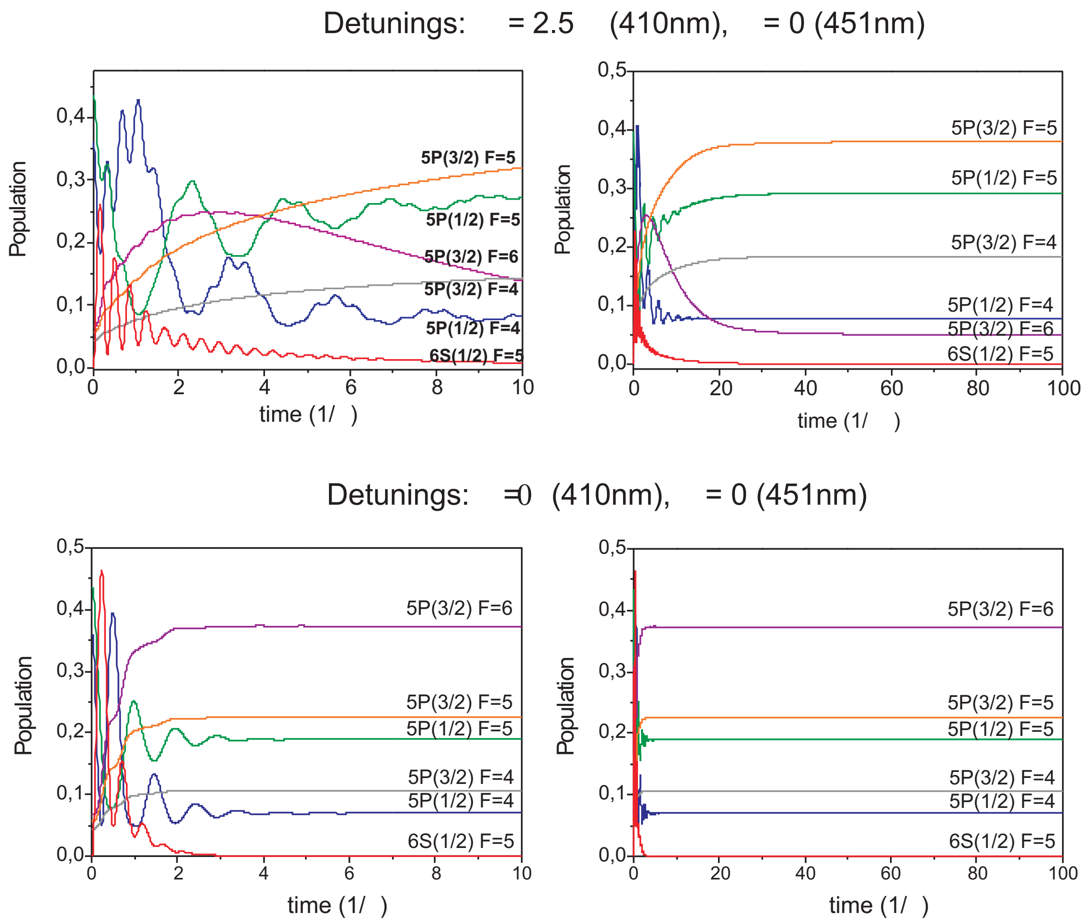

Figure 4.5: *Time evolution of the population when all five-hyperfine transitions are coupled, for time t=0→t=10/Γ (left) and for longer time t→t=100/Γ (right). The Rabi frequencies are as follows: 410nm transitions* $\Omega_{4\to5} = 1.6\Gamma$, $\Omega_{5\to5} = 0.6\Gamma$, *and for the 451nm transitions:* $\Omega_{6\to5} = 0.2\Gamma$, $\Omega_{5\to5} = 0.07\Gamma$, $\Omega_{4\to5} = 0.02\Gamma$. *The 410nm light is blue-detuned by 2.5Γ while the 451nm is set on resonance. The x-axis is in units of 1/Γ where Γ=2π25MHz.*

where k_i is the wavenumber of the light field, Δ_i is the detuning for the particular transition, and Ω_i is the Rabi frequency. The matrix form of the interaction Hamiltonian for the five-frequency excitation is given in equation (1.18). In this case, only standing wave configurations with linearly-polarized fields were considered. The factor $\cos(k_i x)$ is due to the interaction of the atom with a standing wave field. It should be noted that $x = v_T t$, where

v_T is the transverse velocity of the atom. Furthermore, since there are only linearly-polarized fields in a standing wave configuration, coupling between the Zeeman sublevels is not considered in this case.
The average force is calculated from the product of the density matrix and the gradient of the interaction Hamiltonian, as expressed in equation (1.21). The average force is:

$$\begin{aligned} F \;=\; & \frac{\hbar}{2}\,[\,k_1\,\Omega_1\,\cos(k_1\,x)\,\tilde{\rho}\,(g_4, e_{5\,(410)}) + \,k_1\,\Omega_2\,\cos(k_1\,x+\varphi_2)\,\tilde{\rho}\,(g_5, e_{5\,(410)}) \\ & + k_2\,\Omega_3\,\cos(k_2\,x+\varphi_3)\,\tilde{\rho}\,(g_6, e_{5\,(451)}) + \,k_2\,\Omega_4\,\cos(k_2\,x+\varphi_4)\,\tilde{\rho}\,(g_5, e_{5\,(451)}) \\ & + k_2\,\Omega_5\,\cos(k_2\,x+\varphi_5)\,\tilde{\rho}\;\;(g_4, e_{5\,(451)})\,)\,] + c.c. \end{aligned}$$

where k_1 and k_2 are the wavenumbers for the 410nm and 451nm light fields, respectively, φ_i are the phase differences between each light field, and $\tilde{\rho}(g_n, e_m)$ is given by

$$\tilde{\rho}(g_n, e_m) = \langle g_n|\rho|e_m\rangle\, e^{-i\omega_L t} \tag{4.2}$$

where ρ is the steady-state density operator, the subscripts n and m denote the hyperfine level, the subscripts 410 and 451 denote the $J \rightarrow J'$ transition, and ω_L is the laser frequency. The set of differential equations to solve the density matrix elements $\tilde{\rho}(g_n, e_m)$ is given in appendix B.
In the simulation, the laser intensities and detunings are set similar to the experimental conditions. The initial population is the thermal distribution at T=1200°C, such that, at the 5P$_{1/2}$ ground state, the population is 80% of the total population (44% for the F=5 hyperfine state and 36% for the F=4 state) and at 5P$_{3/2}$ state, the population is 20% (6.5% for the F=6 state, 5.5% for F=5, 4.5% for F=4, 3.5% for F=3).
The evolution of the population for a given set of Rabi frequencies and detunings, when all five hyperfine transitions are coupled, is shown in figure 4.5. When there is a relative detuning between the $5P_{1/2} \rightarrow 6S_{1/2}$ and the $5P_{3/2} \rightarrow 6S_{1/2}$ transitions, two prominent features in the evolution of the population can be seen. (1) There is an inversion of the population of the $|5P_{3/2}, F=6\rangle$ state after a time t = $3/\Gamma$. (2) The steady-state population of the $|5P_{3/2}, F=5\rangle$ state is higher compared to the $|5P_{3/2}, F=6\rangle$ state. These features are not present for zero detuning. On the contrary, with zero detuning, the steady-state population of the $|5P_{3/2}, F=5\rangle$ state is lower than that of the $|5P_{3/2}, F=6\rangle$. Furthermore, the population of the $|5P_{3/2}, F=6\rangle$ state increases monotonically without inversion before reaching a steady-state condition. Here, we gain some insight into how the atomic population evolves in a Lambda-system. The population evolution was also calculated for the opposite sign of the detuning, for $\Delta = -2.5\Gamma$, and the result is the same for both positive and negative detunings.

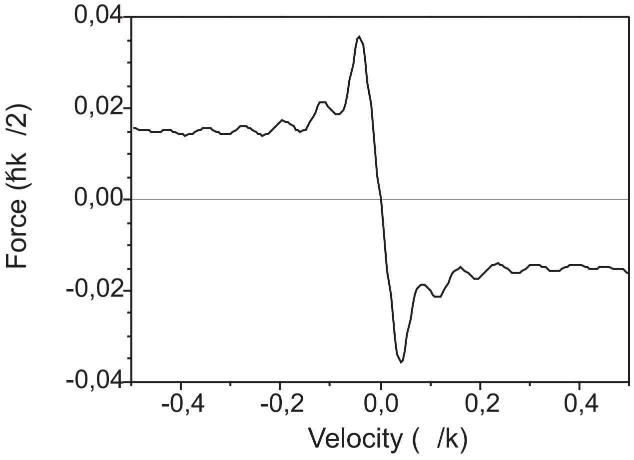

Figure 4.6: *Force as a function of velocity for the six-level indium atomic structure, in the case of blue-detuned 410nm lasers. The detunings for the 410 nm lasers are* $\Delta_{4\to5} = 2.5\,\Gamma, \Delta_{5\to5} = 2.5\,\Gamma$, *and the 451nm laser is in resonance,* Δ*=0. The Rabi frequencies are: (410nm transitions)* $\Omega_{4\to5} = 1.6\Gamma$, $\Omega_{5\to5} = 0.6\Gamma$, *(451 nm transitions):* $\Omega_{6\to5} = 0.2\Gamma$, $\Omega_{5\to5} = 0.07\Gamma$, $\Omega_{4\to5} = 0.02\Gamma$. *The spontaneous emission rates for the 410 nm lasers are* $\Gamma_{4\to5} = 0.213\Gamma$, $\Gamma_{5\to5} = 0.142\Gamma$*; for the 451 nm laser:* $\Gamma_{6\to5} = 0.381\Gamma$, $\Gamma_{5\to5} = 0.194\Gamma$, $\Gamma_{4\to5} = 0.070\Gamma$.

After obtaining the atomic population and coherences, the spatial average of the force can be calculated. A plot of the force as a function of velocity is shown in figure 4.6. To include the effect of the phase difference between each laser, the force is averaged over different phase shifts. It can be seen that there is a damping force for blue-detuned 410 nm cooling lasers and resonant 451 nm laser. The force vs. velocity curve has a steep slope for $-0.03\Gamma/\mathrm{k} \leq \mathrm{v} \leq 0.03\Gamma/\mathrm{k}$, corresponding to a velocity capture range of 30cm/s. The damping coefficient is dF/dv=$-0.5\hbar k^2$ at v=0. This amount of damping force could produce a narrow velocity distribution within the velocity capture range. From this calculation, it is difficult to estimate the amount of heating due to the Doppler force. In the plot of force vs. velocity, the structure at high velocities could be due to multiphoton resonances or Dopplerons [41, 42].

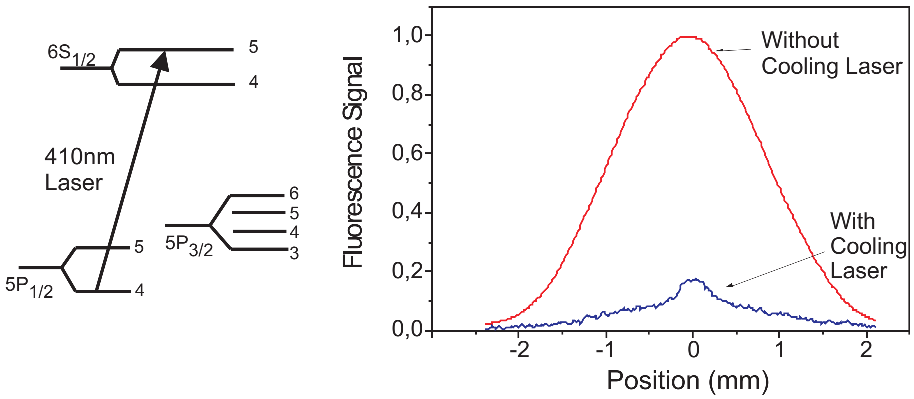

Figure 4.7: *Fluorescence signal of the atomic beam with blue-detuned cooling lasers for* $\Delta = 1.1\Gamma_{410}$*, S=2.8. The scale of the fluorescence signal is normalized relative to that without cooling lasers. The fluorescence signal with cooling laser is rescaled by 10x for better visibility.*

4.1.2 Single-Frequency Laser Cooling at 410 nm Transition

The simplest configuration to investigate is when only one 410 nm hyperfine transition is excited. The cooling laser frequency is set at $|5P_{1/2}, F = 4\rangle \rightarrow |6S_{1/2}, F = 5\rangle$ transition. The interaction time is 5.7 μs. The probe laser is set in resonance at the same hyperfine transition as the cooling laser. Since the cooling laser and the probe laser excites the same transition, optical pumping effects are observed. The amplitude of the fluorescence signal decreases dramatically due to optical pumping. Only $\sim 1.5\%$ of the atoms remain in the $|5P_{1/2}, \mathrm{F{=}4}\rangle$ ground state when the cooling laser is detuned by $\Delta = 1.1\Gamma_{410}$, as shown in figure 4.7. Such depopulation of the $|5P_{1/2}, \mathrm{F{=}4}\rangle$ ground state is estimated to occur after a time $t = 4/\Gamma$ or 4 pumping cycles. This estimate of the number of pumping cycles was obtained from the population evolution, as shown in figure 4.8, with only one hyperfine transition coupled to the light field. The fluorescence signal observed with a blue-detuned, single-frequency cooling laser has a narrow central peak, and a broad Doppler background, as shown in figure 4.7.

For the single-frequency cooling, the effect of the cooling laser intensity, detuning and polarization were investigated.

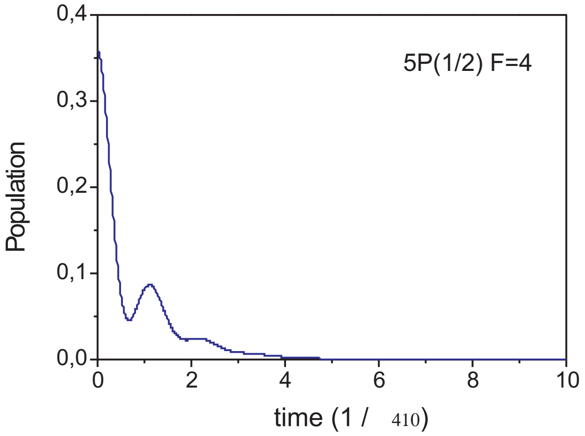

Figure 4.8: *Time evolution of the population when only one hyperfine transition is excited by the 410 nm laser. The Rabi frequency is* $\Omega = 0.32\Gamma_{410}$ *and the detuning is* $\Delta = 1.1\Gamma_{410}$

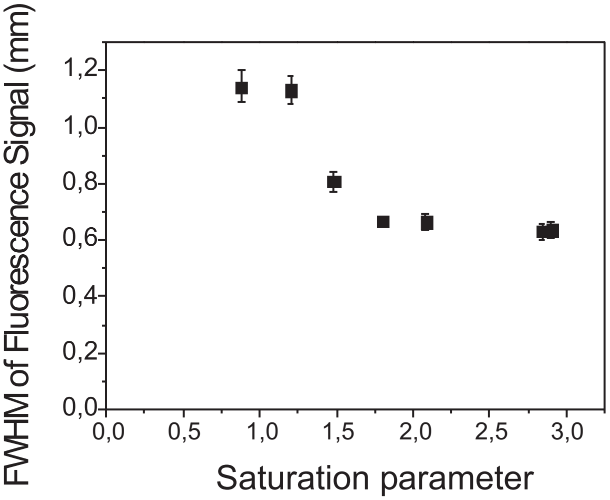

Figure 4.9: *Intensity-dependence of the width (FWHM) of the fluorescence signal of the cooled atoms (narrow peak) in the presence of a single-frequency cooling laser. The intensity is written in terms of the saturation parameter for the 410nm* $|F=4\rangle \rightarrow |F=5\rangle$ *transition, which is the transition excited by the cooling laser. The cooling laser is blue-detuned from resonance by* $1.1\Gamma_{410}$.

Intensity

In most cooling mechanisms, the damping force depends on the intensity of the cooling laser. The FWHM of the fluorescence signal becomes narrower as the intensity of the cooling laser increases, as plotted in figure 4.9. There is a drop in the width of the fluorescence signal as the cooling laser intensity reaches a value S=1.5. For intensities greater than S=1.75, the width of the fluorescence signal does not vary significantly as the laser intensity is increased. This suggests that the cooling effect reaches a saturation level, depending on the laser intensity.

Detuning

The damping force depends on the detuning of the cooling laser, as can be seen from the equation of the force (eq. 1.25). Both blue and red-detunings of the cooling laser were studied. The shape of the fluorescence signal (figure 4.10) is different for red and blue-detuning, implying that optical pumping is not the cause of the narrowing of the fluorescence signal. Optical pumping is symmetric with respect to laser detuning.

For a red-detuned cooling laser, the fluorescence signal has only one Gaussian profile, without a narrow central peak. For a detuning of $\Delta = -1.1\Gamma_{410}$, its FWHM is narrower by 8% less than that of the probe beam. The FWHM of the probe beam fluorescence signal is 2.2mm. The fluorescence signal becomes less equivalent to a Gaussian curve as the detuning decreases, which influences the value of the FWHM and its variation with respect to the detuning.

For a blue-detuned cooling laser, there is a narrow peak at the center of the fluorescence signal (figure 4.10), which is not observed for the case of red-detuning ($\Delta < 0$). The width of the narrow fluorescence peak only slightly varies with detuning (figure 4.10). The amplitude of the fluorescence signal is higher for a smaller values of the detuning. This is due to optical pumping. As the frequency of the cooling laser is further away from resonance, it pumps out less and less atoms from the $|5P_{1/2}, F = 4\rangle$ ground state, which is the state being probed.

Polarization

A spatially-varying polarization of the cooling laser along the atomic trajectory can lead to a cooling effect, depending on the atomic transitions which are optically-excited. For single-frequency cooling at 410 nm, a lin||lin configuration exhibits a more pronounced cooling effect than the lin⊥lin and $\sigma^+ - \sigma^-$ configurations. The amplitude of the narrow peak of the fluorescence signal is highest for the lin||lin case, as shown in figure 4.11. In these measurements, the quantization axis was defined along the propagation axis $\vec{k}$ by applying a small magnetic field of 2 Gauss. The propagation vector $\vec{k}$ is parallel to the magnetic field $\vec{B}$. In this lin||lin configuration, a linearly-polarized light couples all $m_F \rightarrow m'$ transitions. No polarization-gradient is

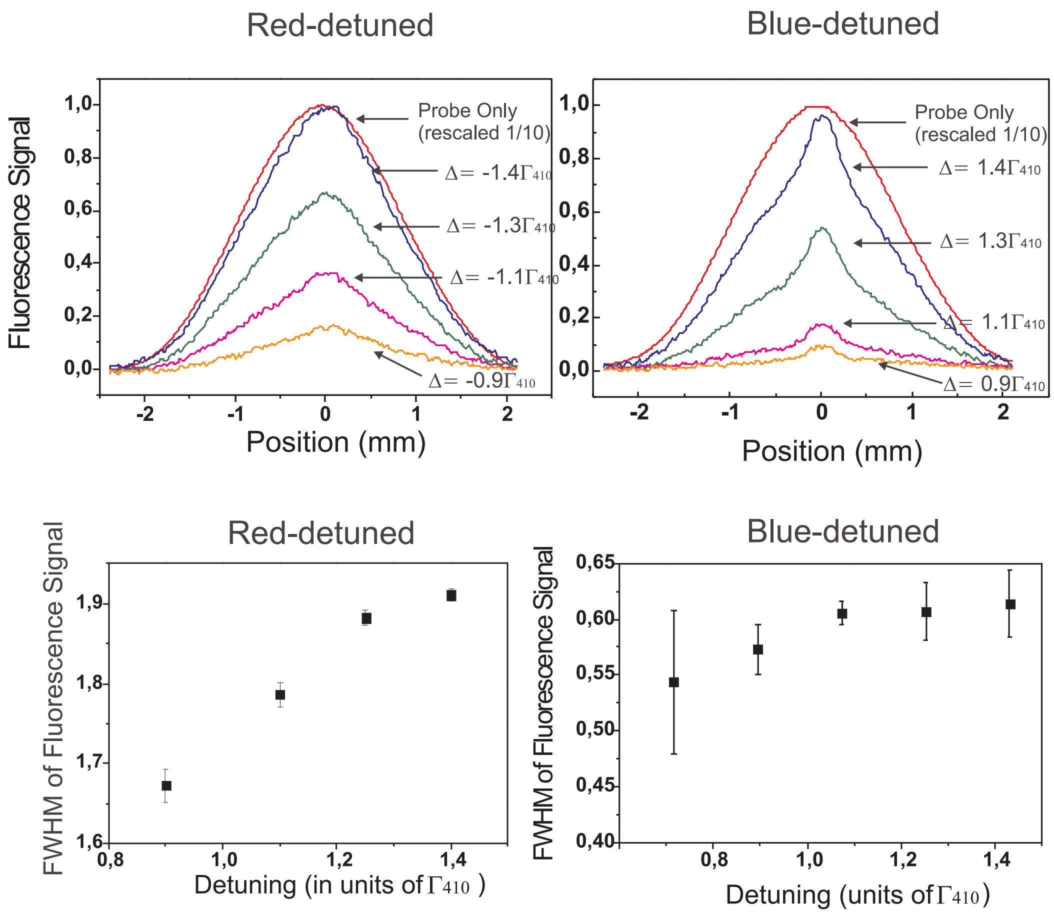

Figure 4.10: *Detuning-dependence of the FWHM of the fluorescence signal with a single-frequency cooling laser, for red-detuning (left) and blue-detuning (right). The cooling laser excites the* $|5P_{1/2}, F = 4\rangle \rightarrow |6S_{1/2}, F = 5\rangle$ *transition and has a saturation parameter of* $S = 2.5S_0$.

present in a lin||lin configuration.

From figure 4.11, the narrowing of the fluorescence signal is still present in a lin⊥lin configuration,, but not as pronounced as for the lin||lin case.

Cooling with Different Transitions

Different cooling transitions were investigated to understand if the angular momentum scheme, $F_g \rightarrow F_e$, influences the cooling effect. In this experiment, only one cooling transition at a time was excited by the 410 nm laser. The probe beam excites all five hyperfine transitions, such that both the 410 nm and 451 nm lasers are orthogonal to the atomic beam at the probe

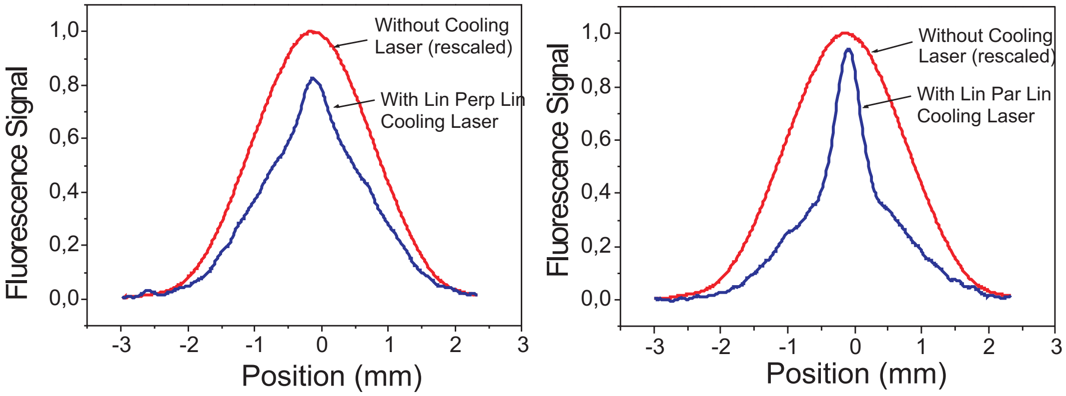

(a) Lin ⊥ Lin Cooling Laser (b) Lin II Lin Cooling Laser

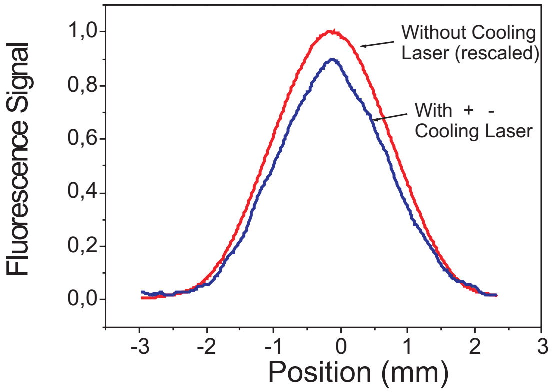

(c) + - Cooling Laser

Figure 4.11: *Polarization dependence of the single-frequency cooling mechanism at 410 nm indium transition. The scaling factor between the curves, with and without cooling laser, is ×90.*

region. With all five-frequencies in the probe region, the velocity distribution of the atoms in the $|5P_{1/2}, F = 4, 5\rangle$ and $|5P_{3/2}, F = 6, 5, 4\rangle$ ground states is detected. The number of atoms which are cooled in each ground state is difficult to determine as this depends on the relative intensities of each probe laser, their detunings and the area of overlap of the five probe lasers. This probing scheme was implemented to minimize the effect of optical pumping when the probe and cooling lasers excite the same transition. It can be seen from figure 4.12 that there is a narrowing of the fluorescence signal for all three transitions, $F = 5 \rightarrow F' = 4$, $F = 5 \rightarrow F' = 5$ and $F = 4 \rightarrow F' = 5$, which implies that the cooling effect is observed for different angular momentum schemes.

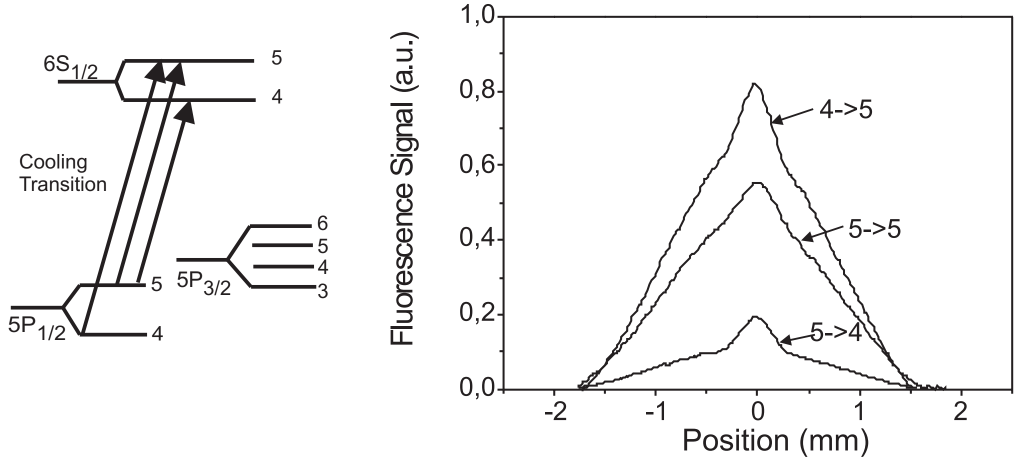

Figure 4.12: *Fluorescence signal when the cooling laser excites one transition at a time. The probe beam consists of both 410nm and 451nm lasers. The atoms in all hyperfine ground states of* $5P_{1/2}$ *and* $5P_{3/2}$*, except for the F=3 state, are being probed.*

Summary

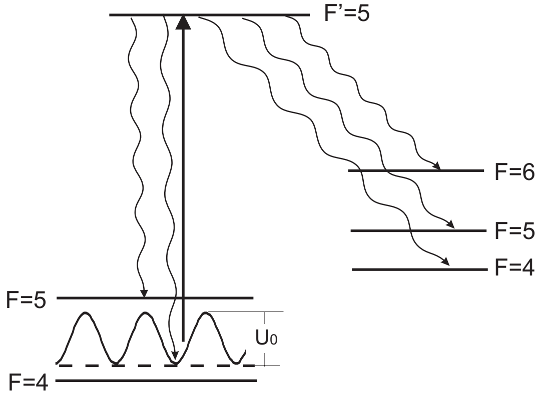

Figure 4.13: *Single-frequency cooling with the 410nm laser can be modelled as a lossy two-level system, with a Rabi frequency* Ω *characterizing the coupling of the atom to the driving field tuned to the* $F{=}4 \rightarrow F'{=}5$ *transition.*

For the single-frequency 410 nm cooling, the phenomenon can be summarized as follows:

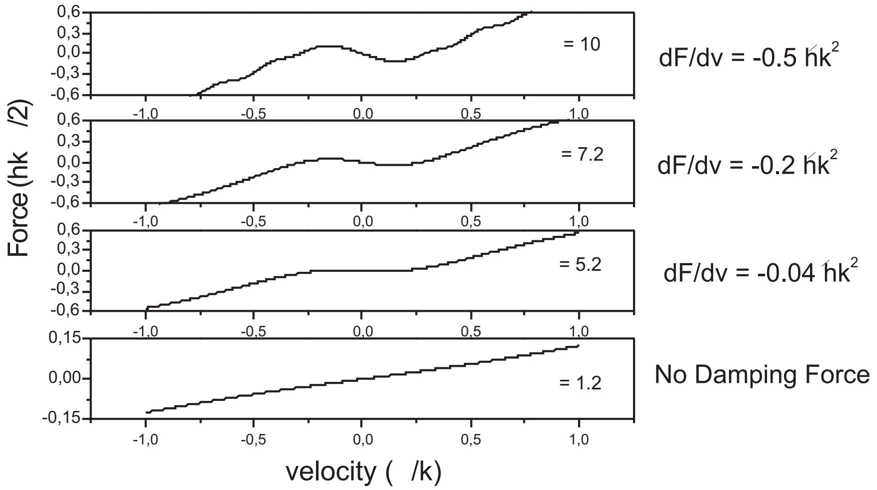

Figure 4.14: *Force as a function of velocity for single-frequency 410 nm cooling. The Rabi frequency* Ω *is varied. The detuning is set at* $\Delta_1 = 1.1\Gamma_{410}$.

(1) The cooling effect is always observed for blue-detuned laser frequency regardless of the angular momentum scheme, $F_g \rightarrow F_e$ transition.
(2) The cooling effect occurs even with lots of loss channels or uncoupled states. The F=4→ F′=5 (410 nm) transition, driven by a linearly-polarized field (no polarization-gradient), can be considered as a lossy two-level system, as shown in figure 4.13.
(3) The cooling effect is observed even with low intensity.

Simulation
To understand the mechanism, the force was calculated using the same procedure as that for the five-frequency cooling scheme, except that all the coupling terms Ω_i are zero except for the Rabi frequency corresponding to the F=4→ F′=5 (410 nm) hyperfine transition. A plot of the force as a function of velocity for a moving atom in the presence of single-frequency, blue-detuned cooling laser is shown in figure 4.14. The Rabi frequency is varied from $\Omega = 1.2\Gamma$ to $\Omega = 10\Gamma$. Experimentally, the intensity of the 410nm cooling laser corresponds to $\Omega = 1.1\Gamma$. From the plot of the force as a function of velocity, there is a damping force only for high intensities, $\Omega > 5.2\Gamma$, but this value is higher than the laser intensities in our experiment.

This leads us to consider another model that can encompass the three phenomena summarized above: low intensity, blue-detuned laser frequency, and several loss channels. All of which are satisfied by the condition in which transient laser cooling was observed. This mechanism was first proposed by Padua, Metcalf, et.al. [43] from experiments on laser cooling of Rubidium.

Transient Laser Cooling

Transient laser cooling can be observed for blue-detuned laser frequencies regardless of the angular momentum scheme. The steady-state condition for solving the damping force is no longer applicable in such transient cooling effect. In this cooling mechanism, an atom experiences a force due to a light shift potential, $U(z) = U_0 \sin^2(kz)$, until it is optically-pumped to an uncoupled state. For indium, the uncoupled states are all the hyperfine ground states of the $5P_{3/2}$ state and one of the $5P_{1/2}$ hyperfine ground states. This cooling mechanism relies on the variation of the optical pumping rate, depending on the atom's position as it enters the standing wave. When an atom is near the node of the standing wave, the optical pumping rate γ_p is slower than at an antinode. The optical pumping rate is zero at the nodes. For blue-detuning, an atom moving away from a node loses more kinetic energy (figure 4.15a) than it gains as it moves away from an antinode (figure 4.15b). The atom climbs the potential hill over a longer time before it is optically-pumped than when it goes down the hill. The opposite happens for the case of red-detuning, wherein the atom gains more kinetic energy as it moves away from a node (figures 4.15c) compared to the kinetic energy it loses when it moves away from an antinode (figure 4.15d).

As calculated by Padua, et.al., when the kinetic energy KE of the atom is greater than $2U_0$, the atom gets optically-pumped when its potential energy is $U_P \sim 5/6 \cdot U_0$, where $U_0 = 2\hbar SC\Delta/[1 + (2\Delta/\Gamma_{410})^2]$. In the indium experiments where the cooling laser excites the $F = 4 \rightarrow F' = 5$ (410 nm) transition, the potential energy is $U_0 = 0.22\hbar\Gamma_{410}$. In this calculation, the saturation parameter is taken to be $S = 3$, a transition strength $C = 1$, and a detuning of $\Delta = 1.1\Gamma_{410}$. The optical pumping rate γ_p is given by [43]:

$$\gamma_p(t) = \tilde{\gamma}_p \sin^2(kz(t)), \tag{4.3}$$

where

$$\tilde{\gamma}_p = \frac{2SCB\Gamma_{410}}{1 + (2\Delta/\Gamma_{410})^2 + SC} \tag{4.4}$$

For the cooling scheme involving one cooling laser exciting the $F = 4 \rightarrow F' = 5$ (410nm) transition, $\tilde{\gamma}_p = 0.6\Gamma_{410}$, where the branching ratio to the uncoupled states B is 0.84, with all the hyperfine ground states of $5P_{3/2}$ and the $|5P_{1/2}, F = 5\rangle$ states as uncoupled states. The probability of optical pumping P(t) between a time interval, t and t+dt is given by [43]:

$$P(t) = \Gamma(t) exp[-\int_0^t \Gamma(t')dt'] \tag{4.5}$$

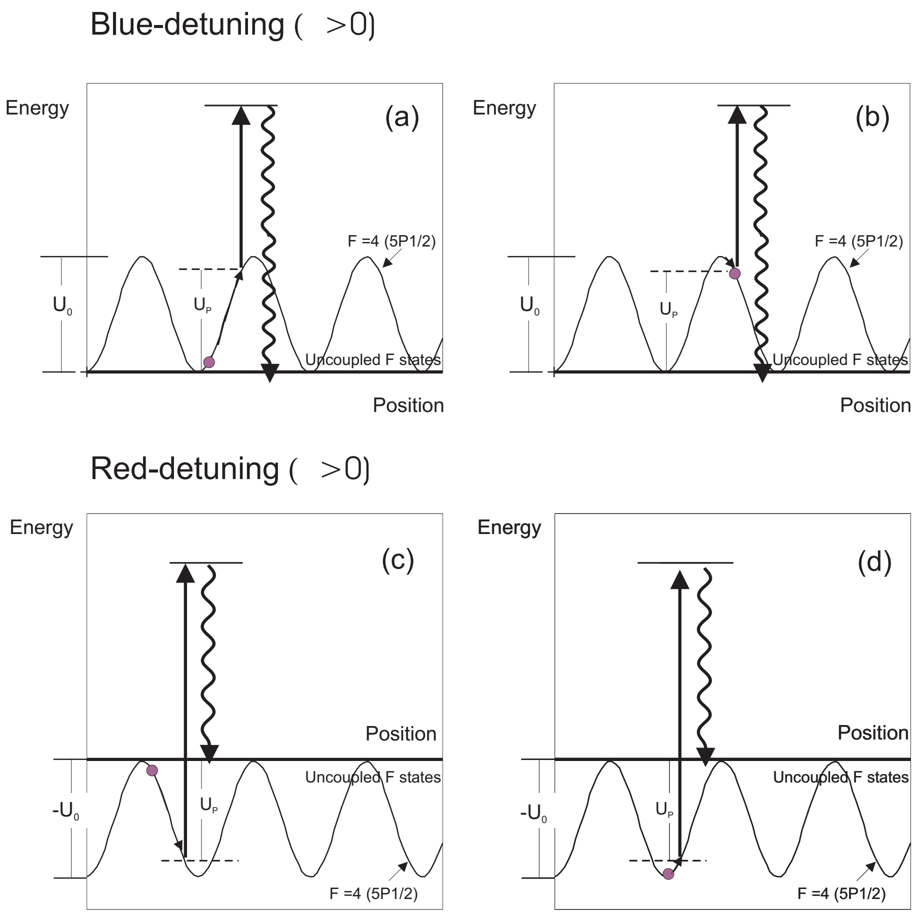

Figure 4.15: *Transient laser cooling mechanism, for blue-detuned cooling laser (a) and (b) and for red-detuned cooling lasers (c) and (d).*

Figure 4.16 shows the optical pumping probability for the experimental conditions of indium single-frequency cooling. It can be seen that for times greater that 1.0μs, there is almost zero probability for optical pumping. In this mechanism, even with less than four pumping cycles, the atom already loses kinetic energy.

The amount of energy loss by the atom ΔKE is equal to the difference between the final energy of the atom before it is optically-pumped, $U_f = 5/6 \cdot U_0$, and the initial average potential energy which is $U_i = U_0/2$. Thus, the kinetic energy loss is ΔKE$=-U_0/3$. For our experimental parameters, S=3 and $\Delta = 1.1\Gamma_{410}$, the energy loss is ΔKE$= -0.07\hbar\Gamma_{410}$. The loss in kinetic energy is directly proportional to the change in velocity Δv and can be written as Δv = v$\cdot$(ΔKE/2KE). In our experiment, for an initial velocity of v=73 cm/s, the change in velocity Δv is only 0.05 cm/s. This value of Δv is only for one initial velocity. To have good estimate of the velocity distribution in the presence of a cooling laser, a quantum Monte Carlo simulation of the atomic trajectories is needed. Such simulations require a lot of computational time and were not executed within the scope of this thesis.

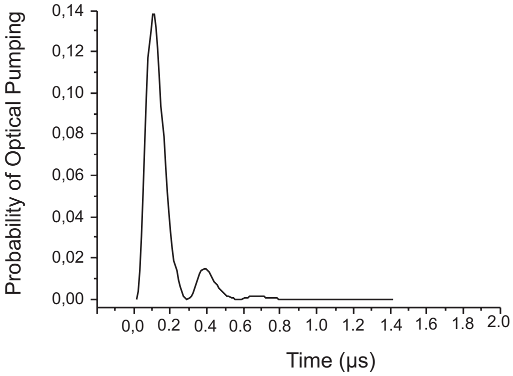

Figure 4.16: *Optical pumping probability as a function of time for S=1, $\Delta = +1.1\Gamma$ and B=0.84.*

4.2 Laser Cooling with 451 nm Lasers

Laser cooling with a 451nm laser provides us a different set of conditions to experimentally realize laser cooling:

(1) The optical pumping dynamics is different for the 451nm transition compared to the 410 nm line because the spontaneous emission rate Γ_{451} of the $6S_{1/2} \rightarrow 5P_{3/2}$ transition is higher than that of the $6S_{1/2} \rightarrow 5P_{1/2}$ transition, which could lead to a different cooling mechanism.

(2) Laser cooling with 451 nm light allows us to investigate high-intensity conditions without sacrificing interaction length, because the 451 nm laser power can be further enhanced. The laser power of the 451 nm light source was increased by changing the frequency-doubling nonlinear crystal from an LBO to a ppKTP crystal.

(3) The 451 nm indium transition has a relatively high transition strength at an $F \rightarrow F-1$ transition ($F{=}6 \rightarrow F'{=}5$). Optical pumping behavior of $F \rightarrow F-1$ transition differs from that of $F \rightarrow F+1$ transition, and this leads to cooling mechanisms, such as blue-detuned polarization-gradient cooling [46], grey molasses [48, 49] and velocity-selective coherent population trapping [51].

(4) Optical pumping effects, when the probe and cooling lasers excite the same transition, are avoided. The probe laser is set at the (410nm) F=4→ F′=5 transition, while the cooling laser is at the 451nm transition. Only the atoms at the $5P_{1/2}$ F=4 state are being detected.

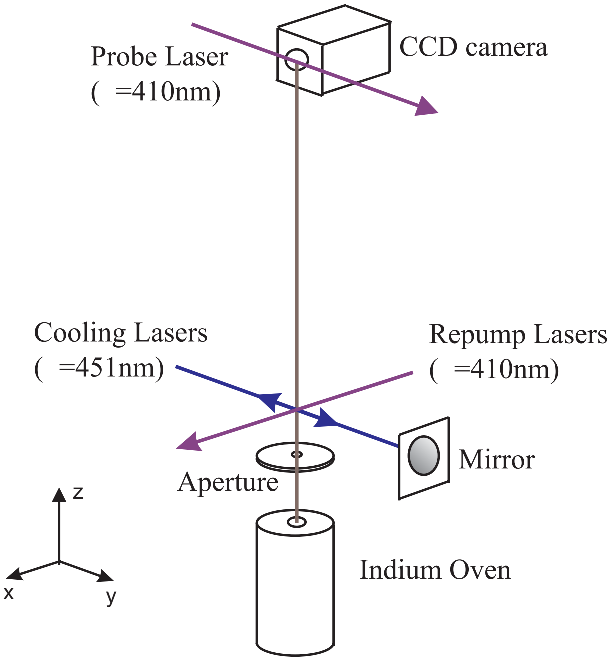

Figure 4.17: *Laser cooling configuration investigated with the 451 nm laser in a standing wave configuration. The role of the 410nm lasers are to repump the atoms to the* $5P_{3/2}$ *state.*

The experimental configuration to achieve laser cooling with 451 nm lasers is shown in figure 4.17. The 451nm lasers are orthogonal to the 410 nm lasers at the cooling region. The probe laser is parallel to the 451 nm laser, such that only the effect of the 451 nm laser on the atomic beam is being detected. The role of the 410 nm laser is to optically pump the atoms to the $5P_{3/2}$, because the thermal population of the $5P_{3/2}$ state is only 20% at a temperature of 1200°C. The 410 nm lasers excite the two ground-state hyperfine transitions at $5P_{1/2}$, as shown in figure 4.18. One of the repumping 410 nm lasers operates at the same transition as the probe laser, the $|5P_{1/2}, F = 4\rangle \rightarrow |6S_{1/2}, F = 5\rangle$ transition. This laser partially pumps out the atoms in the state being probed. Without the 451 nm laser, only $\sim 1\%$ of the initial population remain in the $|5P_{1/2}, F = 4\rangle$ state, as shown in in figure 4.19 labelled as repumpers only.

The 451 nm lasers act as cooling lasers while the 410nm lasers act as repumpers, as shown in the scheme in figure 4.18. The power of the 451 nm laser is 50 mW at the cooling region. The intensity for each transition is $200\,\mathrm{mW/cm^2}$. The interaction length is initially set at 3 mm. This translates into an interaction time of $t_{int} = 5.7\,\mu$s. The detuning of the 451 nm laser is changed by varying the carrier frequency.

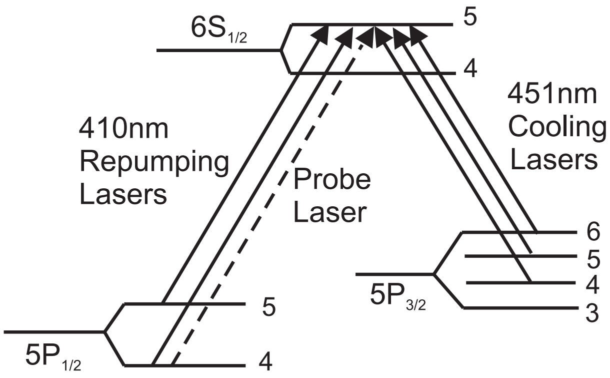

Figure 4.18: *Laser cooling scheme with 451nm cooling lasers. The 410 nm lasers act as repumpers to increase the population of the* $5P_{3/2}$ *state.*

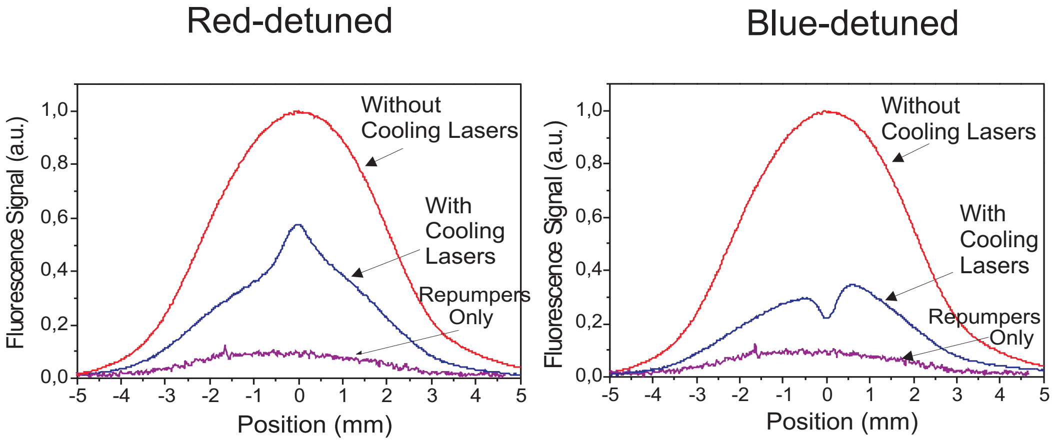

Figure 4.19: *A narrowing of the fluorescence signal for the red-detuned case and a dip at the center of the fluorescence signal for the blue-detuned was observed when a 451 nm cooling laser excites the three hyperfine transitions (F=6,5,4 → F′=5 transition). The fluorescence signals with cooling lasers are rescaled by ×2 and those for 'repumpers only' are rescaled by ×10 for better visibility. The 451 nm lasers are in a lin⊥lin configuration.*

4.2.1 Multi-frequency Laser Cooling

Experimental Observations for Multi-frequency 451nm Cooling

(1). When the 451 nm laser excites the three-hyperfine transitions ($|F = 6,5,4\rangle \rightarrow |\mathrm{F}' = 5\rangle$), a narrowing of the fluorescence signal was observed for red-detuning with $\Delta = -1\,\Gamma_{451}$, as shown in figure 4.19. On the other hand, a dip in the fluorescence signal was observed for blue-detuning at Δ=+1 Γ_{451}, as shown in figure 4.19 (right figure). This holds for lin‖lin and lin⊥lin configuration of the cooling lasers. This is what is expected for Doppler cooling mechanism, in which a cooling effect is observed for red-detuning, and a heating effect for blue-detuning. The FWHM of the narrow fluorescence peak without the Gaussian background is 1.2 mm. An estimate of the FWHM of the velocity distribution with cooling laser gives 39 cm/s, for a FWHM without cooling lasers of 72 cm/s. This value is higher than the Doppler velocity limit of 20.8 cm/s.

(2). Without the 410 nm repumping lasers, no cooling signal was observed. The atoms at the $5\mathrm{P}_{3/2}$ state have to undergo several optical pumping cycles before they are cooled.

(3). The 451 nm laser not only slows the atoms in the transverse direction, but it also increases the atomic population at the $5\mathrm{P}_{1/2}|\mathrm{F}{=}4\rangle$ state. From the amplitude of the fluorescence signal, 18% of the atoms are pumped back to the $5P_{1/2}$ F=4 state by the 451nm lasers, when all three hyperfine transitions $|F = 6,5,4\rangle \rightarrow |F' = 5\rangle$ are coupled, for a detuning of $\Delta = +1\,\Gamma_{451}$, as shown in figure 4.19. The 451 nm lasers optically pump the atoms to the state being probe.

(4). In a lin⊥lin configuration of the cooling lasers, an interesting phenomenon was observed. In this experiment, the 451 nm laser excites two hyperfine transitions, $|F = 6,4\rangle \rightarrow |F = 5\rangle$ (refer to figure 4.20). When the laser power is high (P=50 mW for both transitions or S=2.5 [6 → 5]), a narrowing of the fluorescence signal is seen for red-detuning. As the laser power is decreased to 14 mW (S=0.7) and to 5 mW (S=0.25), a dip in the fluorescence signal is observed for red-detuning, as shown in figure 4.20. The cooling signal turns into a heating signal for the same detuning ($\Delta = -1\,\Gamma_{451}$) as the laser power is decreased.

This can be explained as follows, when the 451 nm cooling lasers are blue-detuned, radiation pressure heating and polarization-gradient cooling at the F=6→ F′=5 transition are the two competing processes. When the cooling transition is an $F \rightarrow F-1$ transition, polarization-gradient cooling occurs for blue-detuned cooling lasers [46, 47]. As the laser power is decreased, polarization-gradient cooling becomes a more dominant effect. Thus, the

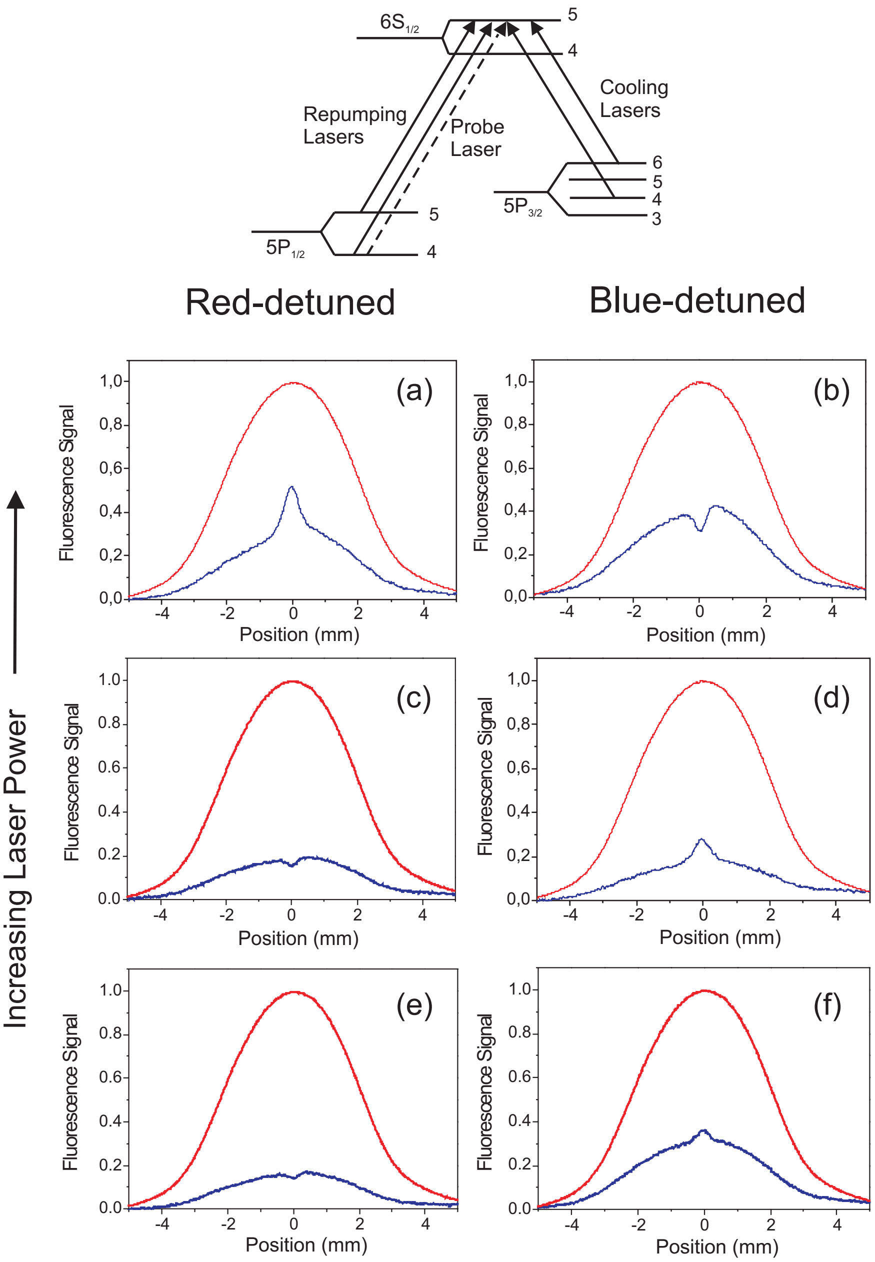

Figure 4.20: *The 451 nm lasers are in a lin⊥lin configuration. As the laser power decreases, the cooling signal turns into a heating signal for the same detuning ($\Delta = -1\Gamma_{451}$). Figures (a) and (b) correspond to a laser power of 50 mW, (c) and (d) to 14 mW, and (e) and (f) to 5 mW. The fluorescence signals, for the case with cooling lasers, are rescaled by ×2 for better visibility.*

cooling signal occurs at blue-detuning. It should be noted that the transition probability for the F=6→ F′=5 transition is 65% of the total decay probability from the $6S_{1/2}$ excited state, while that for the F=4→ F′=5 is only 12%.
Laser cooling experiments involving one cooling transition were pursued to understand the cooling mechanism. The laser intensity, detuning and polarization were varied one at at time to understand the dependence of the cooling effect on these parameters. This will be presented in the next section.

4.2.2 Single-frequency Laser Cooling

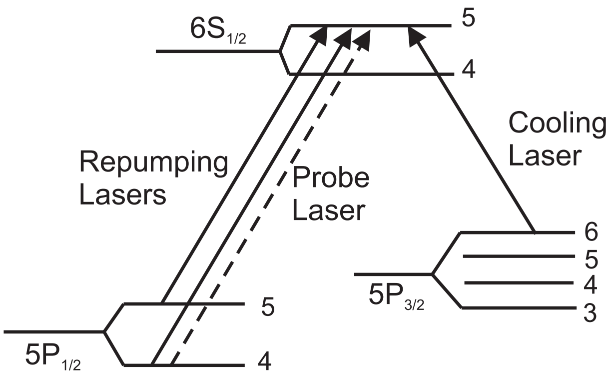

Figure 4.21: *Laser cooling scheme with 451 nm cooling laser, exciting one hyperfine transition (F=6 → F′=5). The 410 nm lasers act as repumpers to increase the population of the $5P_{3/2}$ state.*

The simplest configuration to investigate is one-transition cooling at F=6→ F′=5 (451nm) transition. The 410 nm repumping lasers are present to increase the population at the $5P_{3/2}$ state, but their propagation directions are orthogonal to the 451 nm cooling laser and to the probe laser. Only the effect of the 451 nm laser on the transverse atomic velocity is being detected. The interaction length is 5mm, which corresponds to an interaction time of 9.4μs. The maximum power of the cooling laser is 50 mW, corresponding to a saturation parameter S_0=6. Since only one hyperfine transition is excited, there are two loss channels which are not coupled by the light field.
The cooling laser is in a lin||lin configuration and it excites the F=6→ F′=5 (451 nm) transition, as shown in figure 4.21. With only one cooling transition, a different effect is observed compared to that for three cooling transitions described earlier. A cooling effect is observed for blue-detuned laser frequency and a heating effect for the red-detuned case, as shown in figure 4.22. The FWHM of the narrow fluorescence signal is approximately 0.3 mm.

It is difficult to explain such small width of the narrow fluorescence peak. Nonetheless, an estimate of the FWHM of the transverse velocity distribution v_T of the atoms can be obtained, that is $v_T = 10\,cm/s$.

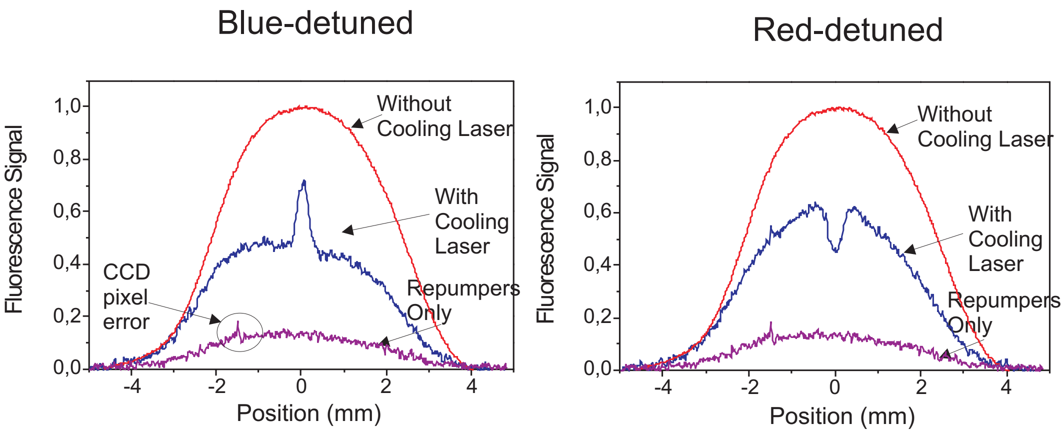

Figure 4.22: *A single-frequency cooling laser, at F=6 → F′=5 (451nm) transition, causes a narrowing of the fluorescence signal for the blue-detuned case ($\Delta = 1.1\,\Gamma_{451}$) and a dip at the center of the fluorescence signal for the red-detuned case($\Delta = -1.1\,\Gamma_{451}$). The fluorescence signals in the presence of the 410nm repumpers and with cooling laser are rescaled by ×6 for better visibility. The power of the 451nm laser is 50mW.*

Intensity

For these measurements, the cooling laser excites the F=6→ F′=5 transition, and is blue-detuned by $\Delta = +1\Gamma_{451}$. The laser intensity is varied by changing the laser power, while the interaction area is kept constant. In figure 4.23, the FWHM of the fluorescence signal of the cold atoms is plotted as a function of cooling laser intensity, which is obtained from a Gaussian fit of the narrow fluorescence peak. It can be seen that the FWHM of the narrow fluorescence signal or final atomic velocity distribution does not vary when the laser power is changed. The fraction of cold atoms, on the other hand, varies as a function of the laser intensity, as can be seen in figure 4.24.

The fraction of cold atoms N_{cold} is given by:

$$N_{cold} = A_1/A_2 \tag{4.6}$$

where A_1 is the area of the narrow peak of the fluorescence signal and A_2 is the area of the Gaussian background. As the laser intensity increases, the number of cold atoms in the state being probed also increases. The FWHM

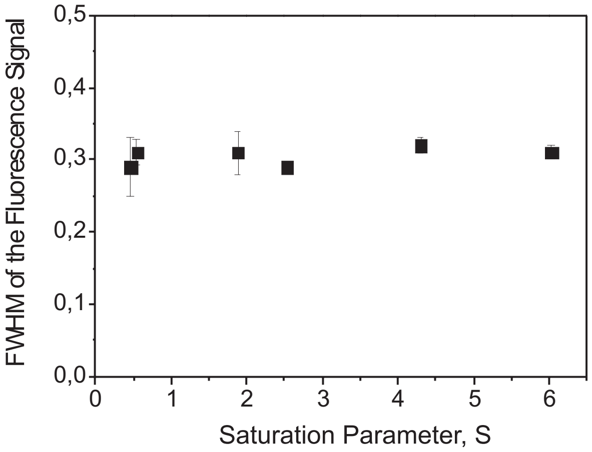

Figure 4.23: *Variation of the FWHM of the fluorescence signal of cold atoms as a function of saturation parameter. The cooling laser excites the F=6→* $F' = 5$ *(451nm) transition, and is blue-detuned by* $\Delta = 1.1\,\Gamma_{451}$.

of the narrow fluorescence peak does not change, however, which means that the transverse velocity distribution of the atomic beam did not become lower with higher laser power.

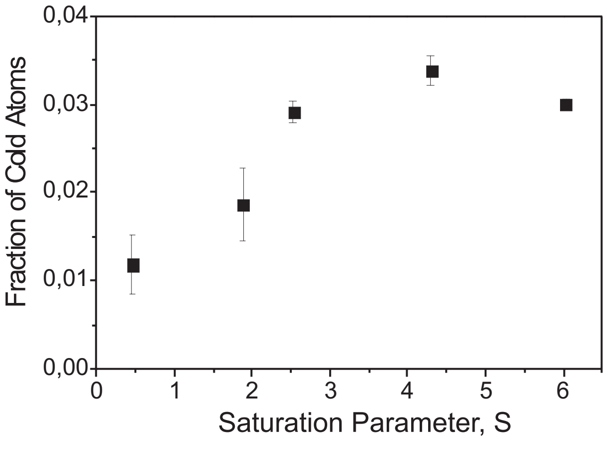

Figure 4.24: *Variation of the fraction of cold atoms as a function of the saturation parameter. The cooling laser excites the F=6→* $F' = 5$ *(451 nm) transition, and is blue-detuned by* $\Delta = 1.1\,\Gamma_{451}$.

Detuning

In these measurements, a single-frequency 451 nm cooling laser excites the F=6→ F'=5 transition. Despite the technical difficulty in determining the exact resonance frequency, the cooling signal consistently occurs at a higher frequency (blue-detuned) relative to that of a heating signal.

The technical difficulty in determining the resonance frequency is due to the instability of the frequency markers and their consistency when compared to each other. One frequency marker is the two-color absorption signal, which depends on the frequency stability of the pump laser (410 nm laser). The other frequency marker is the fluorescence spectrum from the atomic beam, which can not be done in-situ during the laser cooling experiments because it utilizes the same atomic beam. The values of detuning, given in figure 4.25, is obtained by using the fluorescence spectrum of the atomic beam to determine the resonance frequency. Throughout the measurements, the power of the laser is kept constant at 47 mW.

It was observed that the fraction of cold atoms and the shape of the fluorescence signal are sensitive to the detuning, as shown in figure 4.25. From the shape of the fluorescence signal in figure 4.25(left), it can be seen that the atomic velocity distribution is influenced by the laser detuning. It was also observed that there is an optimum detuning, wherein the fraction of cold atoms is maximum and the narrow fluorescence peak has a minimum width and maximum amplitude, which in this case is $\Delta = +1.2\Gamma$. In polarization-gradient cooling, transient cooling and other cooling mechanisms which relies on optical pumping, the amount of light shift energy, which depends on the detuning, is important in determining the final atomic velocity distribution.

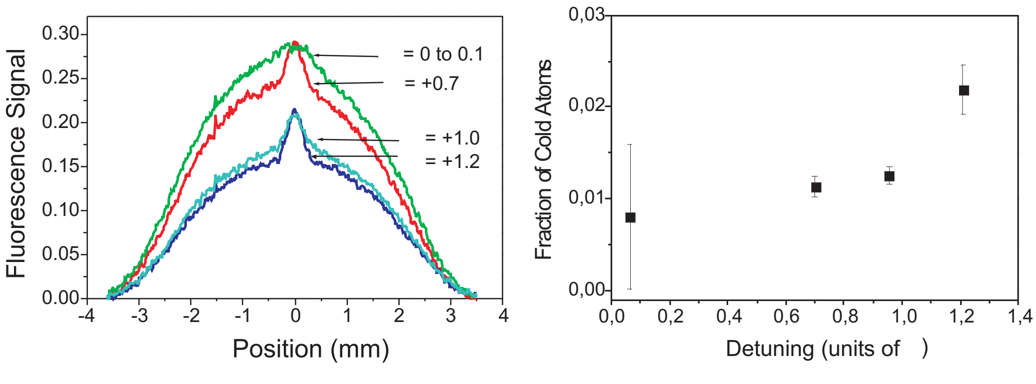

Figure 4.25: *A single-frequency 451nm cooling laser excites the F=6→ F'=5 transition. The fraction of cold atoms as a function of detuning is shown above.*

Polarization

A comparison of the two fluorescence signals between a lin||lin cooling configuration and a lin⊥lin configuration is shown in figure 4.26. It can be seen that with polarization-gradient, the narrow fluorescence peak is still present, and the width of the broad background becomes slightly narrower. For lin⊥lin configuration, the broad background is due to the fact that not all velocity groups satisfy the condition $kv_T \ll \omega_{LS}$, where $\hbar\omega_{LS}$ is the light shift energy. For the lin⊥lin configuration, the damping force is calculated for the F=6→ F=5 transition and this will be presented in the next section.

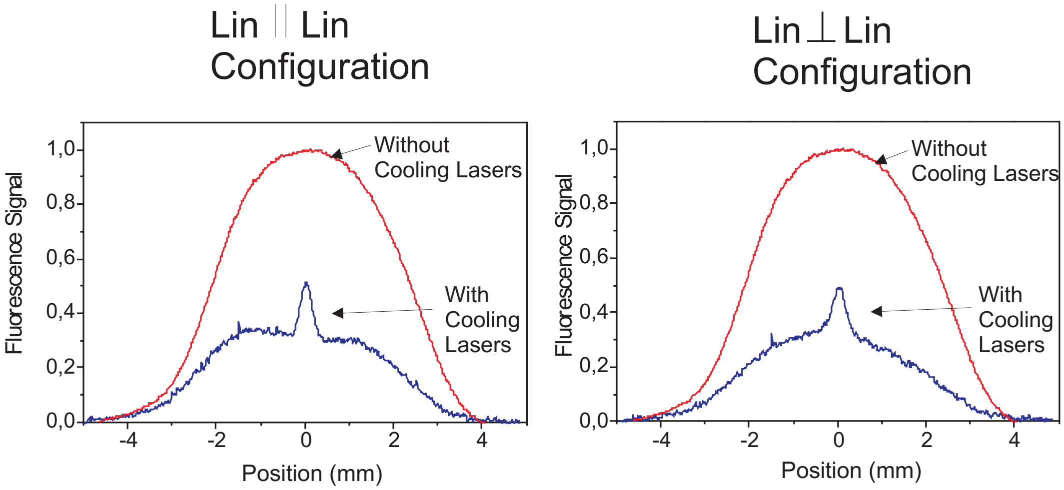

Figure 4.26: *A narrowing of the fluorescence signal for both standing wave and lin⊥lin configuration was observed. The 451 nm cooling laser excites one hyperfine transition (F=6 → F′=5). The fluorescence signals with cooling lasers are rescaled by ×4 for better visibility. The power of the 451nm laser is 21mW and the detuning is* $\Delta = 1.1\,\Gamma_{451}$.

Discussion

From the intensity measurements, the FWHM of the fluorescence signal does not change with laser power. This implies that Doppler force is not the dominant force in this experiment since it varies with intensity. For polarization-gradient cooling, the damping coefficient does not depend on laser power, but the width of the velocity distribution does, if momentum diffusion is taken into account [46]. In transient laser cooling, the amount of kinetic energy loss or the change in the velocity distribution also depends on the laser intensity. This almost non-varying behavior of the FWHM of the fluorescence signal

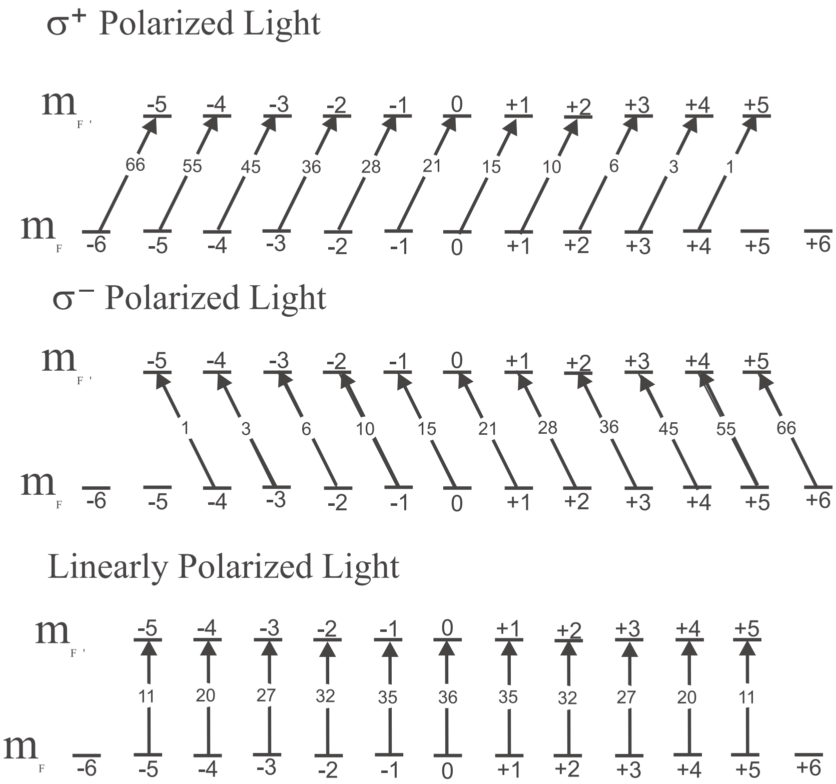

Figure 4.27: *Optical pumping for the F=6→ F′=5 transition when excited by a σ+, σ− circularly-polarized and linearly-polarized light. The number between the ground and excited states should be multiplied by 1/66 to give the transition strength for each coupled* $m_f \rightarrow m'_f$ *transition.*

with laser power should be investigated further in the two extreme ends, the low ($S \ll 1$) and the high-intensity regimes.

The cooling effect is observed for blue-detuning, when the $F = 6 \rightarrow F' = 5$ transition is the cooling transition in the lin$\perp$lin and lin$||$lin configurations. It is known that if an $F \rightarrow F - 1$ transition is excited, polarization-gradient cooling occurs for blue-detuning[47].

Simulation for Polarization-Gradient Cooling

To estimate the amount of damping force for polarization-gradient cooling for the $F = 6 \rightarrow F = 5$ transition, the transition strengths are calculated for different polarization configurations and is shown in figure 4.27. The energy light shifts for the m_f ground states of the $F = 6 \rightarrow F = 5$ transition are calculated for our experimental parameters, and tabulated in appendix E.

The average damping force for a lin$\perp$lin configuration has been calculated by different groups working on laser cooling [46, 50, 47]. The indium atomic scheme is more complicated than the (5+3)-level scheme, which was rigorously calculated by Chang, et al. Nonetheless, the previous methods can be extended to a (13+11)-level scheme, which is the F=6→ F′=5 transitions of indium. The force due to a one-dimensional optical field with polarization-gradient is given by :

$$F(y,t) = -\langle \frac{dH}{dy} \rangle = -\langle \frac{d}{dy} (\vec{\mathrm{d}}^{+} \cdot \vec{E}^{+}(y) e^{-i\omega t} + \vec{\mathrm{d}}^{-} \cdot \vec{E}^{-}(y) e^{i\omega t}) \rangle \tag{4.7}$$

where $\vec{\mathrm{d}}$ is the electric dipole operator, the (+) and (-) superscripts indicate the raising and lowering parts, respectively, and $\vec{E}$ is the electric field at any point along the y-axis, the (+) and (-) superscripts indicate the positive and negative frequency components of the field. The electric field $\vec{E}^{+}$ in a lin⊥lin configuration can be written as follows:

$$\vec{E}^{+}(y,t) = E_0[\cos(k_1\, y)(\hat{\epsilon}_x + \hat{\epsilon}_z) - i\, sin(k_1\, y)(\hat{\epsilon}_x - \hat{\epsilon}_z)] e^{-i\omega_L t} + c.c. \tag{4.8}$$

where k_1 is the wavenumber for the 451nm lasers, and the propagation direction is along y-axis. For the F=6→ F′=5 transition, the average force can be written as:

$$\begin{aligned} F \;=\; & \frac{\hbar\, k_1\, \Omega}{\sqrt{2}} \cos(k_1 y) [\, \tilde{\rho}(g_{-6}, e_{-5}) + \sqrt{\frac{55}{66}}\, \tilde{\rho}\,(g_{-5}, e_{-4}) + \sqrt{\frac{45}{66}}\, \rho\,(g_{-4}, e_{-3}) \\ & \quad + \sqrt{\frac{6}{11}}\, \tilde{\rho}\,(g_{-3}, e_{-2}) + \sqrt{\frac{28}{66}}\, \tilde{\rho}\,(g_{-2}, e_{-1}) + \sqrt{\frac{7}{22}}\, \tilde{\rho}\,(g_{-1}, e_{0}) \\ & \quad + \sqrt{\frac{5}{22}}\, \tilde{\rho}\,(g_{0}, e_{+1}) + \sqrt{\frac{10}{66}}\, \tilde{\rho}\,(g_{+1}, e_{+2}) + \sqrt{\frac{1}{11}}\, \tilde{\rho}\,(g_{+2}, e_{+3}) \\ & \quad + \sqrt{\frac{1}{22}}\, \tilde{\rho}\,(g_{+3}, e_{+4}) + \sqrt{\frac{1}{66}}\, \tilde{\rho}\,(g_{+4}, e_{+5})\,] e^{-i\omega_L t} \\ & + \frac{\hbar\, k_1\, \Omega}{\sqrt{2}} \sin(k_1 y)\, [\sqrt{\frac{1}{66}}\, \tilde{\rho}\,(g_{-4}, e_{-5} + \sqrt{\frac{1}{22}}\, \tilde{\rho}\,(g_{-3}, e_{-4}) + \sqrt{\frac{1}{11}}\, \tilde{\rho}\,(g_{-2}, e_{-3}) \\ & \quad + \sqrt{\frac{10}{66}}\, \tilde{\rho}\,(g_{-1}, e_{-2}) + \sqrt{\frac{15}{66}}\, \tilde{\rho}\,(g_{0}, e_{-1}) + \sqrt{\frac{21}{66}}\, \tilde{\rho}\,(g_{+1}, e_{0}) \\ & \quad + \sqrt{\frac{28}{66}}\, \tilde{\rho}\,(g_{+2}, e_{+1}) + \sqrt{\frac{6}{11}}\, \tilde{\rho}\,(g_{+3}, e_{+2}) + \sqrt{\frac{45}{66}}\, \tilde{\rho}\,(g_{+4}, e_{+3}) \\ & \quad + \sqrt{\frac{55}{66}}\, \tilde{\rho}\,(g_{+5}, e_{+4}) + \tilde{\rho}(g_{+6}, e_{+5})\,]\, e^{i\omega_L t} \end{aligned} \tag{4.9}$$

where $\rho(g_n, e_m)$ is related to the steady-state population, as described in equation 4.2, and the factors before each term are the Clebsch-Gordan coefficients for each $m_F \rightarrow m'_F$ transition (refer to figure 4.27). Equation(4.9) can be interpreted as the force when an atom interacts with a σ^+ polarized light and a σ^- polarized light, shifted by $\lambda/4$ relative to each other.

To obtain the damping force, the density matrix elements are calculated by numerically integrating the Liouvillian equation. In this calculation, only one hyperfine transition at 451nm is considered, that is, the $F = 6 \to F' = 5$ transition. Excitation in the 410 nm transition is not incorporated into the equation. This transition has an effect on the population of the $5P_{3/2}$ state. However, in our experimental scheme, the 410 nm lasers are linearly-polarized and are in a traveling wave configuation. This means that all Zeeman sublevels of the $5P_{1/2}$ to $6S_{1/2}$ are coupled. The coupling of the Zeeman sublevels in the Lambda-system of $5P_{1/2} \leftrightarrow 6S_{1/2} \leftrightarrow 5P_{3/2}$ is not critical. What is significant is the coupling between the $5P_{3/2}$ and $6S_{1/2}$ Zeeman sublevels because only the 451nm laser is in a lin⊥ lin configuration. Furthermore, since the propagation directions of the 410 nm lasers are orthogonal to the 451 nm laser (figure 4.17), the directions of the force due to the 410 nm and 451 nm lasers are also orthogonal to each other. Only the damping force due to the 451 nm laser, which is in the direction parallel to the probe beam, is of interest in this experiment.

Figure 4.28 shows the force as a function of velocity with the assumptions mentioned above. It can be seen that there is a damping force for blue-detuned laser frequency in a lin⊥lin configuration. The damping coefficient is dF/dv= $-2\hbar k^2$ at v=0. The velocity capture range, as seen in figure 4.28, is -0.01Γ_{451}/k $\leq$ v $\leq$ 0.01Γ_{451}/k, which is $v_T \simeq 7 cm/s$. The damping coefficient in this calculation is larger than that obtained for the five-frequency cooling scheme with 410nm cooling lasers, such that, the expected velocity distribution is narrower compared to the latter case. It is also observed experimentally that the width of the velocity distribution is smaller for the single-frequency (451nm) lin⊥lin configuration, than with the five-frequency (410nm) cooling scheme. In the plot of the force as a function of velocity (figure 4.28), the slope is positive for velocities outside the velocity capture range, which accounts for Doppler heating.

4.3 Summary

There is an observed narrowing of the atomic velocity distribution for a five-frequency cooling scheme. This effect occurs for blue-detuned 410 nm laser frequencies and resonant 451 nm laser. A damping force for such scheme was calculated by using a semi-classical approach, in which the Liouvillian equation for a moving atom is solved by numerical integration.

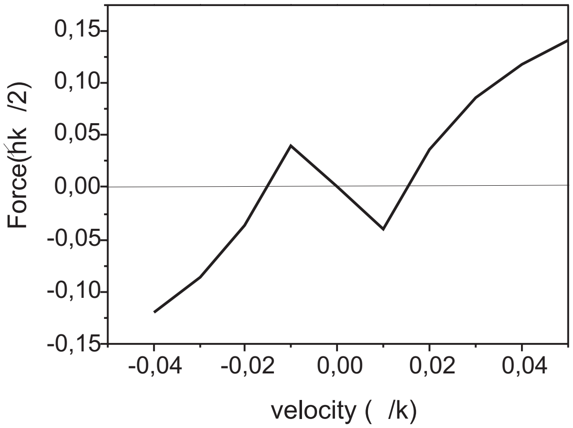

Figure 4.28: *Force as a function of velocity for a lin⊥lin configuration for the F=6→ F′=5 transition. The detuning is* $\Delta = 0.5\,\Gamma_{451}$ *and the saturation parameter is* $\Omega = 2\Gamma_{451}$.

Experiments with a single-hyperfine cooling transition at 410 nm show that the cooling effect still occurs with blue-detuned cooling laser, despite of several loss channels. In the calculation, there is no damping force for a single-frequency 410nm cooling scheme with our set of experimental parameters. This can be phenomenologically explained as a transient cooling effect, in which the steady-state condition for solving the damping force is no longer applicable.

For 451 nm laser cooling experiments, a narrowing of the atomic velocity distribution was observed for red-detuned 451 nm lasers when all three hyperfine transitions were optically-excited. This effect was seen for both standing wave configuration and lin⊥lin configuration. Experiments with a single hyperfine cooling transition show that a cooling effect occurs for blue-detuned laser frequency. The possible mechanisms are polarization-gradient cooling and transient laser cooling. Further systematic studies need to be conducted to understand the mechanism behind the 451 nm laser cooling.

Chapter 5

Conclusion and Outlook

This thesis presents experiments on one-dimensional transverse laser cooling of an indium atomic beam. It was demonstrated that the width of the atomic velocity distribution decreases when the optical fields interact with the indium atomic beam. The extent of narrowing of the atomic velocity distribution depends on the laser cooling configuration.

The critical path towards the realization of laser cooling of indium lies on the experimental set-up of the laser sources and the atomic beam. The laser sources consist of two 410 nm diode lasers and a frequency-doubled Ti:Sapphire laser at 451 nm. Additional frequency components at the 451nm wavelength are necessary to simultaneously excite the hyperfine transitions, thus, an electro-optic modulator (EOM) and an acousto-optic modulator (AOM) are utilized. Aside from the optical set-up, the atomic beam source, which consists of the vacuum chamber and the indium oven, was built.

A significant part of this thesis was dedicated to developing methods for laser frequency-stabilization and spectroscopy of indium in an all-sapphire spectroscopy cell, to ensure that the laser frequencies excite the relevant atomic transition. The 410nm lasers were stabilized by locking the laser frequency to the side-fringe of the Lamb-dip signal and to the slope of the dispersive-shaped signal of the saturated absorption spectrum with current-modulation method. From the Allan variance curve, the frequency stability of the laser locked to the side-fringe of the Lamb-dip signal is 260kHz for an integration time of 1 sec, which is stable enough for laser cooling experiments. For the 451nm laser, two-color absorption spectroscopy in an all-sapphire cell was studied. However, there is no suitable transition line in an all-sapphire cell that can be utilized to actively lock the 451nm laser frequency to an atomic transition frequency. The 451nm laser is locked to an external Fabry-Perot cavity to minimize the frequency drift. To address the issue of frequency-stabilization of the 451nm laser to an atomic transition, two-color polarization spectroscopy could be employed. A dispersive signal can be obtained from the two-color absorption lines of indium, when pumped by a circularly-polarized 451nm laser. This spectroscopy method is, however, complicated when applied to an indium atomic sample due to the number of Zeeman sublevels involved. Nonetheless, this method is promising for frequency stabilization of the 451 nm laser.

Laser cooling of an indium atomic beam was investigated for different experimental configurations and laser parameters. Conventional Doppler cooling was not observed for five-frequency cooling scheme in which the 410nm transitions are optically-excited. A cooling effect is observed for blue-detuned laser frequency, which is contrary to the necessary frequency condition in Doppler cooling. Despite several loss channels, the blue-detuned cooling effect persists in a single-hyperfine cooling transition at 410nm. To understand this mechanism, the Liouvillian equation for a moving atom using a semi-classical approach was solved by numerical integration, and a damping force was obtained for the case of five-frequency cooling scheme. For the 410nm single-frequency cooling, a phenomenological interpretation of the experiment result is given in terms of a transient cooling effect. The expected Doppler-type cooling was observed with red-detuned, 451nm laser cooling scheme involving all three hyperfine transitions. Single-frequency laser cooling experiments at 451nm show that the narrowing of the atomic velocity distribution occurs when the laser frequency is blue-detuned.

Outlook

The aim of laser cooling in atom lithography is to obtain a significant enhancement of the atomic flux. To achieve this, the velocity capture range of the cooling force should be increased and for this, a Doppler cooling scheme is proposed. The interaction area between the laser beams and the atomic beam has to be increased, such that the interaction time is much larger than the damping time. The 451nm laser should be the cooling laser because of its relatively high power and the 410nm lasers should be used as repumping lasers. Laser cooling configurations, as shown figure 5.1, wherein the laser beams pass through the atomic beam several times can lead to a large interaction length, not at the cost of laser power. The scheme in figure 5.1 (b) was realized by Hoogerland et. al. for atomic beam brightening experiment [52].

The long-term goal of this experiment is to deposit indium atoms on a substrate using a standing wave light mask, as shown in figure 5.2. Once the

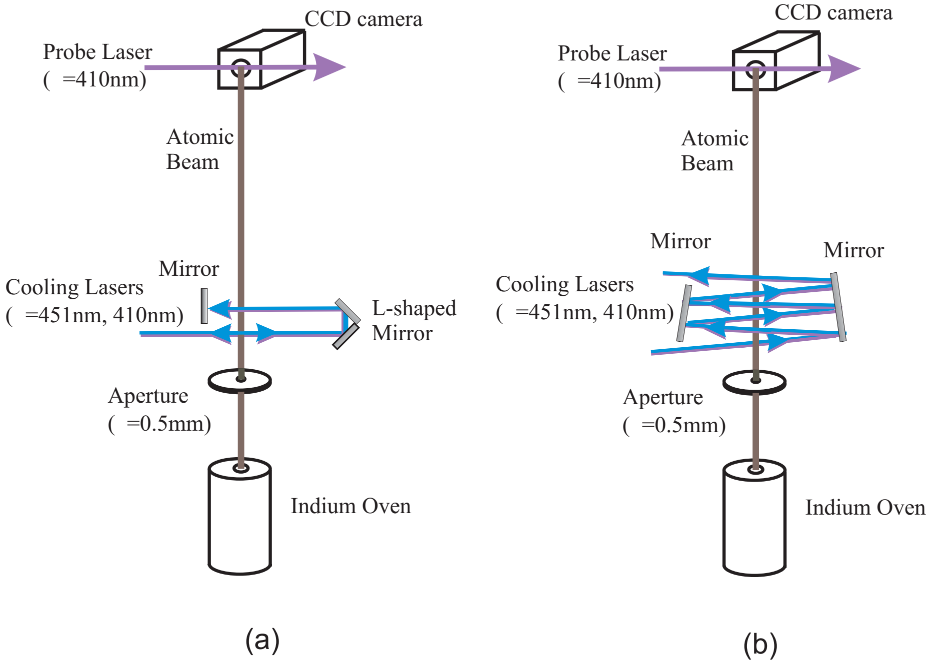

Figure 5.1: *Experimental schemes to realize Doppler cooling.*

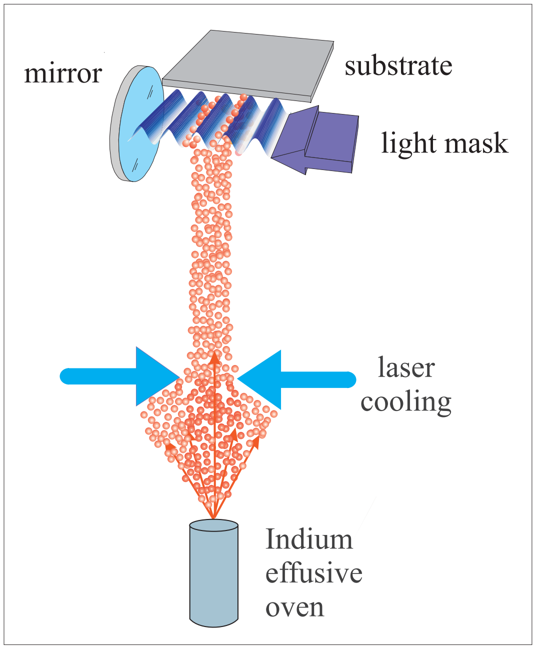

Figure 5.2: *Atom lithography with indium.*

atomic beam flux is increased by laser cooling method, atom lithography with indium is achievable.

Appendix A

Saturation Intensity

The Rabi frequency Ω for each $J \rightarrow J'$ transition, driven by a field E, can be expressed in terms of the reduced dipole matrix element $\langle J\|d\|J'\rangle$ using the equation [53]:

$$\hbar\Omega = (-1)^{J-m}\sum_{q}(-1)^{q}E_{q}\langle J\|d\|J'\rangle \begin{pmatrix} J & 1 & J' \\ -m & q & m' \end{pmatrix} \tag{A.1}$$

where q signifies the polarization of the electric field (q=0 (linearly-polarized), 1 (σ^{+} circularly-polarized), -1(σ^{-} circularly-polarized)).
The value of the Rabi frequency is related to an experimentally measurable parameter, the spontaneous emission rate Γ by the following [11, 13]:

$$[\langle J\|d\|J'\rangle]^2 = \frac{3\mathrm{e}^2\Gamma\lambda^3}{32\pi^3 c\alpha}(2J'+1) \tag{A.2}$$

where e is the electron charge, α is the fine structure constant, J' and J are the angular momenta of the upper and lower states, respectively.
The saturation parameter on resonance S_0 is related to the Rabi frequency by:

$$S_0 = \frac{\Omega^2}{\Gamma_1 \cdot \Gamma_2} = \frac{2\Omega^2}{\Gamma^2} \tag{A.3}$$

$$S_0 = \frac{I}{I_{sat}} \tag{A.4}$$

where Γ_1 is the longitudinal relaxation rate, Γ_2 is the transverse relaxation rate, Γ is the spontaneous emission rate, I is the intensity of the driving field and I_{sat} is the saturation intensity. The intensity I is related to the electric field E by:

$$I = \frac{c\epsilon_0 E^2}{2} \tag{A.5}$$

where ϵ_0 is the permittivity of free space.
For $5P_{1/2} \rightarrow 6S_{1/2}$ and $5P_{3/2} \rightarrow 6S_{1/2}$ transitions in indium, the Rabi frequencies and the saturation parameters can be obtained from equation (A.2) and is shown in table 1.1.

Atomic Transition	Rabi Frequency	Saturation Intensity
$5P_{1/2} \rightarrow 6S_{1/2}$	$2\pi \cdot 0.19\text{MHz} \cdot S_0$	16.8mW/cm^2
$5P_{3/2} \rightarrow 6S_{1/2}$	$2\pi \cdot 0.28\text{MHz} \cdot S_0$	20.1mW/cm^2

Table 1.1. The Rabi frequencies of Indium for the relevant J→J' transitions are expressed in units of the saturation parameter, S_0, to account for the strength of the electric field.

Since in our experiment, the hyperfine transitions are significant, the saturation intensities of the relevant $F \rightarrow F'$ transitions of indium are calculated. Using the 6-j symbol, the dipole matrix elements for the $F \rightarrow F'$ transitions can be obtained from the reduced dipole matrix element of the $J \rightarrow J'$ transition [18]:

$$\langle F\|d\|F'\rangle = \sqrt{(2F+1)(2F'+1)}(-1)^{J+I+F'+1}\left\{\begin{array}{ccc} J & F & I \\ F' & J' & 1 \end{array}\right\}\langle J\|d\|J'\rangle \tag{A.6}$$

Manipulating equation (A.6) and summing over all possible hyperfine ground states F, we obtain the following equation:

$$\begin{aligned}\sum_F \frac{1}{2F'+1}|\langle F\|d\|F'\rangle|^2 &= \sum_F (2F+1)\left\{\begin{array}{ccc} J & F & I \\ F' & J' & 1 \end{array}\right\}^2 |\langle J\|d\|J'\rangle|^2 \qquad \text{(A.7)} \\ &= \frac{|\langle J\|d\|J'\rangle|^2}{2J'+1} \qquad \text{reference [53]} \qquad \text{(A.8)}\end{aligned}$$

From equations (A.2), (A.7) and (A.8), the spontaneous emission rate for the hyperfine transitions are related to the reduced matrix element for the $F \rightarrow F'$ transitions as follows:

$$\Gamma_{F'\rightarrow F} = \Gamma_{J\rightarrow J'}\frac{\omega^3_{F\rightarrow F'}}{\omega^3_{J\rightarrow J'}}(2J'+1)(2F+1)\left\{\begin{array}{ccc} J & F & I \\ F' & J' & 1 \end{array}\right\}^2 \tag{A.9}$$

From equations (A.1) and (A.2), the Rabi frequency $\Omega_{F\rightarrow F'}$ for the hyperfine transition is given by:

$$\Omega^2_{F\rightarrow F'} = \frac{1}{\hbar^2}\frac{|\langle J\|d\|J'\rangle|^2}{(2J'+1)}\frac{2F+1}{2F'+1}\frac{\Gamma_{F\rightarrow F'}}{\Gamma_{J\rightarrow J'}}E^2 \tag{A.10}$$

From equations (A.3) and (A.5), the saturation intensity I_{sat} for the hyperfine transition is given by:

$$I_{sat} = \frac{\Gamma^2}{2\,\Omega^2_{F\rightarrow F'}}\,I = \frac{\Gamma^2}{2\,\Omega^2_{F\rightarrow F'}}\frac{c\epsilon_0}{2}E^2 \tag{A.11}$$

where Γ=$2\pi\cdot25$MHz and $\Omega^2_{F\rightarrow F'}$ is given in equation(A.10). Note that the electric field factor E^2 will cancel out in equation(A.11).

The Rabi frequencies and the saturation intensities for each hyperfine transition is shown in Table 1.2.

$J \rightarrow J'$ Transition	$F \rightarrow F'$ Transition	Saturation Intensity (mW/cm^2)
$5P_{3/2} \rightarrow 6S_{1/2}$	$6 \rightarrow 5$	110.2
$5P_{3/2} \rightarrow 6S_{1/2}$	$5 \rightarrow 5$	183.7
$5P_{3/2} \rightarrow 6S_{1/2}$	$4 \rightarrow 5$	413.2
$5P_{1/2} \rightarrow 6S_{1/2}$	$5 \rightarrow 5$	334.1
$5P_{1/2} \rightarrow 6S_{1/2}$	$4 \rightarrow 5$	272.2

Table 1.2. Rabi frequencies and saturation intensities of indium for the relevant F→ F'transitions

Appendix B

Liouvillian for the Six-level Indium System

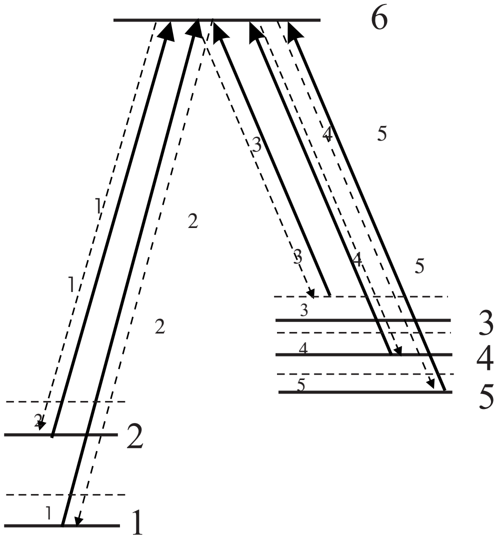

Figure B.1: *The coupled hyperfine levels for the Indium laser cooling scheme.*

The density matrix for a six-level atomic structure is defined as:

$$\rho = \begin{pmatrix} \rho_{11} & \rho_{12} & \rho_{13} & \rho_{14} & \rho_{15} & \rho_{16} \\ \rho_{21} & \rho_{22} & \rho_{23} & \rho_{24} & \rho_{25} & \rho_{26} \\ \rho_{31} & \rho_{32} & \rho_{33} & \rho_{34} & \rho_{35} & \rho_{36} \\ \rho_{41} & \rho_{42} & \rho_{43} & \rho_{44} & \rho_{45} & \rho_{46} \\ \rho_{51} & \rho_{52} & \rho_{53} & \rho_{54} & \rho_{55} & \rho_{56} \\ \rho_{61} & \rho_{62} & \rho_{63} & \rho_{64} & \rho_{65} & \rho_{66} \end{pmatrix} \tag{B.1}$$

The Liouvillian equation:

$$\frac{d\rho(t)}{dt} = \frac{1}{i\hbar}[\hat{H}, \rho(t)] + \hat{L}_{loss}\rho \tag{B.2}$$

This can be written as a set of differential equations:

$$\begin{aligned}
\frac{d}{dt}\rho_{11} &= -i\frac{\hbar}{2}(\Omega_1(\rho_{61} - \rho_{16})) + \Gamma_1\rho_{66} \\
\frac{d}{dt}\rho_{22} &= -i\frac{\hbar}{2}(\Omega_2(\rho_{62} - \rho_{26})) + \Gamma_2\rho_{66} \\
\frac{d}{dt}\rho_{33} &= -i\frac{\hbar}{2}(\Omega_3(\rho_{63} - \rho_{36})) + \Gamma_3\rho_{66} \\
\frac{d}{dt}\rho_{44} &= -i\frac{\hbar}{2}(\Omega_4(\rho_{64} - \rho_{46})) + \Gamma_4\rho_{66} \\
\frac{d}{dt}\rho_{55} &= -i\frac{\hbar}{2}(\Omega_5(\rho_{65} - \rho_{56})) + \Gamma_5\rho_{66} \\
\frac{d}{dt}\rho_{66} &= -i\frac{\hbar}{2}(\Omega_1(\rho_{16} - \rho_{61}) + \Omega_2(\rho_{26} - \rho_{62}) + \Omega_3(\rho_{36} - \rho_{63}) + (\rho_{46} - \Omega_4\rho_{64}) \\
&\quad +\Omega_5(\rho_{56} - \rho_{65})) - i\Gamma\rho_{66} \\
\frac{d}{dt}\rho_{12} &= -i\frac{\hbar}{2}(2(\Delta_1 - \Delta_2)\rho_{12} + \Omega_1\rho_{62} - \Omega_2\rho_{16}) \\
\frac{d}{dt}\rho_{13} &= -i\frac{\hbar}{2}(2(\Delta_1 - \Delta_3)\rho_{13} + \Omega_1\rho_{63} - \Omega_3\rho_{16}) \\
\frac{d}{dt}\rho_{14} &= -i\frac{\hbar}{2}(2(\Delta_1 - \Delta_4)\rho_{14} + \Omega_1\rho_{64} - \Omega_4\rho_{16}) \\
\frac{d}{dt}\rho_{15} &= -i\frac{\hbar}{2}(2(\Delta_1 - \Delta_5)\rho_{15} + \Omega_1\rho_{65} - \Omega_5\rho_{16}) \\
\frac{d}{dt}\rho_{16} &= -i\frac{\hbar}{2}(2\Delta_1\rho_{16} + \Omega_1(\rho_{11} - \rho_{66}) - \rho_{12}\Omega_2 - \rho_{13}\Omega_3 - \rho_{14}\Omega_4 - \rho_{15}\Omega_5) - 0.5\Gamma\rho_{16} \\
\frac{d}{dt}\rho_{21} &= -i\frac{\hbar}{2}(2(\Delta_2 - \Delta_1)\rho_{21} - \Omega_1\rho_{26} + \Omega_2\rho_{61}) \\
\frac{d}{dt}\rho_{23} &= -i\frac{\hbar}{2}(2(\Delta_2 - \Delta_3)\rho_{23} + \Omega_2\rho_{63} - \Omega_3\rho_{26}) \\
\frac{d}{dt}\rho_{24} &= -i\frac{\hbar}{2}(2(\Delta_2 - \Delta_4)\rho_{24} + \Omega_2\rho_{64} - \Omega_4\rho_{26}) \\
\frac{d}{dt}\rho_{25} &= -i\frac{\hbar}{2}(2(\Delta_2 - \Delta_5)\rho_{25} + \Omega_2\rho_{65} - \Omega_5\rho_{26}) \\
\frac{d}{dt}\rho_{26} &= -i\frac{\hbar}{2}(2\Delta_2\rho_{26} - \Omega_1\rho_{21} + \Omega_2(\rho_{66} - \rho_{22}) - \Omega_3\rho_{23} - \Omega_4\rho_{24} - \Omega_5\rho_{25}) - 0.5\Gamma\rho_{26} \\
\frac{d}{dt}\rho_{31} &= -i\frac{\hbar}{2}(2(\Delta_3 - \Delta_1)\rho_{31} - \Omega_1\rho_{36} + \Omega_3\rho_{61}) \\
\frac{d}{dt}\rho_{32} &= -i\frac{\hbar}{2}(2(\Delta_3 - \Delta_2)\rho_{32} - \Omega_2\rho_{36} + \Omega_3\rho_{62})
\end{aligned}$$

$$
\begin{aligned}
\frac{d}{dt}\rho_{34} &= -i\frac{\hbar}{2}(2(\Delta_3-\Delta_4)\rho_{34}+\Omega_3\rho_{64}-\Omega_4\rho_{36}) \\
\frac{d}{dt}\rho_{35} &= -i\frac{\hbar}{2}(2\Delta_3\rho_{35}-2\Delta_5\rho_{35}+\rho_{65}\Omega_3-\rho_{36}\Omega_5) \\
\frac{d}{dt}\rho_{36} &= -i\frac{\hbar}{2}(2\Delta_3\rho_{36}-\Omega_1\rho_{31}-\Omega_2\rho_{32}+\Omega_3(\rho_{66}-\Omega_3\rho_{33})-\Omega_4\rho_{34}-\rho_{35}\Omega_5)-0.5\Gamma\rho_{36} \\
\frac{d}{dt}\rho_{41} &= -i\frac{\hbar}{2}(2(\Delta_4-\Delta_1)\rho_{41}-\Omega_1\rho_{46}+\Omega_4\rho_{61}) \\
\frac{d}{dt}\rho_{42} &= -i\frac{\hbar}{2}(2(\Delta_4-\Delta_2)\rho_{42}-\Omega_2\rho_{46}+\Omega_4\rho_{62}) \\
\frac{d}{dt}\rho_{43} &= -i\frac{\hbar}{2}(2(\Delta_4-\Delta_3)\rho_{43}-\Omega_3\rho_{46}+\Omega_4\rho_{63}) \\
\frac{d}{dt}\rho_{45} &= -i\frac{\hbar}{2}(2(\Delta_4-\Delta_5)\rho_{45}+\Omega_4\rho_{65}-\Omega_5\rho_{46}) \\
\frac{d}{dt}\rho_{46} &= -i\frac{\hbar}{2}(2\Delta_4\rho_{46}-\Omega_1\rho_{41}-\Omega_2\rho_{42}-\Omega_3\rho_{43}+\Omega_4(\rho_{66}-\rho_{44})-\Omega_5\rho_{45})-0.5\Gamma\rho_{46} \\
\frac{d}{dt}\rho_{51} &= -i\frac{\hbar}{2}(2(\Delta_5-\Delta_1)\rho_{51}-\Omega_1\rho_{56}+\Omega_5\rho_{61}) \\
\frac{d}{dt}\rho_{52} &= -i\frac{\hbar}{2}(2(\Delta_5-\Delta_2)\rho_{52}-\Omega_2\rho_{56}+\Omega_5\rho_{62}) \\
\frac{d}{dt}\rho_{53} &= -i\frac{\hbar}{2}(2(\Delta_5-\Delta_3)\rho_{53}-\Omega_3\rho_{56}+\Omega_5\rho_{63}) \\
\frac{d}{dt}\rho_{54} &= -i\frac{\hbar}{2}(2(\Delta_5-\Delta_4)\rho_{54}-\Omega_4\rho_{56}+\Omega_5\rho_{64}) \\
\frac{d}{dt}\rho_{56} &= -i\frac{\hbar}{2}(2\Delta_5\rho_{56}-\Omega_1\rho_{51}-\Omega_2\rho_{52}-\Omega_3\rho_{53}-\Omega_4\rho_{54}-\Omega_5\rho_{55}+\rho_{66}\Omega_5)-0.5\Gamma\rho_{56} \\
\frac{d}{dt}\rho_{61} &= -i\frac{\hbar}{2}(-2\Delta_1\rho_{61}+\Omega_1(\rho_{11}-\rho_{66})+\Omega_2\rho_{21}+\Omega_3\rho_{31}+\Omega_4\rho_{41}+\Omega_5\rho_{51})-0.5\Gamma\rho_{16} \\
\frac{d}{dt}\rho_{62} &= -i\frac{\hbar}{2}(-2\Delta_2\rho_{62}+\Omega_1\rho_{12}+\Omega_2(\rho_{22}-\rho_{66})+\Omega_3\rho_{32}+\Omega_4\rho_{42}+\Omega_5\rho_{52})-0.5\Gamma\rho_{26} \\
\frac{d}{dt}\rho_{63} &= -i\frac{\hbar}{2}(-2\Delta_3\rho_{63}+\Omega_1\rho_{13}+\Omega_2\rho_{23}+\Omega_3(\rho_{33}-\rho_{66})+\Omega_4\rho_{43}+\Omega_5\rho_{53})-0.5\Gamma\rho_{36} \\
\frac{d}{dt}\rho_{64} &= -i\frac{\hbar}{2}(-2\Delta_4\rho_{64}+\Omega_1\rho_{14}+\Omega_2\rho_{24}+\Omega_3\rho_{34}+\Omega_4(\rho_{44}-\rho_{66})+\Omega_5\rho_{54})-0.5\Gamma\rho_{46} \\
\frac{d}{dt}\rho_{65} &= -i\frac{\hbar}{2}(-2\Delta_5\rho_{65}+\Omega_1\rho_{15}+\Omega_2\rho_{25}+\Omega_3\rho_{35}+\Omega_4\rho_{45}+\Omega_5(\rho_{55}-\rho_{66}))-0.5\Gamma\rho_{56}
\end{aligned}
$$

Appendix C

Relevant Indium Data

Atomic Mass	m	$115 \times 1.66\ 10^{-27}$ kg
Wavelength ($5P_{1/2} \leftrightarrow 6S_{1/2}$)	λ_1	410nm
Wavelength ($5P_{1/2} \leftrightarrow 6S_{1/2}$)	λ_2	451nm
Decay Rate ($6S_{1/2} \rightarrow 5P_{1/2}$)	Γ_{410}	$2\pi \cdot 8.9$MHz
Decay Rate ($6S_{1/2} \rightarrow 5P_{3/2}$)	Γ_{451}	$2\pi \cdot 16.2$MHz
Linewidth of $6S_{1/2}$ state	Γ	$2\pi \cdot 25.1$MHz
Recoil Velocity ($5P_{1/2} \rightarrow 6S_{1/2}$)	v_{rec1}	8.46 mm/s
Recoil Velocity ($5P_{3/2} \rightarrow 6S_{1/2}$)	v_{rec2}	7.69 mm/s
Recoil Frequency ($5P_{1/2} \rightarrow 6S_{1/2}$)	f_{rec1}	10.32 kHz
Recoil Frequency ($5P_{3/2} \rightarrow 6S_{1/2}$)	f_{rec2}	9.53 kHz
Doppler Temperature	T_{Dopp}	T_{Dopp}=600 μK
Doppler Velocity	v_{Dopp}	20.8 cm/s

Appendix D

Cooling Rate Calculation

The velocity change can be estimated in a one-dimensional transverse cooling experiment from the energy light shift $\hbar\omega_{LS}$. This calculation is valid only for a two-level atom. The maximum cooling rate $\frac{dE}{dt}$ in a standing wave configuration by the equation:

$$\frac{dE}{dt} = \frac{\hbar\,\omega_{LS}}{\tau_{fluo}} \tag{D.1}$$

where τ_{fluo} is the inverse of the scattering rate γ_p:

$$\tau_{fluo} = \frac{1}{\gamma_p} = \frac{1 + S_0 + (\frac{2\Delta}{\Gamma})^2}{S_0\Gamma/2} \tag{D.2}$$

and the light shift ω_{LS} is given by:

$$\omega_{LS} = \frac{\sqrt{\Omega^2 + \Delta^2} - \Delta}{2} \tag{D.3}$$

The rate of change of energy is related to the acceleration of the atom, a, the transverse velocity, v_t and the mass m, by the following equation:

$$\frac{dE}{dt} = \frac{dE}{dv}\frac{dv}{dt} = (\mathrm{m}\,\mathrm{v}_t)a \tag{D.4}$$

$$a = \frac{\hbar\,\omega_{LS}}{\mathrm{m}\,\mathrm{v}_t\,\tau_{fluo}} \tag{D.5}$$

If the acceleration is known, then the change in velocity can be obtained by the simple kinematic equation:

$$\begin{aligned} a &= \frac{\Delta \mathrm{v}}{\Delta t} = \Delta \mathrm{v}\,\frac{\mathrm{v}_{long}}{l} && \text{(D.6)} \\ \Delta \mathrm{v} &= \frac{\hbar\,\omega_{LS}}{\mathrm{m}\,\mathrm{v}_t\tau_{fluo}}\,\frac{l}{\mathrm{v}_{long}} && \text{(D.7)} \end{aligned}$$

where l is the interaction length and v_{long} is the longitudinal velocity of atoms in the atomic beam.

For the 410nm single-frequency cooling, S = 1, $\Delta = 1.1\Gamma_{410}$, the change in velocity is Δv= 1.12cm/s.

Appendix E

Energy Light Shift

The energy light shift of the ground state magnetic sublevel is given by [54]:

$$E_{LS} = \frac{\hbar \Delta S_0 C_{ge}^2}{1 + (2\Delta/\Gamma)^2} \tag{E.1}$$

where Δ is the detuning, Γ is the natural linewidth and C_{ge} is the Clebsch-Gordan coefficient that describes the coupling between the atom and the light field.
For S_0=1, $\Delta = 1.0\Gamma$, the energy light shift, in units of $\hbar\Gamma$, for the magnetic ground states of the indium atomic level scheme is tabulated below:

F=6 → F'=5 (451nm) transition driven by σ+ polarized light

$m_f = -6$	$m_f = -5$	$m_f = -4$	$m_f = -3$	$m_f = -2$	$m_f = -1$
0.2 Γ	0.167 Γ	0.136 Γ	0.110 Γ	0.085 Γ	0.064 Γ

$m_f = 0$	$m_f = +1$	$m_f = +2$	$m_f = +3$	$m_f = +4$	$m_f = +5$	$m_f = +6$
0.046 Γ	0.030 Γ	0.018 Γ	0.009 Γ	0.003 Γ	0	0

451nm F=6 → F'=5 transition driven by σ- polarized light

$m_f = -6$	$m_f = -5$	$m_f = -4$	$m_f = -3$	$m_f = -2$	$m_f = -1$
0	0	0.003 Γ	0.009 Γ	0.018 Γ	0.030 Γ

$m_f = 0$	$m_f = +1$	$m_f = +2$	$m_f = +3$	$m_f = +4$	$m_f = +5$	$m_f = +6$
0.046 Γ	0.064 Γ	0.085 Γ	0.110 Γ	0.136 Γ	0.167 Γ	0.2 Γ

451nm F=6 → F'=5 transition driven by linearly-polarized light

$m_f = -6$	$m_f = -5$	$m_f = -4$	$m_f = -3$	$m_f = -2$	$m_f = -1$
0	0.033 Γ	0.061 Γ	0.082 Γ	0.097 Γ	0.106 Γ

$m_f = 0$	$m_f = +1$	$m_f = +2$	$m_f = +3$	$m_f = +4$	$m_f = +5$	$m_f = +6$
0.109 Γ	0.106 Γ	0.097 Γ	0.082 Γ	0.061 Γ	0.033 Γ	0

Bibliography

[1] R. Feynman, *Feynman and Computation*, pp. 63-76, Perseus Books, Reading (1999)

[2] R. Hiremane, *From Moore's Law to Intel Innovation - Prediction to Reality*, Technology at Intel magazine pp. 1-9, (April 2005)

[3] D. Meschede and H. Metcalf, *Atomic Nanofabrication: Atomic Deposition and Lithography by Laser and Magnetic Forces*, J. Phys. D **36** R17 (2003)

[4] M. Mützel, S. Tandler, D. Haubrich, D. Meschede, K. Peithmann, M. Flasphler and K. Buse, *Atom Lithography with a holographic light mask*, Phys. Rev. Lett. **88**, 83601 (2002)

[5] G. Timp, R.E. Behringer, D.M. Tennant, J.E. Cunningham, M. Prentiss and K.K. Berggren, *Using light as a lens for submicron, neutral atom lithography*, Phys. Rev. Lett. **69**, 1636 (1992)

[6] F. Lison, H.J. Adams, D. Haubrich, M. Kreis, S. Nowak and D. Meschede,*Nanoscale atomic lithography with a cesium atom beam*, Appl. Phys. B: Lasers Opt. **65**, 419 (1997)

[7] J.J. McClelland, R.E. Scholten, E.C. Palm and R.J. Celotta, *Laser-focused atomic deposition*, Science **262**, 877 (1993)

[8] U. Drodofsky, J. Stuhler, Th. Schulze, M. Drewsen, B. Brezger, T. Pfau and J. Mlynek, *Hexagonal nanostructures generated by light masks for neutral atoms*, Appl. Phys. B **65**, 755 (1997)

[9] R.W. McGowan, D.M. Giltner and S.A. Lee, Opt. Lett. **20**, 2535 (1995)

[10] R. Ohmukai, S. Urabe, M. Watanabe, *Atom lithography with ytterbium beam*, Appl. Phys. B **77**, 415 (2003)

[11] B. Shore, *The Theory of Coherent Excitation* **vol. 2**, John Wiley and Sons Inc., New York (1990)

[12] http://physics.nist.gov/PhysRefData/Handbook/Tables/indiumtable3.htm

[13] E.U. Condon and G.H. Shortley, *The Theory of Atomic Spectra*, Cambridge Univ. Press, Cambridge (1953)

[14] G. Lindblad, Commun. Math. Phys. **33**, 305 (1973)

[15] J. Dalibard and C. Cohen-Tannoudji, *Dressed-atom approach to atomic motion in laser light: the dipole force revisited*, J. Opt. Soc. Am. B **2**, 1707-1720 (1985)

[16] T. Hänsch and A. Schawlow, *Cooling of gases by laser radiation*, Optics Communication **13**, 68-69 (1975)

[17] S. Chu, L. Hollberg, J. E. Bjorkholm, A. Cable and A. Ashkin, *Three-dimensional Viscous Confinement and Cooling of Atoms by Resonance Radiation Pressure*. Phys. Rev. Lett. **55**, 48-51 (1985)

[18] A.R. Edmonds, *Angular Momentum in Quantum Mechanics*, Princeton University Press, Princeton, **3rd edition** (1974)

[19] H. Metcalf and P. van der Straten, *Laser Cooling and Trapping*, Springer, New York (1999)

[20] H. Metcalf and P. van der Straten, *Laser Cooling and Trapping of Atoms*, J. Opt. Soc. Am. B **20**, 887-908 (2003)

[21] A. Aspect, J. Dalibard, A. Heidmann, C. Salomon and C. Cohen-Tannoudji, *Cooling Atoms with Stimulated Emission*, Phys. Rev. Lett. **57**, 1688 (1986)

[22] S. Nakamura, G. Fasol, *The Blue Laser Diode*, Springer, Berlin (1997)

[23] J.A. Armstrong, N. Bloembergen, J. Ducuing and P.S. Pershan, *Interaction between light waves in a nonlinear dielectric*, Phys. Rev. **127**, 1918-1939 (1962)

[24] D. Meschede, *Optics, Light and Lasers*, Wiley-Vch Verlag GmbH, Weinheim, Germany (2004)

[25] A. Yariv, *Optical Electronics*, Saunders College Publishing, Florida, U.S.A. **4th edition** (1991)

[26] J. Wang, *Opto-mechanical manipulation of indium atoms*, Ph.D. thesis, Bonn, Germany (2004)

[27] R. W. Boyd, *Nonlinear Optics*, Elsevier Science, Florida, U.S.A., **2nd Edition** (2003)

[28] T.W. Hänsch and B. Couillaud, *Laser Frequency Stabilization by Polarization Spectroscopy of a Reflecting Reference Cavity*, Optics Communications **35**, 441-444 (1980)

[29] A. Ashkin, G. Boyd and J. Dziedzic, *Resonant Optical Second Harmonic Generation and Mixing*, IEEE J. Quant. Electronics QE-2 **6**, 109-124 (1966)

[30] S. Metz, *Continuous Control of the Phase Difference in a Mach-Zender Interferometer and Second Harmonic Generation in a Periodically-Poled KTP Crystal*, M.S. thesis, New York, U.S.A (2004)

[31] H. Karlsson, *Email Communications - Specifications of the ppKTP crystal* Cobolt AB, Sweden, (2003)

[32] M. Houé and P.D. Townsend. *An introduction to methods of periodic poling for second-harmonic generation*, J. Phys. D Appl. Phys. **28**, 1747-1763 (1995)

[33] H. Metcalf and P. van der Straten, *Laser Cooling and Trapping*, Springer, New York (1999)

[34] D.W. Allan. *Statistics of atomic frequency standards*, Proc. IEEE **54**, 221-230 (1966)

[35] P.R. Berman, P.F. Liao and J.E. Bjorkholm. *Theory of saturation spectroscopy including collision effects*, Phys. Rev. A **20**, 2389-2404 (1979)

[36] C. Brechignac, R. Vetter and P.R. Berman. *Study of velocity-changing collisions in excited Kr using saturation spectroscopy*, Phys. Rev. A **17**, 1609-1613 (1978)

[37] U. Rasbach, J. Wang, R. dela Torre, V. Leung, B. Kloeter, D.Meschede, T. Varzhapertyan and D. Sarkisyan. *One- and Two-Color Spectroscopy on an Indium All-Sapphire Cell*, Phys. Rev. A **70**, 33810, September 2004

[38] W. Demtröder, *Laser Spectroscopy - Basic Concepts and Instrumentation*, Springer, Berlin, **3rd Edition** (2003)

[39] P. Lett, R. Watts, C. Westbrook, W. Phillips, P. Gould and H. Metcalf, *Observation of Atoms Laser Cooled Below the Doppler Limit*, Phys. Rev. Lett. **61** 169 (1988)

[40] C.A. Sackett, J. Chen, J.J. Tollett and R.G. Hulet. *Dipole Force Laser Cooling in Multilevel Atoms*, Laser Physics **4**, 861-865 (1994)

[41] J. Chen, J.G. Story and R. Hulet. *Evolution of atomic motion in an intense standing wave*, Phys. Rev. A **47**, 2128-2138 (1993)

[42] E. Kyrola and S. Stenholm. *Velocity Tuned Resonances as Multi-Doppleron Processes*, Opt. Commun. **22**, 123 (1977)

[43] S. Padua, C. Xie, R. Gupta, H. Batelaan, T. Bergeman, and H. Metcalf, *Transient Laser Cooling*, Phys. Rev. Lett. **70**, 3217 (1993)

[44] C. Salomon, J. Dalibard, A. Aspect, H. Metcalf, and C. Cohen-Tannoudji. *Channeling Atoms in a Laser Standing Wave*, Phys. Rev. Lett. **59**, 1659 (1987)

[45] A. Ashkin. *Trapping of Atoms by Resonance Radiation Pressure*, Phys. Rev. Lett. **40** 729 (1978)

[46] J. Dalibard and C. Cohen-Tannoudji. *Laser cooling below the Doppler limit by polarization gradients: simple theoretical models*, J. Opt. Soc Am. B **6**, 2023-2045 (1989)

[47] V. Finkelstein, P.R. Berman and J. Guo. *One-dimensional laser cooling below the Doppler Limit*, Phys. Rev. A **45**, 1829-1842 (1992)

[48] D. Boiron, C. Triche, D.R. Meacher, P. Verkerk and G. Grynberg. *Three-dimensional cooling of cesium atoms in four-beam gray molasses*, Phys. Rev. A **52** R3425-R3428 (1995)

[49] D. Boiron, A. Michaud, P. Lemone, Y. Castin, C. Salomon, S. Weyers, K. Szymaniec, L. Cognet and A. Clairon. *Laser cooling of cesium atoms in gray optical molasses down to* $1.1\mu K$ Phys. Rev. A **53** R3734-R3737 (1996)

[50] S. Chang and V. Minogin. *Density-matrix approach to dynamics of multilevel atoms in laser fields* Physics Reports **365**, 65-143 (2002)

[51] A. Aspect, E. Arimondo, R. Kaiser, N. Vansteenkiste and C. Cohen-Tannoudji. *Laser cooling below the one-photon recoil energy by velocity-selective coherent population trapping: theoretical analysis*, J. Opt. Soc. Am. B **6**, 2112-2124 (1989)

[52] M.D. Hoogerland, J.P. Driessen, e.D. Vredenbregt, H.J. Megens, M. P. Schuwer, H.C. Beijerinck, and K.A. van Leeuwen. *Bright Thermal Atomic Beams by Laser Cooling: A 1400-fold gain in beam flux* Appl. Phys. B **62**, 323-327 (1996)

[53] I.I. Sobelman, *Atomic Spectra and Radiative Transitions*, Springer, Berlin (1979)

[54] H. Metcalf and P. van der Straten, *Laser Cooling and Trapping* p. 101, Springer, New York (1999)

Acknowledgment

This thesis would not be completed without the insights, encouragement and support of my thesis adviser, Prof. Dieter Meschede. I would also like to extend my appreciation to Prof. Buse for accepting to be a co-referee of this thesis.

Working in the indium project has been adventurous and stimulating because of the presence of two post-docs, Dr. Ulrich Rasbach and Dr. Dietmar Haubrich. I thank both of them for editing this thesis and for the technical assistance, even beyond normal working hours. I also thank Prof. Metcalf for the stimulating discussions on our experimental results.

It has been a richly-rewarding and exhausting experience to work in such experiment. I thank Ulrich Rasbach and Jiayu Wang, who spent long hours in the laboratory with me and whose encouragement and enthusiasm helped us get through all the technical issues in the course of this work. Ulrich, with his extra-ordinary humor, and Jiayu, with his calmness, lightened the mood of the data-gathering stage. I am extending my appreciation to the new generation of the Indium team, Bernhard Kloter, Jae-Ihn Kim and Claudia Weber. For Jae-Ihn, who helped in enhancing the blue-light power, thank you for your contribution. For Bernhard, who edited parts of this thesis, and for Claudia, who worked with me during the later stage of the data-gathering, thank you. I also extend my acknowledgment to Susan Metz, who developed the ppKTP frequency-doubling cavity. I thank Dr. Stefan Kuhr for encouraging me when things are not working well with the project and for helping me in the German translation of the abstract. I thank Oscar Bulaong, Jr. for editing certain parts of this work within a short notice. I thank my officemates, Yann Louyer and Leonid Förster, for maintaining a good atmosphere in our office. I thank Dr. Wolfgang Alt for his insights on every physics question I have, and Yevhen Miroshnychenko for his help while I was printing this thesis.

Lastly, I thank my parents for everything they have invested in me.